A search for dark matter in dwarf spheroidal galaxies with VERITAS

Conor McGrath
17205746

This thesis is submitted to University College Dublin in fulfilment of the requirements for the degree of Doctor of Philosophy

School Of Physics
University College Dublin
Supervisor : Associate Professor John Quinn
Head of School : Professor Emma Sokell
September 2023

Contents

List of Figures

List of Tables

Abstract

Understanding the nature and identity of dark matter (DM) is a key goal in the physics community. As weakly interacting massive particles (WIMPs) interact only through gravity and the weak nuclear force they are popular candidates for the identity of DM. WIMPs are a particularly attractive candidate due to the so called "WIMP Miracle" which states that the predicted relic abundance of a WIMP DM is the same as the measured abundance of DM measured in the Universe today. Certain DM theories suggest that WIMPs may decay or annihilate into standard model particles with electromagnetic radiation up to very-high-energy (VHE) gamma-rays (greater than 100 GeV) produced in the process. The Very Energetic Radiation Imaging Telescope Array System (VERITAS) is an array of four imaging atmospheric Cherenkov telescopes (IACTs) that can indirectly detect VHE gamma rays in an energy range of 100 GeV to > 30 TeV, making it an ideal instrument to detect signatures of DM decay or annihilation. Dwarf spheroidal galaxies (dSphs) are chosen as the targets of this search for WIMP DM due to their high dark matter content and their low gamma-ray fluxes from other processes. The goal of this thesis is to use the full VERITAS dSph data set to derive the improved upper limits on the WIMP annihilation cross section to date. The newly implemented VERITAS image template method (ITM) is used to improve gamma-ray sensitivity during the analysis of each dSph. The DM mass range on which the upper limits are placed is extended beyond the unitary limit of a point-like DM particle by assuming above this mass limit DM particles are no longer point-like but instead have a geometrical cross section. This allows upper limits to be placed on the annihilation cross section of DM masses up to 10s of PeV as well as on the geometrical cross section of composite DM particles above ~ 100 TeV. This thesis also investigates the benefits of treating dSphs as largely extended sources in order to contain a larger fraction of their DM content. This required an investigation into maximum angular cut possible with the current VERITAS analysis pipeline. In order to complete these analyses a method of deriving the VERITAS point-spread function was required. This was initially performed in the absence of gamma-ray simulations using observations of the Crab Nebula and later with said gamma-ray simulations. The upper limits derived in

this thesis are the first results presented using the most state-of-the-art, physically motivated J-Factors. Despite these J-Factors predicting lower DM densities in most dSphs, the limits derived are the most constraining limits from an indirect search in dSphs with the largest DM mass range. The extended-source analysis in this thesis uses the largest angular cut to date on dSphs and shows the benefits of such an analysis.

Statement of original authorship

I hereby certify that the submitted work is my own work, was completed while registered as a candidate for the degree stated on the title page, and I have not obtained a degree elsewhere on the basis of the research presented in this submitted work. As a member of VERITAS[2], a collaboration of ~ 100 members I am not solely responsible for the data acquisition, calibrations, planning or upkeep of the VERITAS instrument. All members of the collaboration are expected to contribute time annually to the many tasks required to keep the experiment operational. This includes but is not limited to : on site observation shifts, data quality monitoring, calibration tasks and software maintenance. While I was not a VERITAS member when any of the data used in this thesis was taken I have performed multiple observing shifts both on site and remotely. The same goes for the analysis software used, many of these tools were developed over the course of many years in the early days of VERITAS, and while I was not involved in development I have contributed support and maintenance help during my time as a VERITAS member. All VERITAS source analyses presented in this thesis (dSphs, Crab and OJ287) were performed by me. As well as this any PSF and EA generation and studies were also performed by me. Finally the dark matter analysis pipeline used in this thesis was developed by me and the upper limit search using said pipeline was performed by me. Any open source material or software used within this thesis or my analysis is highlighted when discussed.

---

[2] https://veritas.sao.arizona.edu/

I was born not knowing and have had only a little time to change that here and there.

Richard P. Feynman

Acknowledgements

This thesis would never have been possible without the unrelenting support of my family, friends and loved ones. In particular my parents Siobhan and Kevin for encouraging me at every step along my academic career and for supporting me along every path I've taken this far in life, be it my dreams of being a rockstar, brewmaster or astrophysicist. My sister Ciara for her endless advice about how to survive academia, genuine interest in my research (maybe now you'll finally understand what I do) and for supplying me with a place to sleep whenever I want to visit her. My incredible partner Sarah who offered endless encouragement, advice, jokes, command line support, smiles and days of her time to help me through the PhD process, all while completing her PhD is second to none, Yeehaw!. Finally to anyone who ever showed interest, support, encouragement or a minute of their time during the last four years, thank you.

A chapter of this thesis alone could be dedicated to my supervisor John Quinn. John has been a great help to me since before my PhD began, from supervising my MSc research to helping me with PhD funding applications to his overwhelming support during my PhD, this thesis would definitely not exist without him. On an academic level I have learned invaluable lessons about the scientific approach, programming and computing, and even the proper use of a hyphen. John was always available to answer any question I might have no matter how big or small and would always ask the questions that I didn't realise I should be asking. On a personal level our many chats and complaining sessions about sport, life and tech made for an ideal work environment.

To everyone who made my time in UCD more enjoyable thank you all. Baibre Fox for the many chats about sports and Chelsea F.C., Roderick Jones for the coffee breaks and laughs and Paul Hanratty for putting up with me throughout my time in labs. To everyone involved in the MSc. in Space Science and Technology, thank you for putting me on the path to where I am today. In particular to the class of 17/18 and Robert Jeffrey for your dedication as a teacher and the great discussions when demonstrating together.

Being a member of VERITAS afforded me the opportunity to travel around the world, but more importantly it introduced me to many great scientists and a fantastic group of people. I could thank nearly every member for one reason or another. In particular I'd like to thank Amy, Atreya, Colin, Claire, Deivid, Elisa, Jack, Jamie × 2, Matt, Olivier, Sam and Ste for good laughs, great chats and even better advice.

Finally a thank you to the miscellaneous that have been a excellent source of distraction, entertainment and support over the last four years : Chelsea Football Club, Pittsburgh Steelers, DONUT, South Dublin Panthers, Underdog Dublin, The Gaslight Anthem, NVRMNT, Boojum, Sunday pints, Reinkarnated Dublin and Corrstown Golf Club.

1 Introduction

The field of TeV astronomy has a short but impactful history. The first TeV gamma-rays were detected by the Whipple collaboration in 1989 using the Whipple 10-meter gamma-ray telescope (Weekes et al. 1989). These gamma rays were seen coming from the Crab Nebula which is one of the brightest steady sources in the gamma-ray sky and is still well studied to this day (Bühler and Blandford 2014). In the early days there remained very few known TeV gamma-ray sources but as observations continued more sources were discovered. Some notable early discoveries include the active galaxy Markarian 421 (Mrk 421) (Punch et al. 1992) and the detection of TeV gamma rays from the blazar Markarian 501 (Mrk 501) (Quinn et al. 1996), both of which were discovered at the Whipple Observatory. In the years since, more modern TeV observatories have been able to detect many more sources of TeV gamma rays. These sources are some of the most energetic galactic and extragalactic objects such as active galactic nuclei (AGN) (Netzer 2015), gamma-ray bursts (GRBs) (Fishman and Meegan 1995) and stellar explosions. Some of the main science goals of TeV astrophysicists include investigating the mechanisims and enviornments that are allow partices to be accelerated to such high energies, the search for the origins of cosmic rays, understanding transient events such as GRBs and understanding the central engines and jet physics of AGN. In recent years gamma-ray experiments have worked along side experiments such as gravitational wave (Adams et al. 2021) and neutrinos detectors (Acharyya et al. 2023) in an aim to find gamma-ray counterparts to such events. Finally TeV gamma rays can be used to investigate fundamental physics topics such as the potential for Lorentz invariance violations are high energies, the existence of exotic particles such as Axions or Axion like particles and the identity of dark matter (DM).

Understanding the nature and identity of DM has been an outstanding scientific problem since its discovery by Zwicky in 1933. DM is currently believed to make up roughly 85% of mass in our universe and as a result the majority of matter in our universe is of unknown origin. Despite this the only observational evidence for the existence of this matter comes from gravitational interactions. Without the existence of DM current physics theory could not explain the mass and dynamics of galaxies or the evolution of the universe to its current state. As DM is believed to be of non-standard model origin the discovery of it would lead to major changes in the field of particle physics by potentially introducing a whole new category of particles or changing current understanding of fundamental physics. There is also the possibility that there is in fact no DM but instead current gravitational theory is not complete at astronomical levels. The disproof of the existence of DM would therefore have a major impact on a heavily relied upon area of physics.

One of the leading candidate DM particles is the Weakly Interacting Massive Particle (WIMP). WIMPs arise from many Standard Model (SM) extensions, for example and most notably in Supersymmetry. WIMPs are postulated to have an interaction cross-section no larger than the cross-section for the weak interaction and mass in the range of 10 GeV to 10s of TeV and to have formed during the early universe with their current abundance as a result of a "freeze-out". WIMPs are a popular theory due to their predicted relic abundance matching the measured DM abundance in the universe today in what is known as the "WIMP miracle". The WIMP model is also attractive to physicists as it predicts a particle-DM instead of other more exotic solutions.

DM searches fall under three different categories: direct, indirect and production. Direct-detection experiments attempt to observe collisions between SM and DM particles, whereas indirect detection may be made via the observations of gamma rays produced in the decay or annihilation of WIMPs to SM particles. Finally, the collider experiments use collisions between standard model particles in an attempt to produce DM. The most favourable targets used in indirect WIMP DM searches will have a large DM content and minimal gamma rays produced from other astrophysical processes. For this reason dwarf spheroidal galaxies (dSphs) are popular targets of observations. DSphs are predicted to have a large DM content, a high mass to luminosity ratio and a negligible astrophysical background. To date there have been several indirect searches for gamma-ray products of WIMP annihilation and/or decay carried out by the current state-of-the-art gamma-ray observatories Fermi-LAT, H.E.S.S., MAGIC, HAWC and VERITAS, leading to constraints on the thermally-averaged cross section and the decay lifetime.

2 The Imaging Atmospheric Cherenkov Technique

Unlike space-based gamma-ray telescopes or ground-based optical and radio telescopes which directly detect photons, ground-based gamma-ray telescopes indirectly detect gamma rays via showers of relativistic charged particles produced through interactions between the gamma ray and the Earth's atmosphere. The air shower will produce a light pool of Cherenkov radiation with a ground radius of $\sim$ 130 m. The maximum emission of Cherenkov radiation occurs at the point with the largest number of cascaded particles which for energies between 100 GeV and 1 TeV is $\sim$ 10 km. Imaging atmospheric Cherenkov telescopes (IACTs) must have a large light collection area, a means to differentiate gamma-ray induced Cherenkov showers from cosmic ray background light and the ability to reconstruct the energy and incident direction of a photon. In order to do this, IACTs are designed with large mirrors ($\sim$ 100 m^2) to allow for a large light collection area, cameras built from PMTs in order to capture the nanosecond flashes and are often built in pairs or arrays to incorporate array-level stereoscopic shower reconstruction techniques. The image seen as a result of a gamma ray by an IACT will be a narrow ellipse, which differs from those produced by background cosmic rays. The major axis of the image ellipse describes the vertical extension of the shower as well as points in the direction of the source position, this means that with the use of multiple telescopes observing the same shower the source location can be inferred from the intersection of these directions. The shower height can then be estimated from the distance of the shower location (on the ground plane) to each telescope, this parameter is known as the impact parameter. See Figure 1 for a visual representation of an IACT array observing a Cherenkov shower. The first detection of a gamma-ray source using the IACT technique was achieved when the Crab Nebula was successfully detected above the background by the Whipple collaboration using the 10 m telescope at Fred Lawrence Whipple Observatory (Cawley et al. 1985), which is the current day location of the VERITAS telescope array. Since then the field of IACTs has grown greatly with the IACT technique still used in modern active experiments such as VERITAS (Holder et al. 2008), MAGIC (Albert et al. 2008) and H.E.S.S (Hinton and HESS Collaboration 2004). An alternative to the IACT method is the water

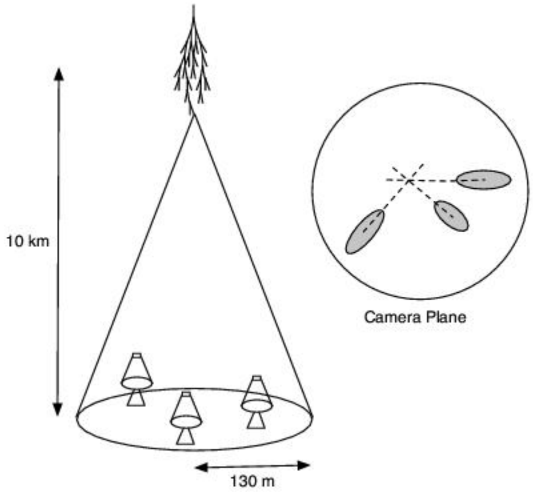

Figure 1: A Cherenkov light pool originating roughly 10 km above Earth falling on an array of 3 IACTs. Upper right shows examples of the images that will be seen by each telescope and how the core location of the shower is reconstructed. Credit : VERITAS Collaboration

Cherenkov method. This method uses tanks of water instead of the atmosphere to induce Cherenkov radiation. Each tank of water will also contain an array of detectors which image the induced Cherenkov radiation. The most notable active experiment which employs this method is HAWC (Fuente et al. 2013).

2.1 Extensive Air Showers

An extensive air shower (EAS) is a shower of secondary particles produced when a particle such as a gamma ray, lepton or hadron enters the Earth's atmosphere. When a gamma ray enters and interacts with the atmosphere it will undergo a pair production process : producing an electron-positron pair. The electron-positron pair produced will have equal energies and if the energy of gamma ray is much greater than the rest-mass energy of the electron-positron pair they will travel in the same direction as the gamma ray. Following this, the electron and positron will begin to produce secondary photons via bremsstrahlung where upon deflecting off of atomic nuclei the particle will emit the energy lost through the deflection in the form of a photon. The electron or positron will continue to undergo this process producing more gamma rays, while at the same time the produced gamma rays will undergo pair production thus producing more electron-positron pairs. This cycle of processes will continue until the energy of the photons are lower than that is required for pair production to occur and thus halting the production of electron-positron pairs and further secondary photons. The minimum energy required for a gamma ray to undergo pair production is $2m_ec^2$ or 1.022 MeV and the minimum energy required for bremsstrahlung is ∼84 MeV. As the energy of the secondary particles will decrease with each process it means that the maximum number of particles seen in a shower is dependent on the energy of the initial incident particle. A projection of a gamma-ray induced Cherenkov shower and a cosmic-ray induced Cherenkov shower can be seen in Figure 2. The average distance travelled by a particle before it undergoes bremsstrahlung is known as the radiation length or X_0, this distance describes the distance travelled after which a photon will lose $\frac{1}{e}$ of its original energy through radiation. In our atmosphere X_0 for bremsstrahlung is $X_0 = 36.62$ g cm^{-2} which is 7/9 of the mean free path for pair production. This results in both pair production and bremsstrahlung occurring after similar particle distances travelled. Since at the average height of the atmosphere it's density is ∼1033 g cm^{-2} and since the initial pair production process must occur very close to the top of the atmosphere, a particle shower will undergo roughly 28 radiation lengths and therefore any showers seen at ground level must have been produced by a highly energetic particle. As mentioned in Section 2.3 any charged particle in the EAS which is above the required threshold will produce Cherenkov radiation during this process.

2.2 Hadronic Showers

An EAS can also be induced when leptons or hadrons enter the atmosphere. For example most hadrons upon interacting with the Earth's atmosphere, will produce pions (π^0, π^+ and π^-). The π^0 will quickly decay into two gamma rays which will then undergo pair production followed by bremsstrahlung and thus producing an EAS which is nearly indistinguishable from a shower produced by a single gamma ray. This becomes a source of background for an IACT. Charged pions (π^+ and

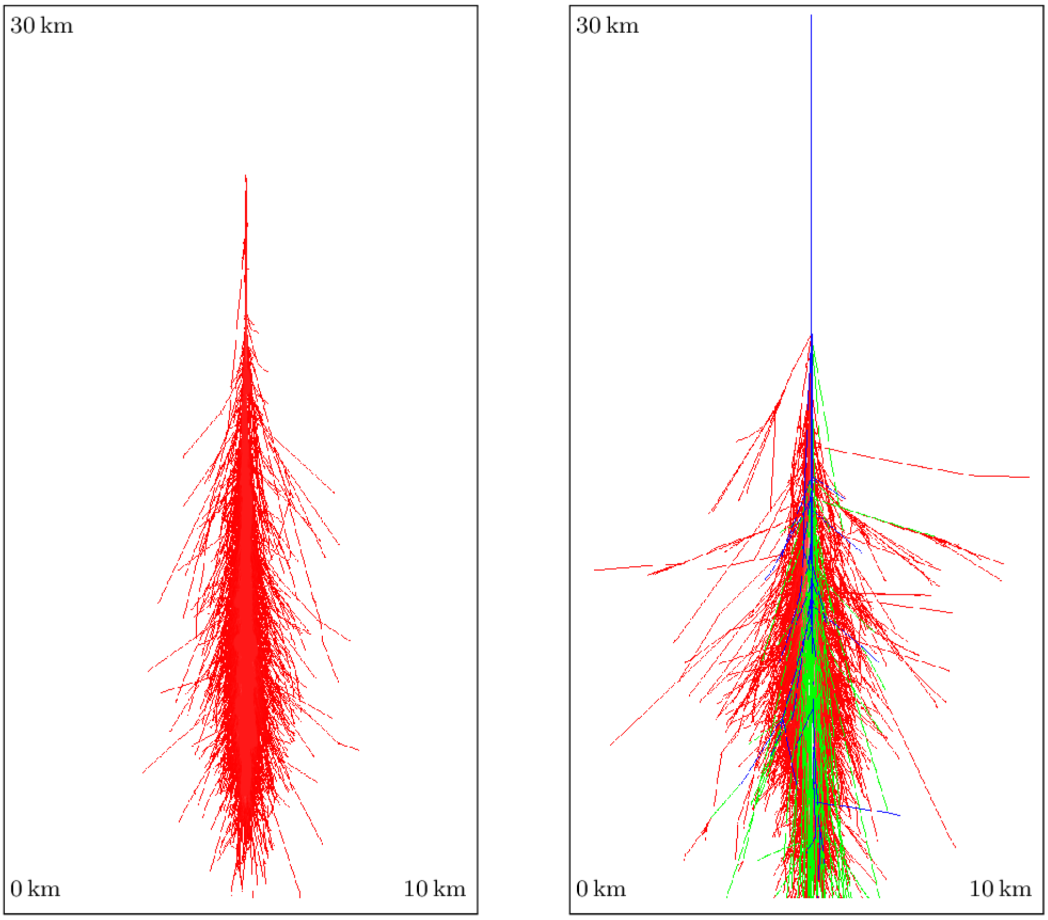

(a) γ-ray induced air shower with 300 GeV and first interaction in 23 km height

(b) hadron induced air shower with 1 TeV and first interaction in 18 km height

Figure 2: A comparison between the EAS produced by a gamma ray and one produced by a hadron, where the hadronic component is shown is blue, muon component in green and electromagnetic component in red (Häffner 2014).

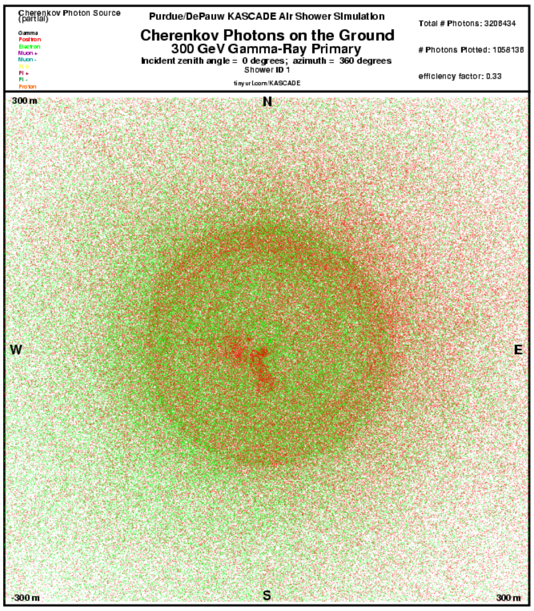

Figure 3: Simulation of a Cherenkov shower at ground level produced by a 300 GeV gamma ray. Purdue/DePauw Universities

π^-) on the other hand will produce muons who are also a source of Cherenkov radiation. It is also possible for cosmic electrons and positrons to interact with the atmosphere and induce an EAS, these showers will once again appear similar to those initially produced by a gamma ray and as a result will add to the background. A common difference between showers produced by gamma rays and those produced by hadrons is the distribution and development of the showers. Due to their significant transversal momentum the showers produced by hadrons can be often spread over a larger area and clumpy, Figures 3 and 4 show examples of both a gamma ray and hadronic shower projected onto the ground plane.

2.3 Cherenkov Radiation

It is not uncommon for charged particles such as electrons and positrons to move faster than the speed of light in media such as water where the speed of light is slowed down by roughly 25%. In the realm of very high-energy astronomy, Cherenkov

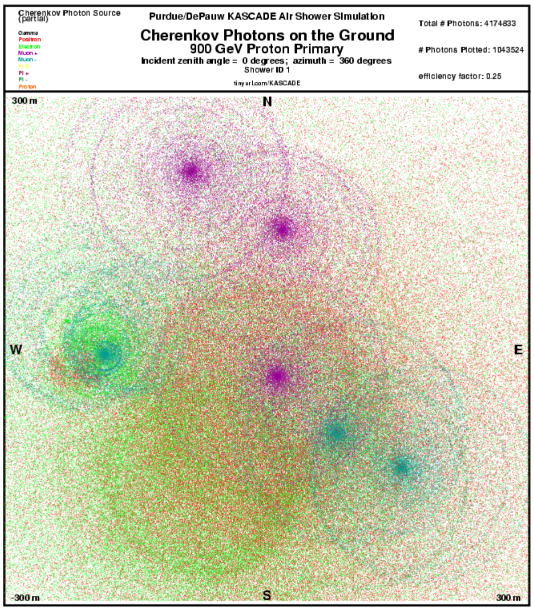

Figure 4: Simulation of a Cherenkov shower at ground level produced by a 900 GeV proton. Purdue/DePauw Universities

radiation is emitted when a high-energy gamma ray or cosmic ray interacts with our atmosphere and produces secondary charged particles which travel faster than light in the medium. A charged particle travelling in a dielectric medium will induce polarisation in the medium. This is because as the charged particle passes particles within the medium, the particles in the medium are briefly excited. These particles then return to their ground-state via the emission of photons. In cases where the charged particle has a velocity $v < \frac{c}{n}$ where c is the speed of light and n the refractive index of the medium, the polarisation around the charged particle will be close to symmetric. The emitted waves will not undergo any interference and will not be visible due to their low intensity. On the other hand, if the charged particle has a velocity greater than the speed of light in the medium, i.e. $v > \frac{c}{n}$ the polarisation will be no longer symmetric as the medium's particles do not have time to return to their base states resulting in the emitted waves overlapping. The overlapping waves will undergo constructive interference leading to visible cones of light known as Cherenkov radiation (Jelley 1955). This process is not dissimilar to the processes that cause sonic booms when sound waves produced by a body travelling faster than the speed of sound cannot propagate forward and instead produce a shock wave known as a sonic boom. The cone of Cherenkov light is produced with an angle from the initial particle of

$$\cos\theta = \frac{1}{\beta n} \tag{1}$$

where $\beta = \frac{v}{c}$ and n is once again the refractive index of the medium. For a 1 TeV primary gamma ray this pool of Cherenkov light has a photon density of ~ 100 photons m^{-1} (Holder 2015). By looking at the factor of n alone we can see that the Cherenkov angle will decrease with increasing height as the refractive index of air decreases with altitude. A sketch of how a Cherenkov wave front is produced, with the Cherenkov angle highlighted is shown in Figure 5.

This means that a Cherenkov emission at an altitude of roughly 10 km will have a ground radius of roughly 120 m. This fact was used by VERITAS collaboration when choosing the locations for each telescope. Each telescope is positioned roughly 100 m from one another to ensure showers will be seen by multiple telescopes to allow

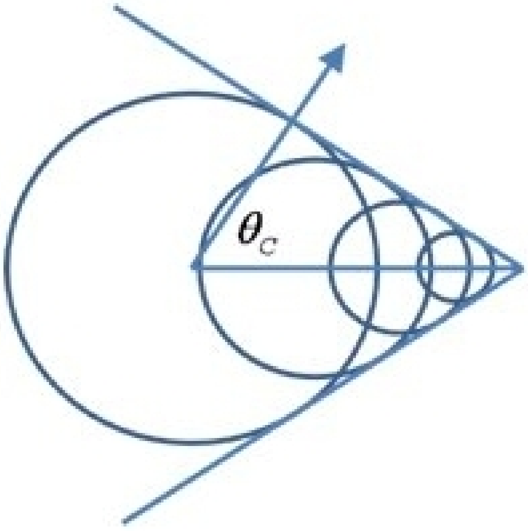

Figure 5: A visualisation of the Cherenkov angle. The horizontal blue line is the trajectory (left to right) of the charged particle traveling at speed v. The blue circles are individual wavelets formed by the passing of the particle. As the wavelets undergo constructive interference the wave front (diagonal lines) is emiited at an angle θ from the charged particle's trajectory. Credit : PhysicsOpenLab

for stereoscopic views of each shower. This spacing between telescopes also helps to reject local background muons as their Cherenkov light cones are only seen by a single telescope. The spectrum of Cherenkov light which peaks at short wavelengths (UV-blue) is described by the Frank-Tamm equation (Frank and Tamm 1937) :

$$\frac{\delta^2 N}{\delta x \delta \lambda} = 2\pi\alpha \frac{1}{\lambda^2}\left(1 - \frac{1}{\beta^2 n^2(\lambda)}\right) \tag{2}$$

where $\alpha \approx 1/137$ is the fine-structure constant and x is the unit distance travelled by the particle.

2.4 Current Ground-Based Gamma-ray Observatories

Current ground-based gamma-ray observatories fall into two categories, Imaging Atmospheric Cherenkov Telescopes (IACTs) and water Cherenkov detectors (WCD). Current IACTs include the Very Energetic Radiation Imaging Telescope Array System (VERITAS) (Holder et al. 2008), the High Energy Stereoscopic System (H.E.S.S.) (Hinton and HESS Collaboration 2004), the Major Atmospheric Gamma Imaging Cherenkov Telescope (MAGIC) (Albert et al. 2008) and the future Cherenkov Telescope Array (CTA) (Acharya et al. 2013). The currently active water Cherenkov detector are the High Altitude Water Cherenkov Experiment (HAWC) (Fuente et al. 2013) and the water Cherenkov detector array (WCDA) at the Large High Altitude Air Shower Observatory (LHAASO) (Ma et al. 2022). IACTs are telescopes with rapid cameras and large collection areas designed to observe nanosecond pulses of Cherenkov radiation that are induced by gamma rays when they interact with the Earth's atmosphere. Water Cherenkov detectors instead use water pools to detect charged relativistic particles as they pass through the water. One of the key differences between IACTs and water Cherenkov detectors is their fields-of-view, IACTs are pointing telescopes with fields of view on the order of 3° to 5° which gives them a greater sensitivity and angular resolution than water Cherenkov detectors. On the other hand water Cherenkov detectors have fields-of-view of ~ 1.5 str which means although they have a lower sensitivity they can operate as survey instruments that can observe a large number of targets at once. As water Cherenkov detectors use water pools to detect Cherenkov radiation they are capable of operating during daytime leading them to have duty cycles of close to 100%. This also makes them great survey instruments and leads to a higher likelihood of detecting transient events such as gamma-ray bursts or gravitational wave events.

2.4.1 Imaging Atmospheric-Cherenkov Telescopes

VERITAS is an array of four 12 m IACTs located in southern Arizona, USA that began full array operations in 2007. VERITAS has an energy range of 85 GeV to $>$ 30 TeV and is the instrument used in this thesis.

H.E.S.S. is an array of four 12 m IACTs and a fifth 28 m telescope located in Khomas Region, Namibia that began operations in 2004 with the 28 m telescope being added in 2012. H.E.S.S. has an energy range of 30 GeV to $>$ 10 TeV, the lower energy range is achieved by the addition of the larger 28 m telescope.

MAGIC is a pair of two 17 m telescopes located on the island of La Palma, Spain that began operations in 2004. Due to its large mirrors and high altitude (2200 m) MAGIC is more sensitive to lower-energy gamma rays and has an energy range of 50 GeV to $>$ 10 TeV.

CTA is an array of more than 60 IACTs that is currently under construction. CTA will have telescopes located at two sites, the island of La Palma, Spain in the northern hemisphere and Paranal, Chile in the southern hemisphere. CTA will be sensitive to gamma rays in an energy range of 20 GeV to $>$ 300 TeV, this energy range is achieved by the use of three different sizes of telescope.

2.4.2 Water Cherenkov Detectors

HAWC is an array of 300 water Cherenkov detectors located on the flanks of the Sierra Negra volcano in Puebla, Mexico. It is the successor to the Milagro gamma-ray observatory (Yodh 1997) and began operations in 2015. HAWC has an energy range of 100 GeV - 100 TeV and a field-of-view covering 15% of the sky which allows it to observe 2/3 of the sky in a 24 hour period.

The WCDA at LHAASO is an array of 3,120 water Cherenkov detectors located in Daocheng, Sichuan province, P.R. China which began operations in 2019. The

WCDA alone has an energy range of 100 GeV - 30 TeV but when combined with the other instruments used in the experiment (the 1.3 km^2 array (KM2A) of electromagnetic particle and muon detectors, the 18 wide field-of-view air Cherenkov telescopes (WFCTA) and a newly proposed electron-neutron detector array (ENDA)) the observatory has an energy range of 200 GeV - 1 PeV.

2.4.3 Summary

Some of the key differences between IACTs and water Cherenkov detectors are their angular resolution, the energy range in which they're most sensitive and the times at which they can observe. These differences will present themselves differently depending on the type of study performed with each instrument but there are some generalities. As IACT experiments often utilise arrays of telescopes, it is possible to produce stereoscopic views of each gamma-ray shower. The use of stereoscopic views means triangulation can be used to more accurately determine the direction from which the gamma ray came. This leads to a better angular resolution and the ability to more precisely localise gamma-ray sources. While water Cherenkov detectors have a lesser angular resolution due to instrument characteristics this comes with the benefit of a large effective area and energy threshold, both of which are at least in part due to their large scale. As the energy of an incident gamma ray increases as will the size of the shower produced, this means that at a certain size an instrument's camera will become saturated and any images larger than this will all appear the same size. This determines the upper bound of the energy threshold of the instrument. As the collection area and FoV of water Cherenkov detectors is greater than that of IACTs, water Cherenkov detectors can successfully reconstruct gamma rays from larger shower images and as a result have a greater energy threshold. One of the key limitations to the lower energy threshold of ground-based gamma-ray telescopes is the gamma ray being energtic enough to penetrate deep enough into the atmosphere. In order to observe gamma rays below these energies telescopes must be placed above the atmosphere and be directly observed. For example, the Fermi Gamma-ray Space Telescope (Moiseev et al. 2007) is a space based telescope with an energy range of 20 MeV to more than 300 GeV - a ideal range to complement that of IACTs and water Cherenkov detectors. Much like water Cherenkov detectors space based detectors like the Fermi Gamma-ray Space Telescope observations are not affected by day or moonlight and as a result have a duty cycle of nearly 100%.

3 VERITAS

The Very Energetic Radiation Imaging Telescope Array System (VERITAS) is an array of four 12-meter diameter IACTs located at the Fred Lawrence Whipple Observatory (FLWO) in southern Arizona which has an altitude of 1268 m. VERITAS has been in full array operation since 2007 and is currently funded to operate through the year 2025. Located at the reflector focal point, the camera in each telescope is made up of 499 photo-multiplier tubes (PMTs) onto which the hexagonal mirrors focus the images. PMTs are used in the camera due to their fast response. Each pixel has a field of view (FOV) of $\sim 0.1°$ which gives the array a total FOV of 3.5°. VERITAS can indirectly detect gamma rays in the energy range of 100 GeV to >30 TeV, it has an energy resolution of 17% for a 1 TeV photon and can achieve a 5 σ detection of a source with 1% the flux of the Crab Nebula in $\sim$ 25 hours of observations. There have been 6 VERITAS configurations (V1 - V6), the work in this thesis focuses on V4 (the beginning of four telescope operations in 2007) onward. A major hardware improvement occurred in the summer of 2009 in which telescope 1 was moved from its initial location to its current, a visualisation of the past and current positions of the telescopes can be seen in Figure 6. This move resulted in a more symmetrical array and a 30% improvement in sensitivity (Perkins, Maier, and VERITAS Collaboration 2010). Following this, in the summer of 2012 all four telescopes underwent a camera upgrade. This camera upgrade consisted of replacing all 499 PMTs in each camera with new high-quantum-efficiency PMTs resulting in a 50% increase in photon-detection efficiency and a 30% reduction in triggering threshold (Kieda 2013). As mentioned, these major upgrades break up the timeline of VERITAS's operations from V4 onward into 3 epochs, namely: V4 (01/September/2007 - 31/August/2009) - which ran from the beginning of four-telescope operations until the relocation of telescope 1, V5 (01/September/2009 - 31/August/2012) - which ran from the relocation of telescope 1 until the four-telescope camera upgrade and V6 (01/September/2012 - present) - which has been running from the camera upgrades until today.

Figure 6: The locations and distances between telescopes both before the relocation of T1 (Blue) and after (Red)

3.1 Optical Support Structure and Mirrors

Each VERITAS telescope consists of an altitude-over-azimuth positioner and a tubular steel optical support structure (OSS). The OSS is a space frame of $\sim$ 12m in diameter and the camera is mounted on a counter-weighted quadropod. The VERITAS telescopes are capable of slewing at speeds up to 1° per second but is limited to $\sim 0.3° - 0.5°$ per second during operations. A picture of a VERITAS telescope where the OSS, mirrors and positioner are shown in Figure 7. Each of the four VERITAS telescopes contain a Davies-Cotton optical support structure (Davies and Cotton 1957) with a 12 m aperture reflector. Each reflector contains 350 hexagonal mirrors giving the telescope a total collection area of $\sim$100 m^2. Hexagonal mirrors are used in order to minimise the deadspace between mirrors. Multiple mirrors are chosen over a single dish in order to avoid having to account for the weight and cost of a single mirror when designing the OSS, it also allows for the removal of individual mirrors for cleaning, recoating or replacement. Each mirror is made of polished glass which is aluminised and anodised. As the mirrors are not covered they undergo gradual degradation due to exposure to dust and sand in the local environment. For this reason the mirror reflectivity is regularly measured and mirrors are often cleaned and sometimes recoated, a plot showing the reflectivity of newly coated and cleaned mirrors can be seen in Figure 8. Each mirror of a VERITAS telescope is manually

Figure 7: An image of a VERITAS telescope showing the mirror structure.

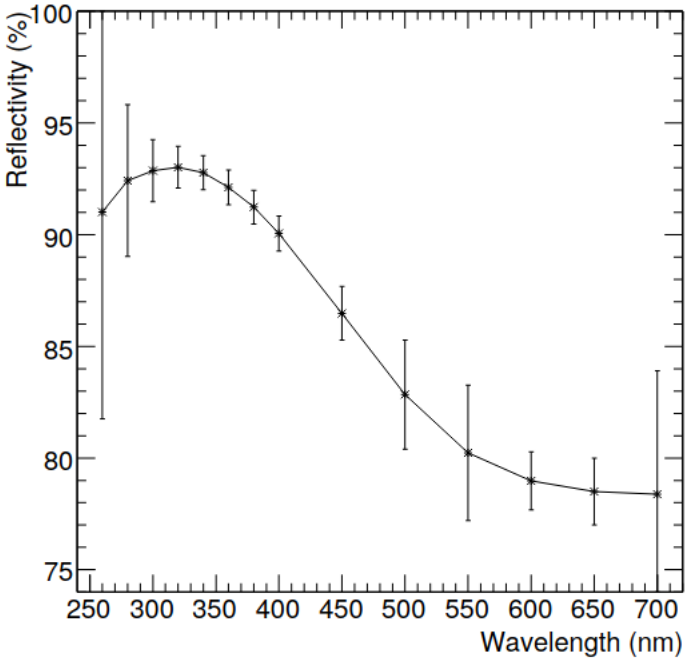

Figure 8: The VERITAS mirror reflectivity shown as a function of wavelength from (Roache et al. 2008)

aligned in order to allow the separate mirrors to act as a single dish. The mirrors are aligned using the "raster" scan method (McCann et al. 2010).

3.2 The VERITAS Cameras

Each VERITAS camera is made up of 499 PMTs housed in a 1.8 m square box. The PMTs used in the first VERITAS cameras were Photonis 2.86 cm diameter, UV sensitive PMTs (model XP2970/02), which were replaced in 2012 by Hamamatsu R10560-100-20 MOD PMTs. The new high-quantum efficiency (hQE) PMTs increased the QE from ∼20% to ∼35%. In order to maximise the light collection efficiency of the camera the PMTs are arranged in a hexagonal pattern, the remaining gaps between pixels are accounted for by the addition of 499 Winston light concentrator light cones (Winston 1970) which are attached to the front of the VERITAS cameras. Figure 9 shows the arrangement of the pixels and lightcones in a VERITAS

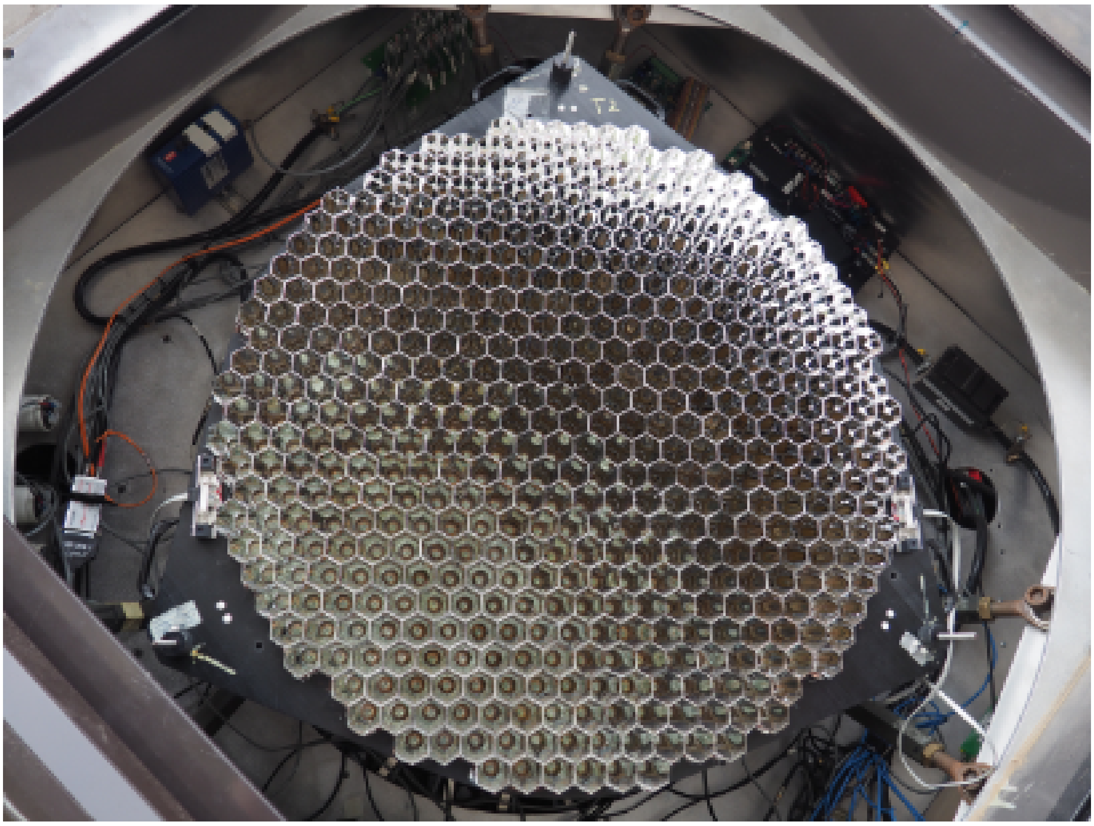

Figure 9: An image of the VERITAS camera showing the hexagonal light cones atop the PMTs which make up the 499 pixels. - VERITAS Collaboration

camera. The typical high voltage (HV) of each PMT is 900 kV.

3.3 The Trigger System

In order to reduce the rate of background events triggered by fluctuations in the night sky background (NSB) or cosmic rays VERITAS employs a 3 level triggering system (Weinstein 2008). Level 1 (L1) is at single pixel level, Level 2 (L2) is at the camera level and finally Level 3 (L3) is at array level. The L1 trigger system in each camera is made up of 499 custom designed Constant Fraction Discriminators (CFDs) (Hall et al. 2003) (one for each PMT). The CFD's employ a constant fraction threshold in order to reduce timing jitters that are caused by changes in the NSB leading to different pulse amplitudes. After passing through a pre-amplifier, the PMT outputs are sent to the input of the CFD. The CFD then triplicates the signal. The first of the triplicated signals is passed through a threshold discriminator (TD) which will trigger if the signal reaches a programmable threshold voltage (usually 45 mV). During non-standard observations the CFD threshold is changed to account for the altered conditions, for example the value is increased to 65 mV during low-moonlight conditions. The increase in threshold value will decrease the number of false positive triggers which are caused by the increased background from the moonlight. The second is attenuated by a fraction and the third is inverted and delayed. The second and third signals are then passed to a zero crossing discriminator (ZCD) which sums the two signals and finds the time at which the summed signal reaches a given fraction of the total signal. A rate feedback loop is applied in real-time to allow for automatic adjustments to the CFD trigger rate under varying noise levels. When a pixel signal surpasses the triggering threshold it is considered a triggered pixel.

At L2, the output from each CFD is passed to a topological trigger system. Here patterns of 3 or more adjacent pixels which all triggered within 6 ns of one another are searched for, if found an L2 trigger is achieved. This removes L1 triggers that were caused by NSB events or PMT fluctuations.

Finally at L3 co-incident triggers from multiple telescopes are searched for. L3 is triggered when it receives L2 signals from more than one telescope within a window of $\sim$50 ns. This timing accounts for the travel time of the signal from the telescopes to a central trigger machine and arrival time delays which are dependent on the telescopes pointing. The L3 trigger will reject single telescope L2 triggers which my occur due to background muons and NSB variations. Upon an L3 trigger occurring, a signal is sent to each telescope to begin a data read out. At this point while the data is being read out no new triggers can occur which leads to some dead time. Figure 10 shows the L2 trigger rates for each telescope and the L3 trigger rates under dark sky conditions.

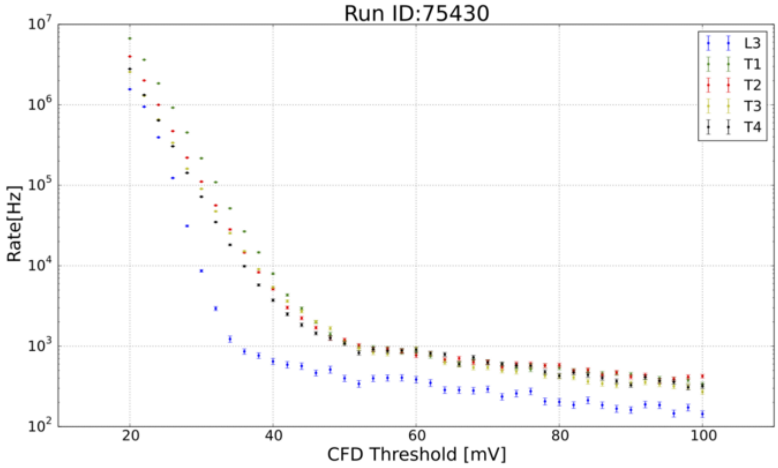

Figure 10: A bias curve showing trigger rates with respect to the CFD threshold taken under dark sky conditions. The L2 rates for each telescope (Green, red, yellow and black for T1, T2, T3 and T4 respectively) are shown as well as the array level L3 rates (Blue).

3.4 Data Acquisition

The flash-analogue-to-digital converters (FADCs) (Rebillot et al. 2003) continuously digitise the analogue signals received from the PMTs at a rate of 500 MSamples/sec. The digitised pixel signals are stored in a ring buffer which has a memory depth of 32 μs. Each FADC board contains 10 channels each of which receives a signal from a single pixel, meaning each telescope's camera (499 pixels) requires 50 FADC boards. The FADC boards are housed in four VME crates. The FADCs have both a "high" gain and "low" gain channel where a gain level is applied. So long as the "High" gain channel remains unsaturated the signal is digitised and written to the buffer memory, in cases where the "High" gain channel becomes saturated, the "Low" gain signal is digitised and written to the buffer memory. Upon an L3 trigger occurring a signal is sent to each telescope's data acquisition system to tell it to read out the previous 24 samples of signals from the camera - during this time buffering must stop and will only resume when the memory buffer is completely read out. The FADC buffer is read out by the VME Data Acquisition (VDAQ) which buffers the pixel-level events before passing them onto the telescope-level Event Builder as well as the event number, type and CFD trigger rates. To handle fluctuations in the NSB the FADC is offset by a value known as the pedestal value. This offset is applied as the FADC is AC-coupled which allows for the measurement of signal fluctuations around the pedestal value. To measure the NSB with the use of the pedestal, artificial events known as pedestal events are measured by forcing the telescopes to trigger in the absence of a real event. These artificial events occur at a rate of 3 Hz. From these artificial events a measure of the NSB can be found by measuring the signal variance with respect to the pedestal as measured by the FADC, this is the pedestal variation (pedvar). The pedvar is estimated from 3 minute averages of pedestal events to account for variation in the NSB over time. The Event Builder can now combine events from each VME crate in order to produce telescope-level events. These telescope-level events are then transferred to the Harvester which will combine the telescope-level events into an array-level event. As this occurs the Harvester also displays a real-time ”Quicklook” analysis of the data which can be used by observers to determine a source’s current state. Finally, the data for each individual run (usually 15-30 minutes) is stored in a custom format VERITAS Bank File (VBF) (VERITAS Collaboration: E. Hays 2007).

3.5 Sky Monitoring

There are multiple instruments on site that allow observers to monitor the sky for clouds, sources of light, etc. during a night of observations. The All-sky Cloud Monitor is a CCD camera situated near T3 that faces directly upwards. Observers use the All-sky Cloud monitor as an easily accessed method to view the sky conditions throughout the night. Along with the All-sky Cloud Monitor T2 and T4 are each equipped with a far-infrared radiation pyrometer (FIR). These FIRs both monitor the temperature of the target area of the sky during an observation runs. If cloud is present in the area of the sky monitored by the FIR observers will see an increase in temperature, this gives a real-time measure of clouds that may block Cherenkov radiation, potential sources of background light or light scattering caused by the cloud. Finally much like the FIRs, VERITAS also employs the use of a LIDAR to measure the fraction of back-scattered light from a zenith pointing laser that is reflected off of clouds, smoke or other atmospheric effects. This measurement can again allow observers to measure the effect of clouds on the data taken.

3.6 VERITAS Pointing Monitor

The VERITAS Pointing Monitor (VPM) consists of a sky camera, focal-plane camera and LEDs which are mounted by each telescope's camera's light cones. During observations the VPM measures the number and location of stars in the FoV, this information is then stored in the VERITAS database for use during analysis. The VPM also gives live updates (one update every 2 seconds) of information such as the number of stars it detects. As observers can expect to see between 50 and 70 stars in the camera's FoV, this can also be used as a means to measure the quality of the observing conditions as less stars will be visible in the presence of cloud or smoke.

3.7 Calibration

In order to ensure that the VERITAS instrument can accurately reconstruct gamma-ray energy and origin regular calibration measurements are performed. The results from calibration measurements can be used to ensure the telescopes' pointing systems remain accurate and any mirror/PMT degradation or other changes that could effect the accuracy of the reconstructed events are accounted for. Some of the common calibrations performed are:

Flasher and Flat Fielding: Where every night a flasher (Hanna et al. 2010) observation run is performed. During the flasher run an LED flasher will flash each telescope's camera with pulses light. At the same time the camera is forced to trigger in order to ensure the pulses are recorded. This allows for corrections to be made to account for any timing or relative gain differences between pixels and to calculate the absolute gain in the PMTs.

Whole-Dish Reflectivity: In order to measure the reflectivity of the mirrors the telescopes are slewed to point at a star which is reflected onto a plate that is fixed to the focal plane. From here a picture is taken using a camera mounted on the OSS that sees both the focal plane and the star. The intensity of the reflected image can then be compared to the intensity of the camera image and a value for the whole-dish reflectivity can be calculated.

T-Point: T-Point measurements are used to correct for systematic errors in the model used by the tracking software. Measurements are taken of ∼50-60 stars which make up a grid covering the sky in a step sizes of ∼30 degrees in azimuth and ∼15 degrees in elevation. By measuring the offset of the star from the centre of the camera when the telescopes are pointed at the star's known location the pointing model can be updated.

3.7.1 Gain-Threshold Factors

As mentioned in Section 3.1 the VERITAS instrument and in particular the reflectivity of the mirrors will degrade over time. As this level of degradation has an effect on the results produced by the instrument, understanding and addressing its effect is crucial. In order to account for the ever-changing nature of the telescopes, a set of gain-threshold (GT) factors based on measurements of the instrument's reflectivity and gain (Adams et al. 2022) are produced for every season (twice annually). As the VERITAS mirrors degrade and their reflectivity decreases, the observed size of showers will also decrease. This means that the lookup tables which describe the energy of the incident photon based on the observed shower size will become more and more inaccurate as the mirrors' reflectivity decreases. In order to measure and account for the level of degradation of the mirrors a reflectivity factor is calculated for each season, this is given as $r_i = R_i/R_{i,MC}$ where R_i is the measured reflectivity for a single telescope i in a chosen season and $R_{i,MC}$ is the Monte Carlo simulated reflectivity for a single telescope i in a chosen season. Figure 11 shows how the mirror reflectivity factor has decreased throughout V6.

Alongside the mirror reflectivity measurements, measurements of the absolute gain of the cameras' PMTs are also taken. Much like the mirror reflectivity factor, a gain factor is given by $g_i = G_i/G_{i,MC}$ where G_i is the measured average gain of the PMTs in telescope i and $G_{i,MC}$ is the average gain of the PMTs in telescope i according to Monte Carlo simulations. A time-dependent evolution of the gain factors is shown in Figure 12. A more detailed breakdown of how the measurements are used in obtaining mirror reflectivity and gain factors is presented in (Adams

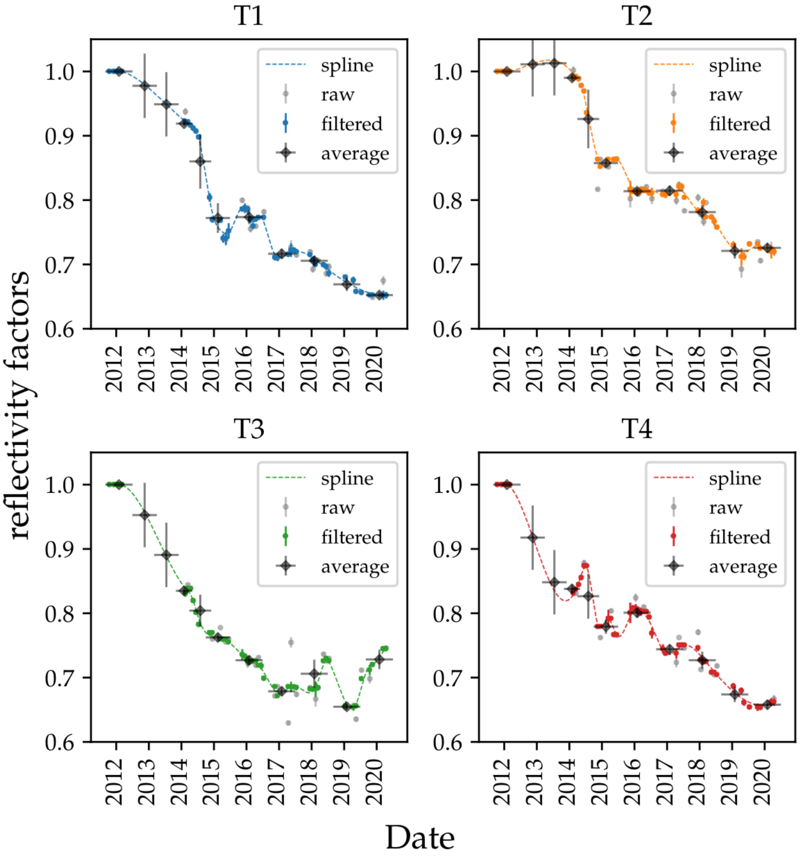

Figure 11: Mirror reflectivity factors for each VERITAS telescope from the beginning of V6. The large error bars on the early years are due to less common or no reflectivity measurements from those years. (Adams et al. 2022)

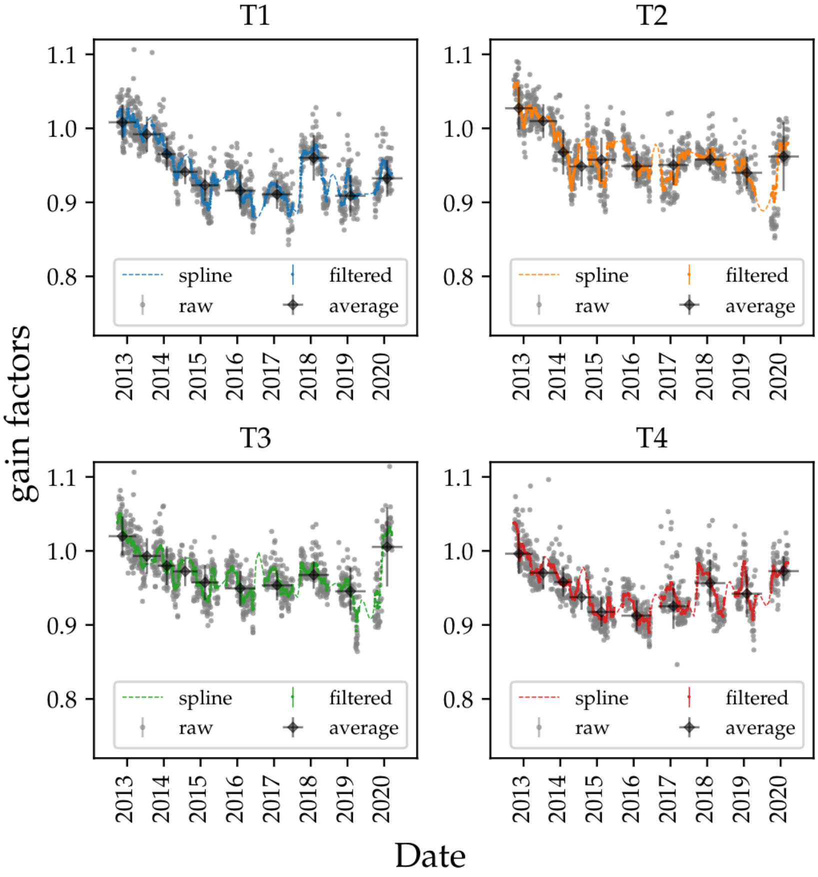

Figure 12: Gain factors for each VERITAS telescope from the beginning of V6. (Adams et al. 2022)

et al. 2022). Finally in order to get a measure of the total effect of both the mirror degradation and drop in absolute gain a total throughput of each telescope can given as the product of g_i and r_i this is shown in Figure 13. Now that both the gain and reflection factors are known and combined to give the GT factors, the GT factor can be applied directly to pixel and pedestal charge values in simulations used to produce lookup tables thus accounting for any changes in reflectivity and gain.

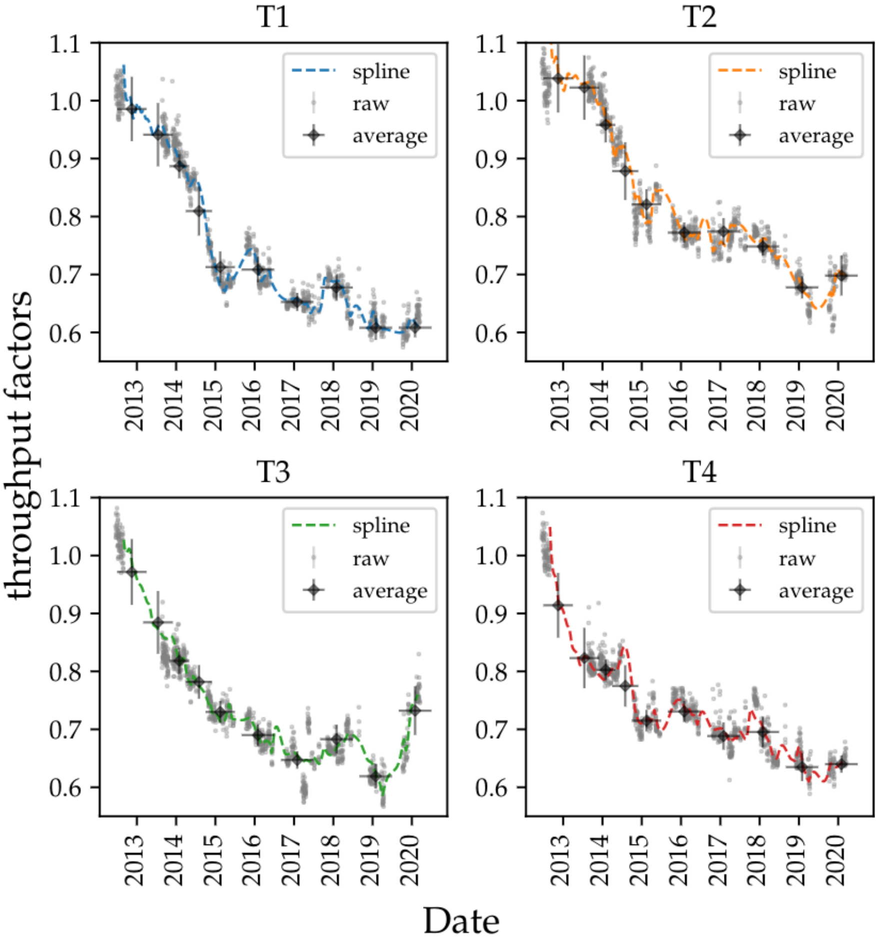

Figure 13: The throughput factor achieved from the combination of the reflectivity factor (11) and the gain factor (12). (Adams et al. 2022)

4 VERITAS Analysis Technique

The VERITAS analysis chain focuses on three levels: firstly pixel data is calibrated to obtain the charge. The pixel charges are then calibrated and telescope level images are produced. Single telescope level images are then combined to produce array level images of each shower, these array level images are used to find the geometrical properties of the shower. From their geometrical properties each shower is characterised as either a gamma-ray-like shower or hadronic shower with all hadronic showers being cut from the analysis. Finally a background estimate is made which is used to determine if there is any statistically significant excess gamma-ray count from the observed target.

4.1 Trace Analysis

When detected by the PMTs in the camera, Cherenkov pulses are recorded by the FADCs as a voltage-vs-time signal, an example of which can be seen in Figure 14. The point at which the signal rises to 50% of its greatest value is the arrival time T_0 of the pulse, in the case of Figure 14 this is the beginning of the grey area with the end of the grey area signifying the end of the pulse where the signal drops below 50% of its greatest value. The FADC pulse is offset by the pedestal (Section 3.4) value to handle fluctuations in the NSB during the run. In order to minimize the amount of NSB that is included in the integrated charge, a double-pass trace integration method is used (Holder 2005). The first pass uses a wide integration window (8 samples) in order to find T_0 of each pixel. This image is then cleaned and parameterised as per Section 4.3. Using the cleaned and parameterised image a line can be fit to the arrival time of a pulse as a function of its position along the image axis. The slope of this line is then used to obtain a new T_0 which is the beginning point of a shorter integration window (6 samples).

4.2 Image Cleaning

The island cleaning method (Fegan 1997) used in standard VERITAS analysis to clean images is implemented as follows: Pixels are first classified by their signal-to-

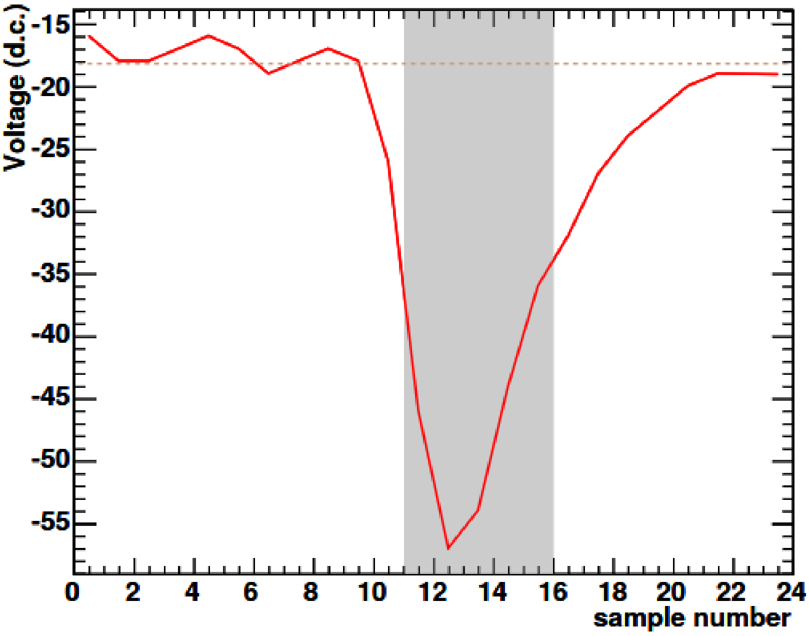

Figure 14: The FADC output of a PMT event. The horizontal dashed line shows the pedestal level, the grey area shows the integration area beginning and ending at half the greatest value of the signal.

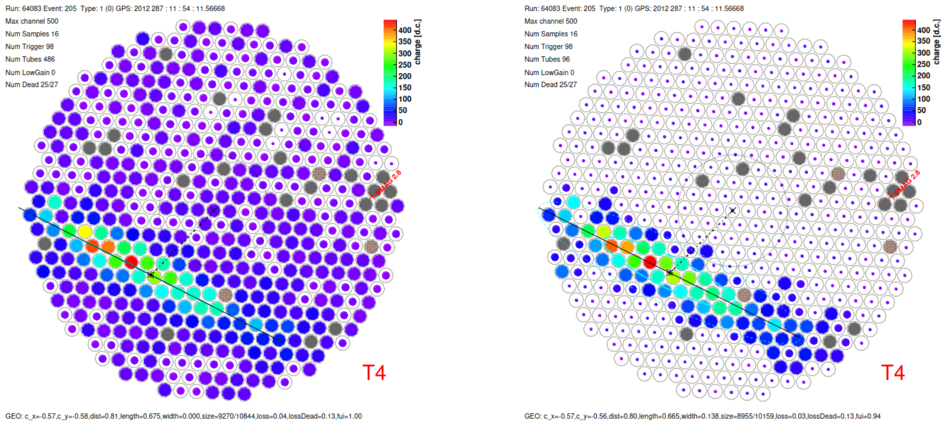

Figure 15: Example of the charge in each pixel from a gamma-ray event before (left) and after (right) cleaning has been performed. Black pixels are either dead or surpressed pixels.

noise ratio (pedvar) as either bright, boundary or empty. A bright pixel is defined as a pixel with a signal-to-noise ratio of 5 or greater, a boundary pixel is defined as a non-bright pixel which is next to a bright pixel and has a signal-to-noise ratio of 2.25 or above and any pixels with a signal-to-noise ratio less than 2.5 is classified as an empty pixel. Any pixel classified as empty will be immediately removed from the image analysis. Following the classification of all pixels, any isolated bright pixels with no neighbouring boundary pixels will also be removed before the next stage of the analysis. The remaining bright and boundary pixels are now considered to be due to a Cherenkov shower. Figure 15 shows the image of a shower taken by VERITAS before and after cleaning.

4.3 Image Parameterisation

The cleaned shower image will now be parameterised into "Hillas parameters" (Hillas 1985) which can be used to discriminate gamma-ray induced showers from cosmic-ray induced showers. The Hillas parameters are found by performing a moment analysis using the signal and positions of the image pixels (Fegan 1997). The key parameters used in the VERITAS image paramertisation are both described below and are also shown in Figure 16.

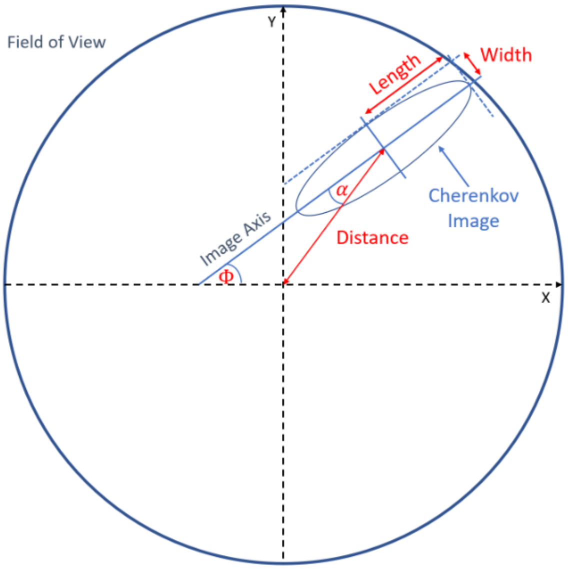

Figure 16: Visualisation of the Hillas parameters used in image parameterisation. All parameters are the same as described in Section 4.3. Not shown is the loss parameter which measures the fraction of the ellipse shown which is cut on the edge of the camera.

Size : The integrated charge of all image pixels. This is the brightness or intensity of the shower as seen by the telescope.

Centroid : The location on the camera of the centre of gravity of the image.

Distance : The distance from the centre of the camera's FoV to the centroid of the image.

Length : The root mean squared (RMS) of the charge along the major axis of the shower.

Width : The RMS of the charge along the minor axis of the shower.

Loss : The percentage of the size parameter which comes from pixels along the edge of the camera.

While unlike the other parameters the *loss* parameter does not necessarily describe the image itself, it is used to determine when to reject showers which are cut off by the edge of the camera.

4.4 Event Reconstruction

Now that they have been cleaned and parameterised, images of the same event from multiple telescopes can be combined in order to produce a stereoscopic reconstruction of the event. As a stereoscopic reconstruction of an event offers a more detailed view through multiple images it acts as a significant improvement to a single telescope reconstruction. The first stage of reconstructing a shower image is to cut events that do not contain a minimum number of pixels in the image, minimum total charge in the image and or exceed a maximum loss value.

4.4.1 Geometrical Reconstruction

To begin the event reconstruction the origin of the shower and core location are first reconstructed. As a shower will develop along the direction of the incident gamma-ray its origin must be along the major axis of the image. The shower's origin can therefore be found by finding the point at which two or more images of the same shower intersect, as shown in Figure 17. This is done by first superimposing the major axis of the shower image from each telescope onto a common sky plane the point of intersection can then be estimated. Unfortunately due to uncertainties in measurements it is rare that a single intersection point is seen but instead $N\left(N-1\right)/2$ (for N telescopes) intersection points are seen. In the case of multiple intersection points a single origin point can be found from a weighted average of the intersection point of each telescope pair. Each image pair is assigned a weight as defined by the following equation:

$$weight_{1,2} = \left(\frac{1}{size_1} + \frac{1}{size_2}\right)^{-1} \times \left(\frac{width_1}{length_1} + \frac{width_2}{length_2}\right)^{-1} \times sin\left(\theta_{1,2}\right) \tag{3}$$

where size, length and width are described in section 4.3 and $\theta_{1,2}$ is the angle between the two axes. By projecting the intersection of the showers on a common ground plane, the location at which the gamma ray would have hit the Earth if it had not interacted with the atmosphere is found. From the location at which the shower core would have hit the ground, the *impact parameter* (R) can be found.

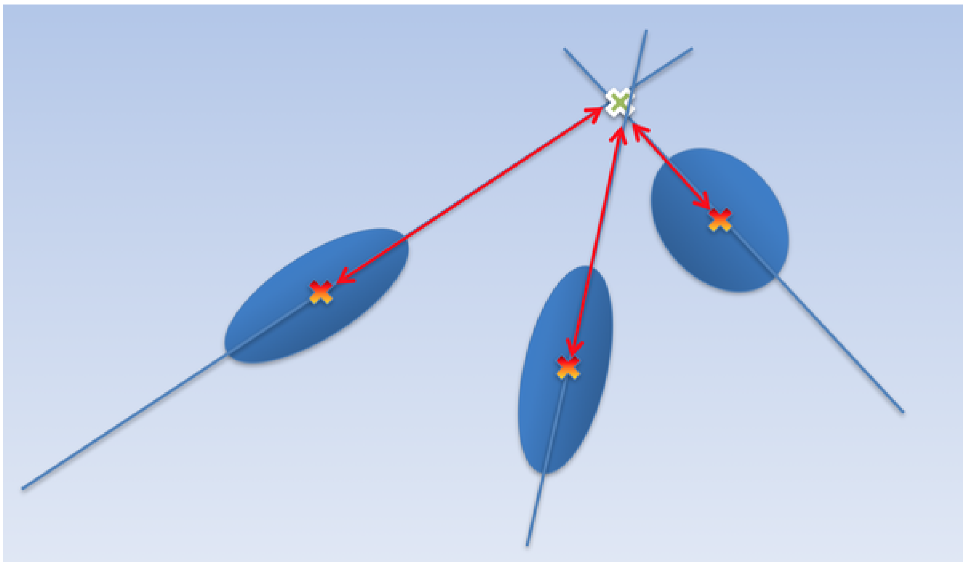

Figure 17: An example of using the weighing of the major axes of showers seen by three telescopes to reconstruct the real source position (green cross). The centre of gravity of each individual shower is shown by a red cross.

The impact parameter is the distance between the centre of the telescope array and the core location in the ground plane.

The *emission height* is estimated as the average emission from the pairwise combination of images, the values for which are obtained using the image centroids, impact parameters and source location (Aharonian et al. 1997). As hadronic showers are often induced deeper in the atmosphere, the emission height is useful when attempting to reject hadronic showers, it can also be used when rejecting badly reconstructed showers.

4.4.2 Energy Estimation

The energy of an incident gamma ray can be estimated through the comparison of the total integrated charge (brightness) of the shower image and the impact parameter. This is because the brightness of a shower will decrease with the distance between the shower and observer, with more energetic showers appearing brighter than less energetic showers. The energy of a shower can therefore be estimated with the use of look-up tables which contain values for shower energy as a function of integrated charge and impact parameter. Lookup tables are produced from Monte Carlo simulations of gamma-ray events for a range of combinations of epoch, zenith angle, NSB level and wobble offset to ensure complete coverage. The energy of an event can be found by averaging the estimated energy of the event according to each telescope:

$$E = \frac{\sum_i^N \frac{E_i}{\sigma_E^2}}{\sum_i^N \frac{1}{\sigma_E^2}} \tag{4}$$

where E is the estimated energy of the simulated shower and σ_E is the 90% energy distribution, both of which are obtained from the lookup table.

4.5 Gamma/Hadron separation

After the events have been reconstructed, the data still consists of a combination of both gamma-ray events and background cosmic-ray events. It is therefore necessary to attempt to separate as many gamma-ray like events from the background events. As a cosmic-ray induced shower should appear different to a gamma-ray induced shower, this separation is done by applying a set of cuts to the shapes of the shower images. Using the stereo images of each shower a mean scaled width and length (MSCW/MSCL) for a shower can be defined as (Krawczynski et al. 2006):

$$MSCW = \frac{1}{N}\sum\left(\frac{width - w\left(R,S\right)}{\sigma_w\left(R,S\right)}\right) \tag{5}$$

$$MSCL = \frac{1}{N}\sum\left(\frac{length - l\left(R,S\right)}{\sigma_l\left(R,S\right)}\right) \tag{6}$$

where $w(R,S)$ and $l(R,S)$ are median length and widths and $\sigma_{w/l}(R,S)$ are their 90% distributions derived from Monte Carlo simulations of gamma-ray showers, the values for which are found in look-up tables. An example of the distribution of MSCW and MSCL can be seen in Figure 18 where the distribution of gamma-ray events is expected to be a Gaussian centred on 0 and cosmic-ray background events to be centred on larger values. It is clear from Figure 18 that cosmic-ray showers will have longer and wider showers than gamma-ray showers. Cuts can therefore be applied to the MSCW and MSCL in order to best remove background

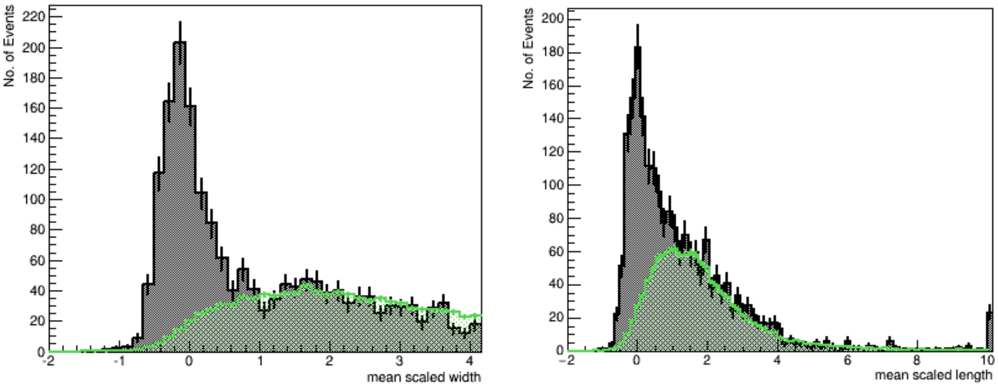

Figure 18: Simulated examples of the MSCW (left) and MSCL (right) distributions of both *ON* region events (black histogram) and *OFF* region events (green lines). The difference between their distributions is used to differentiate the two types of showers.

Cut	Min MSCW	Max MSCW	Min MSCL	Max MSCL	Min Size (Digital Counts)
Soft	0.05	1.1	0.05	1.3	400
Medium	0.05	1.1	0.05	1.3	700
Hard	0.05	1.1	0.05	1.4	1200

Table 1: A list of the cuts used in a standard VERITAS analysis.

events from gamma rays, although some background will remain. The values at which the cuts are made are calculated a priori and verified on control data sets. A range of cuts have been optimised depending on the spectral hardness of a source. ”Soft”, ”Medium” and ”Hard” cuts are optimised for sources with respective spectral hardness, the values for each are shown in Table 1. Hard cuts have higher energy threshold and are more strict in order to minimise the number of cosmic ray events. Soft cuts on the other hand have a lower energy threshold and are less strict, allowing for an increase in the signal at lower energies but at the expense of increasing the background.

4.5.1 Background Estimation

A method of calculating the average background in the region of interest is required in order to determine the number of excess gamma-ray-like events there. Multiple different methods can be employed in order to do so but all of which rely on the principle of observing an area of the sky with no known source of gamma rays and counting the number of gamma-ray-like events observed in that region over the same exposure time as the source observation. In order to ensure the background estimation is as accurate as possible, the data are sampled from a large area taken at as close to the source region as possible i.e. the same elevation and azimuth and then averaged to match the size of the region of interest. The *ON* region is a circular region located on the observed target which in the case of a point-source analysis is the size of the VERITAS point spread function (PSF). Within the *ON* region we expect to see the gamma-ray events produced by the target being observed as well as some background gamma-ray-like events. An observation mode called "wobble" is commonly used when observing a source. In a wobble observation the target is offset from the centre of the camera in one of the four cardinal directions by a set distance (usually 0.5° for a point source) the direction of wobble is changed every run to ensure consistent coverage. The shape and location of the *OFF* region(s) will differ depending on which background estimation method is used. When a known source of gamma rays, a bright star or other source of background falls into the camera's FoV an exclusion region is used to omit it from an analysis, an exclusion region is also placed around the *ON* position to prevent gamma-rays from being included in the background estimation for other points in the camera. Some commonly used background estimation methods are :

The reflected region method : multiple *OFF* regions are defined as a ring of concentric regions identical in size to the *ON* region that are offset the same distance from the centre of the camera's FoV. Any wobble region that overlaps an exclusion region is completely removed from the analysis. The total number of events measured across all *OFF* regions is finally averaged by the number of *OFF* regions to give a final estimation of the number of background events in the *ON* region. An

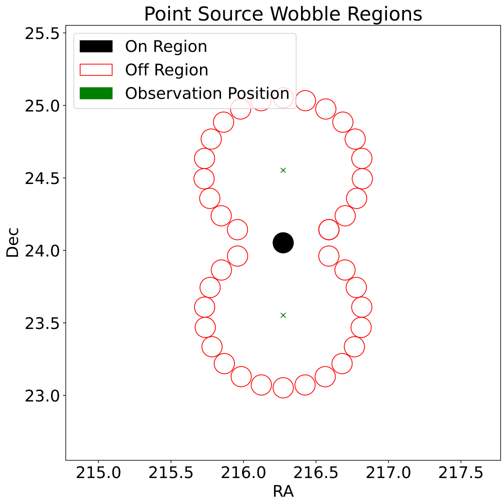

Figure 19: A visualisation of the reflected region (wobble) background estimation method using both a north and south wobble

example of this showing both a north and south wobble can be seen in Figure 19. This is the method used in this analysis.

The ring background method : uses an *OFF* region defined as a solid ring around the *ON* whose two radii are $r_1 = r_{offset} - r_{ON}$ and $r_2 = r_{offset} + r_{ON}$. The number of events counted in the *OFF* region is averaged by the ratio of the areas of the *OFF* and *ON* region. Any event which falls in an area of overlap between the *OFF* region and an exclusion region is removed from the analysis. A visualisation of which can be seen in Figure 20.

4.5.2 Source Detection

Upon performing the source-region analysis and background estimation as discussed in section 4.5.1, a value for the number of *ON* events N_{on} and total number of background events N_{off} is obtained. A normalisation factor α is then defined which will scale the background observations to match the source observations, this is the

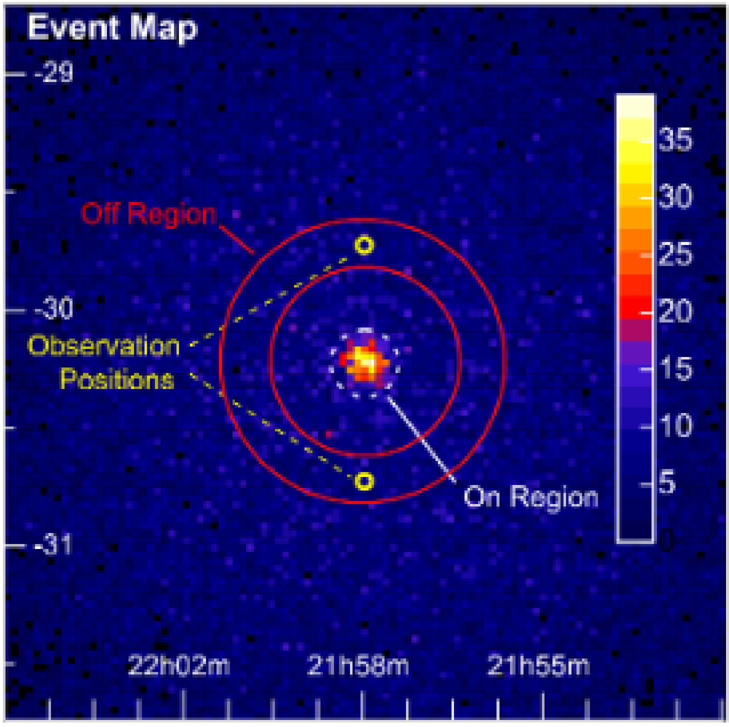

Figure 20: A visualisation of the ring background estimation method with both a north and south wobble shown (Berge, Funk, and Hinton 2007)

ratio of the area of the background regions to the source region. For example if the reflected region model is used with equal exposure times for both the *ON* and *OFF* observations and 5 reflected regions are used to sample the background the normalisation factor will be $\alpha = \frac{1}{5} = 0.2$. Now from background subtraction the number of gamma-rays produced by the target (the excess) is $N_s = N_{on} - \alpha N_{off}$. A positive excess does not yet guarantee that the target has been detected above the background, statistical fluctuations in the background rates can lead to a positive excess even in the absence of a gamma-ray source. The significance of the measured excess above the background is given by Li and Ma equation 17 (Li and Ma 1983):

$$S = \sqrt{2}\left\{N_{on}ln\left[\frac{1+\alpha}{\alpha}\left(\frac{N_{on}}{N_{on}+N_{off}}\right)\right] + N_{off}ln\left[(1+\alpha)\left(\frac{N_{off}}{N_{on}+N_{off}}\right)\right]\right\}^{\frac{1}{2}} \quad (7)$$

In gamma-ray astronomy a significance value of $S \geq 5$ is conventionally required in order to claim a detection. This level of significance is equivalent to a 0.00002% probability that the result observed excess is caused by a statistical fluctuation.

4.6 Image Template Model Analysis

The use of maximum likelihood methods (MLM) with shower-image templates in the reconstruction of gamma-rays has been shown to improve both the resolution and sensitivity of IACT analysis (de Naurois and Rolland 2009) (Le Bohec et al. 1998) and has been implemented by H.E.S.S. in their ImPACT algorithm (Parsons and Hinton 2014). VERITAS has now also implemented a shower-image template maximum likelihood gamma-ray reconstruction method, known as ITM (Christiansen and VERITAS Collaboration 2017). The ITM method consists of selecting simulated images that best match observed shower images. By comparing these images a more accurate estimate for the shape and size of the shower image can be derived which will lead to a more accurate gamma-ray reconstruction. Some of the key advantages of the ITM method include the ability to better reconstruct truncated events or events with missing pixels. The VERITAS ITM simulations are generated for a range of values of energy, zenith, azimuth, core location and depth in the atmo-

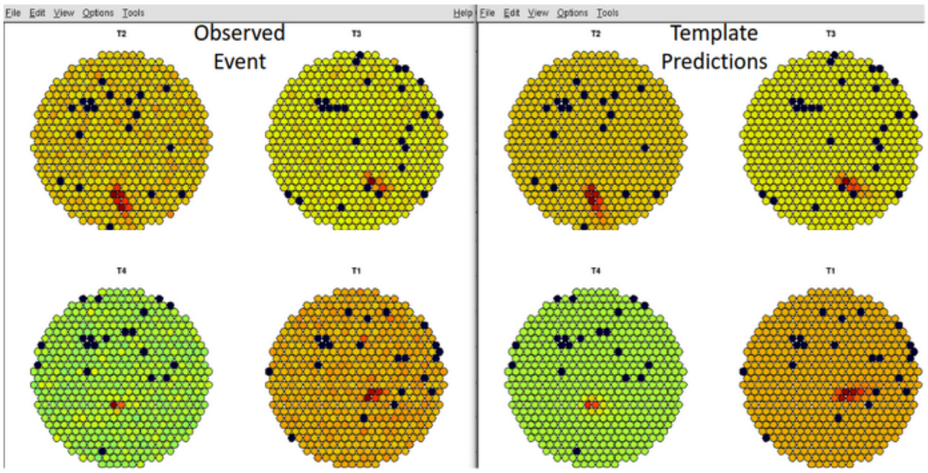

Figure 21: A gamma-ray event on each VERITAS telescope both before and after the implementation of ITM. The colour gradient shows pixel current with black meaning the pixel is missing or suppressed. For example the group of black pixels in the upper left coincide with a bright star in the image. Source (Christiansen and VERITAS Collaboration 2017)

sphere of the first interaction (Vincent and VERITAS Collaboration 2015). From each template the expected average number of photoelectrons a PMT will detect based on the six previously listed parameters can be found. The templates can be used to compare an image consisting of template pixels to the observed image and calculate a likelihood which will be maximised to find the optimal gamma-ray parameters. In Figure 21 an example of an observed gamma-ray event (left) beside the ITM predicted equivalent (right) from each VERITAS telescope is shown. Due to the improvement in angular resolution a reduced angular cut can now be used in the point-source analysis thus leading to a greater sensitivity due to a reduced *ON* region background and an increase in the number of *OFF* regions. ITM also allows for a more accurate measure of the background regions due to the better reconstruction of events that occur near bright stars in the FoV. The sensitivity improvements as a result of ITM have been tested using both soft, medium and hard-spectrum sources where a 25% improvement in sensitivity has been observed for dim soft-spectrum sources and a 35% improvement for medium to hard-spectrum sources.

4.7 VERITAS Analysis Software

The VERITAS Gamma-ray Analysis Suite (VEGAS), is one of the two VERITAS software analysis packages through which all analyses must be performed prior to publication. The primary analysis of the data used in this work was performed using VEGAS while any secondary/validation was performed using EventDisplay (the second of the two packages).

4.8 Extended Source Analysis

Although most of the standard VERITAS analysis methods will translate directly from a point-source analysis to an extended-source analysis there are some factors that must be considered. It is known that due to atmospheric depths, a gradient in gamma-ray rates will occur with elevation. This will have an impact on an extended-source analysis as the larger source- and background-regions will lead to an increase in background and gamma-ray rates, thus making the gradient's effects visible. Section 4.5.1 discusses how for every data run the target which is being observed is offset by a set distance in each cardinal direction from the centre of the camera. If we consider the case of north and south offsets (east and west are ignored in this discussion as the gradient is only elevation dependant) there will be a δElevation $= 1°$ between the center of the camera for each run, this results in a δElevation $= 2°$ between the centres of the most extreme background regions. This leads to a difference in background rates between runs with a north and south wobble. To measure the effect of this, one can take observations of a dark area of sky and compare the *ON* and *OFF* region gamma-ray rates. For this investigation 30 hours of VERITAS observations of OJ 287 in a quiet state were used. A standard ITM analysis was then performed with four different angular cuts : 0.07°(point source cut), 0.1°, 0.15° and 0.2°. In every case the gamma-ray rate per degree per exposure time for each background region is measured. If the gradient in gamma-ray rate is only elevation dependent and ensuring we use symmetrically positioned wobble regions the average rates will average out across north and south wobbles and agree with the gamma-ray rates in source region. Figure 22 shows the *ON* and *OFF* rates from the analysis of OJ 287 using an angular cut of 0.2°. We can see the

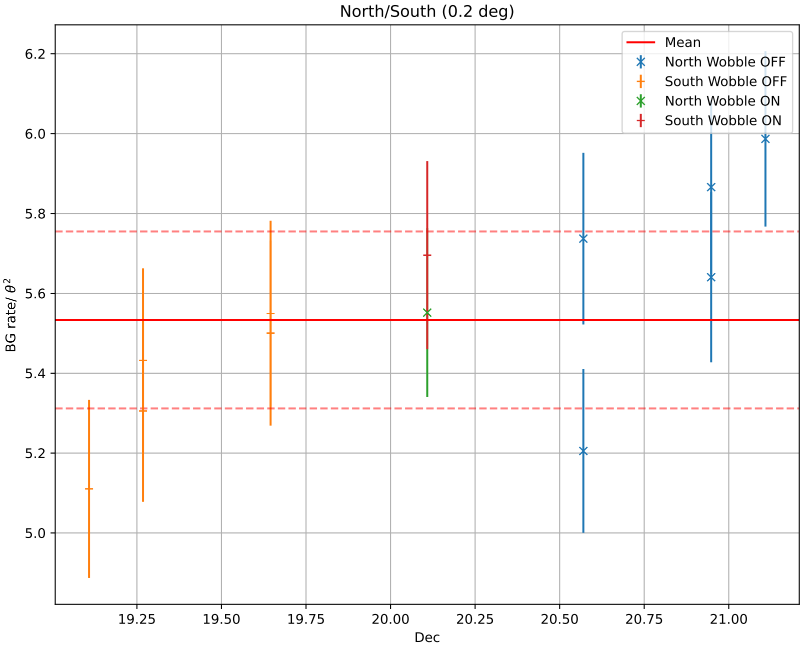

Figure 22: *ON* and *OFF* rates from an area of dark sky with no known gamma-ray source viewed under two different wobble offsets North(Blue) and South(Orange) with symmetrical *OFF* regions. The average background rate and error (red solid and dashed) is used to measure the effect of the camera gradient.

averaged background rate (horizontal red line) falls within the error bounds of the *ON* region rates and the gradient is negated by the use of symmetric *OFF* regions.

4.9 VERITAS Instrument Response Functions

VERITAS IRFs are developed on twice annual bases as to account for changes in the instrument and atmospheric effects. IRFs will also vary with azimuth, elevation and night sky background. This means that in order to account for differences between IRFs based on the observing conditions and seasons from which the observations used in this study were taken, weighted IRFs are used in this analysis. Figure 23 shows an example of a weighted Effective Area (EA) used in the analysis and an

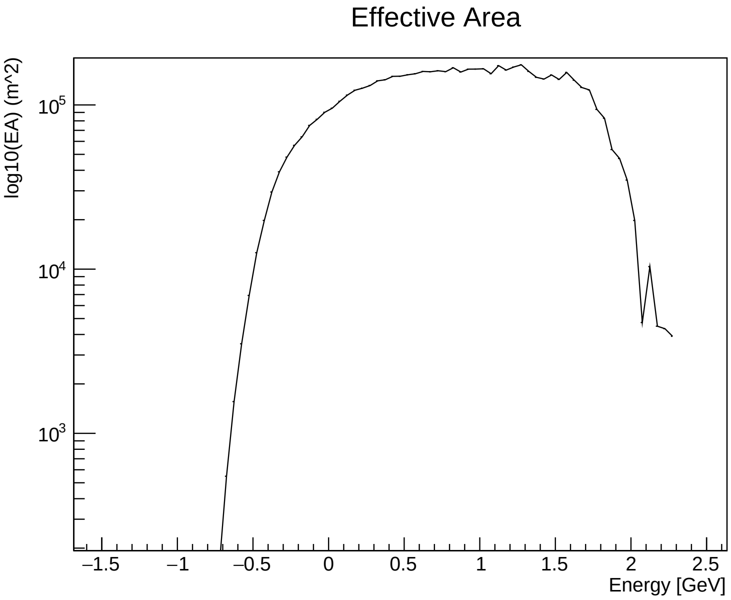

Figure 23: Example of a weighted EA used in the DM MLE.

example of a weighted energy dispersion matrix is shown in Figure 24.

4.10 Effective Area

The Effective Area (EA) of a telescope defines the telescope's ability to detect a gamma-ray at a particular energy by combining the efficiency at that energy with the geometrical area of the telescope. In order to calculate the VERITAS energy dependent EA, simulated gamma-ray showers are dropped over a large area A_0, these simulated gamma rays are then passed through the VERITAS analysis pipeline - in particular the event selection stage. We then count the number of events which pass selection and as a result the EA(E) can be described as (Mohanty et al. 1998):

$$A(E) = A_0 \frac{N_{detected}(E)}{N_{simulated}(E)} \tag{8}$$

The EA of an instrument is not just energy dependant, but is also affected by parameters such as the zenith and azimuth of the observation target, the night sky background level and pointing offset, to ensure full coverage EAs are produced for a

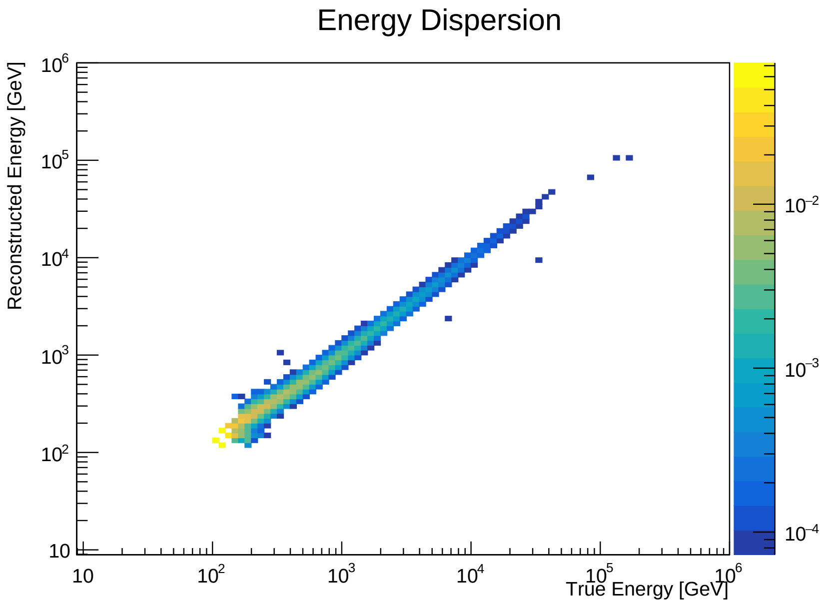

Figure 24: Example of a weighted energy dispersion matrix.

range of each parameter. As the response of VERITAS changes over time, the EA must be regularly measured to account for the effects of the change of the instrument response. In Figure 25 we can see the shape of the VERITAS EA as well as see the effects the different array epochs, applying UV filters and operating in reduced high voltage have on the EA.

4.11 VERITAS Point Spread Function

As the VERITAS point spread function (PSF) is not included in VEGAS IRFs a method of deriving it is required for this analysis. There are two methods employed in this thesis to produce and validate the VERITAS PSF. One method using an actual VERITAS data set and the second using the simulations used in the production of other VERITAS IRFs. At the beginning of this research VERITAS IRF production simulations were under production and were not available for PSF production. For this reason a data-derived VERITAS PSF was first produced. Upon the completed production of the simulations, they were then used to produce a simulation based PSF which would be used in the final analysis.

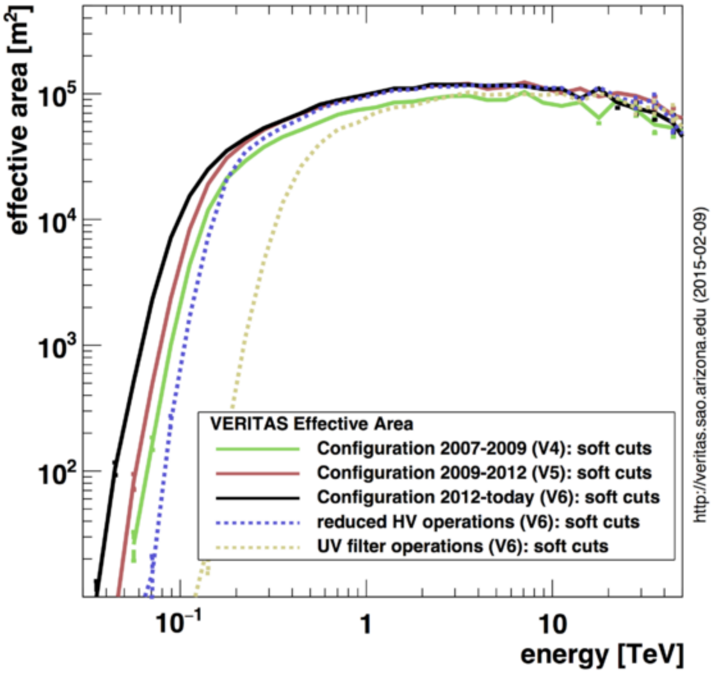

Figure 25: Effective area as a function of gamma-ray energy (elevation: 70 deg) for various different instrument epochs and conditions

4.11.1 Data-Derived PSF

A point source with a large data set which spans the time-frame of observations is required to derive the VERITAS PSF from data. The Crab Nebula is point like and the brightest steady source in the gamma-ray sky. It is often used in VERITAS calibrations and for this reason has an extensive data set of 1044 total hours since 2007. For these reasons it is chosen to be the source from which to derive the PSF.

4.11.1.1 Production Method

The method used to derive a PSF from data is as follows: First the data undergoes a quality check. The good quality data is then analysed using the standard VEGAS methods. The excess events (found using a reflected region method) are then extracted. Finally these events are binned by energy and distance from the centre of the *ON* or *OFF* region they are found in degrees, giving an energy dependant PSF. There is one major obstacle to overcome when deriving the VERITAS PSF from source data and that is the limitations on statistics imposed by the θ cut (reflected region size) used when performing the standard analysis which is discussed in Section 4.11.1.3.

4.11.1.2 Data Set

The Crab Nebula data set used to derive the PSF contains $\sim$ 225 hours of 0.5° wobble offset data spanned across all VERITAS seasons between December 2007 and March 2020. This is the same data set used in (Adams et al. 2022) and was used in this analysis for this reason.

4.11.1.3 θ Cut Limitations

While an ideal PSF would account for events all the way to the edge of the VERITAS camera, this is not possible for a purely data-based PSF. As excess events are used to derive the PSF at least one wobble background region is required. This means that the θ cut used in the analysis cannot exceed the size of the wobble offset (0.5°), for this reason a limit of 0.4° θ cut was applied. With a θ cut of 0.4° only one wobble background region can be formed, leading to two further problems: due

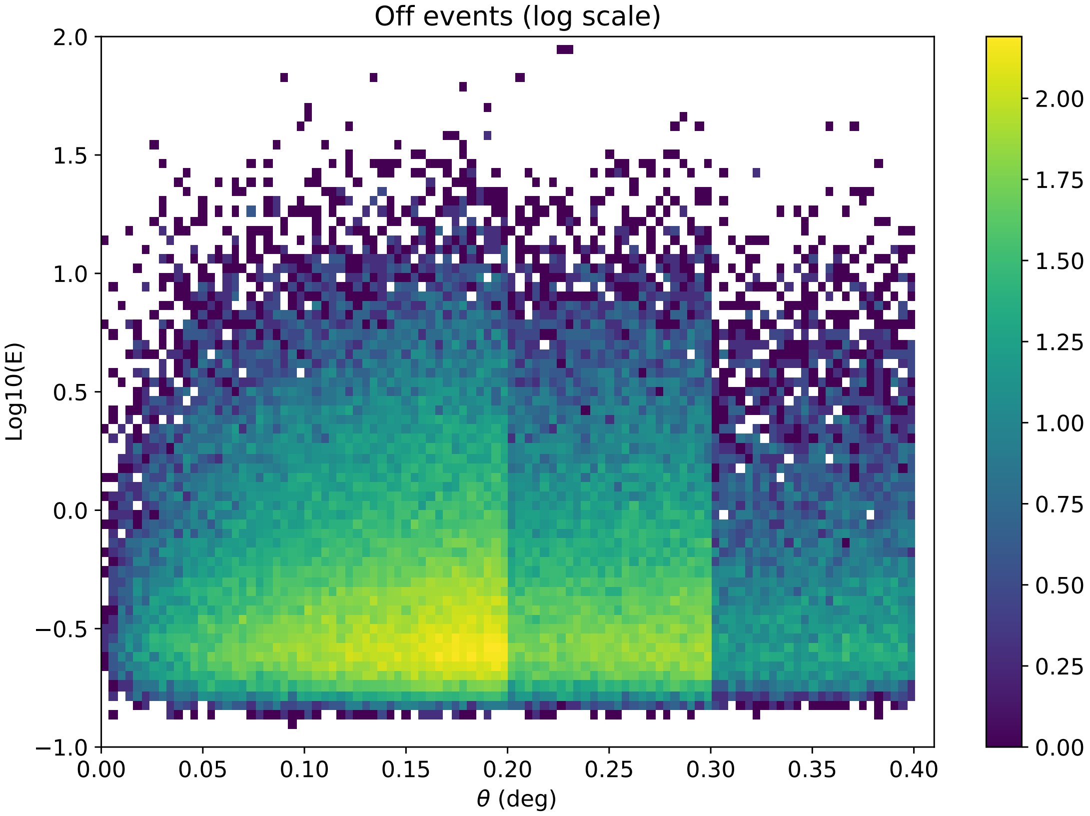

Figure 26: Combination of Crab *OFF* events from all θ cuts prior to α correction

to the presence of only one wobble region the number of *OFF* events is greatly reduced, leading to a less accurate excess and in the case of the wobble region being rejected due to overlap with an exclusion region the run is rendered unusable. This reduces the total exposure time to ~ 60 hours. To overcome this 3 different θ cuts of $0.2^\circ, 0.3^\circ$ and 0.4° are used in the analysis and combined in the PSF production as seen in Figure 26. As the θ cut increases, the number of wobble regions will decrease and as a result as will the number of *OFF* events counted. This results in the hard edges at the point of each change in θ cut which can be seen in Figure 26. In order to handle this a normalisation factor α is used to account for the changes in both the number of background regions and in the case of the 0.4° cut the change

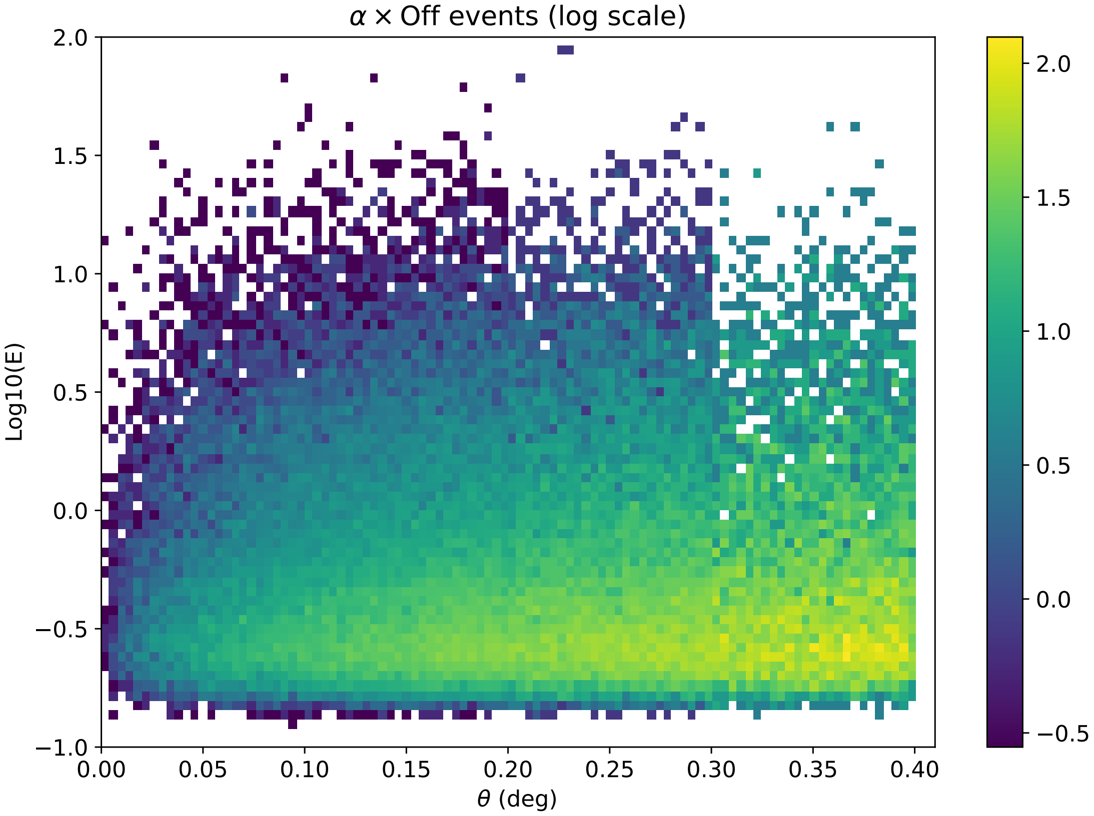

Figure 27: Combination of Crab *OFF* events corrected by α

in exposure time. The smoothed background events can be seen in Figure 27. Now that the background region has been smoothed the excess events can be obtained by subtracting the α-adjusted *OFF* events from the *ON* events. First shown in Figure 28 is the *ON* events from which the smoothed background will be subtracted then Figure 29 shows the excess events from which the PSF will be extracted. Finally the excess events are binned in energy and θ producing an energy dependent PSF as shown in Figure 30

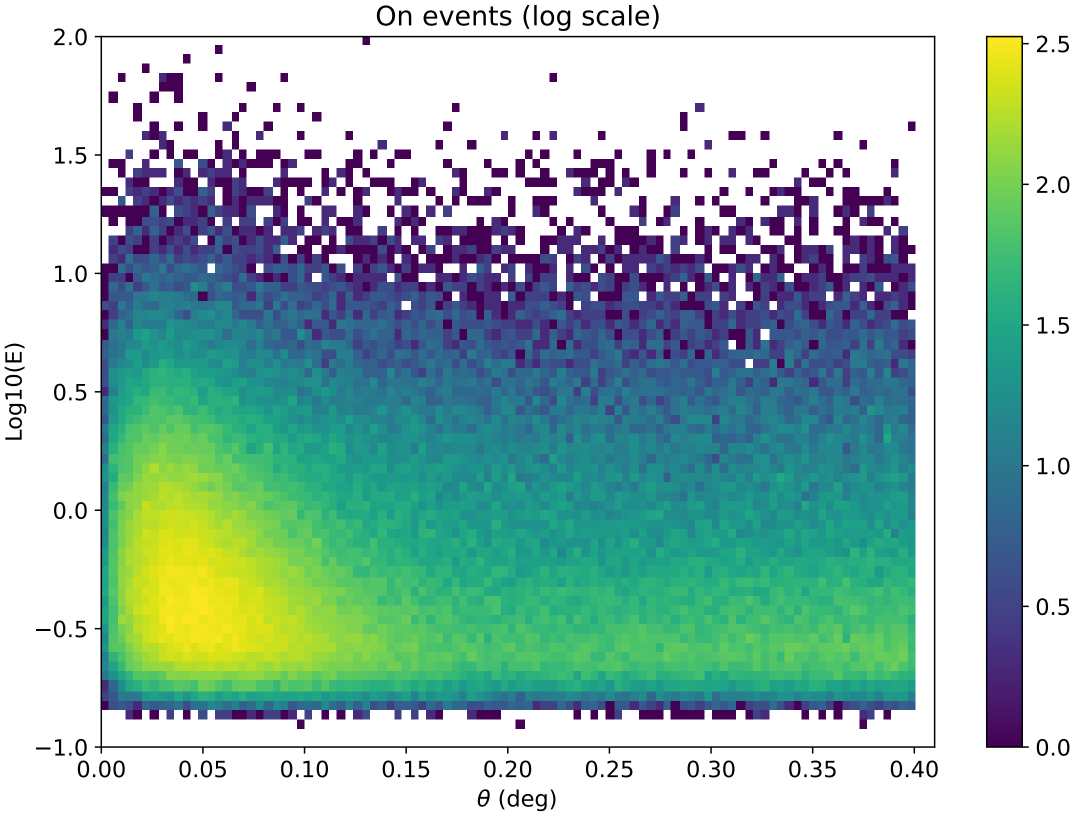

Figure 28: Combined Crab *ON* events from all θ cuts.

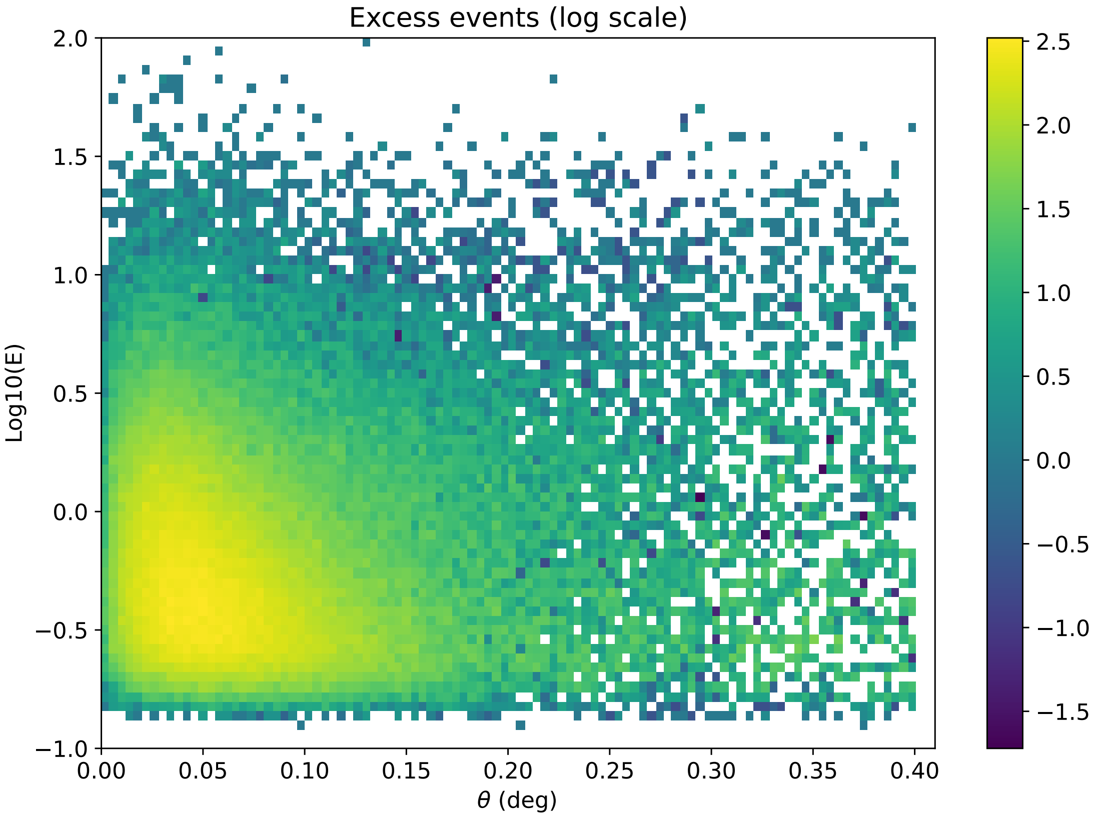

Figure 29: Excess Crab events after adjustments for varying θ cuts. This is where the PSF is extracted from.

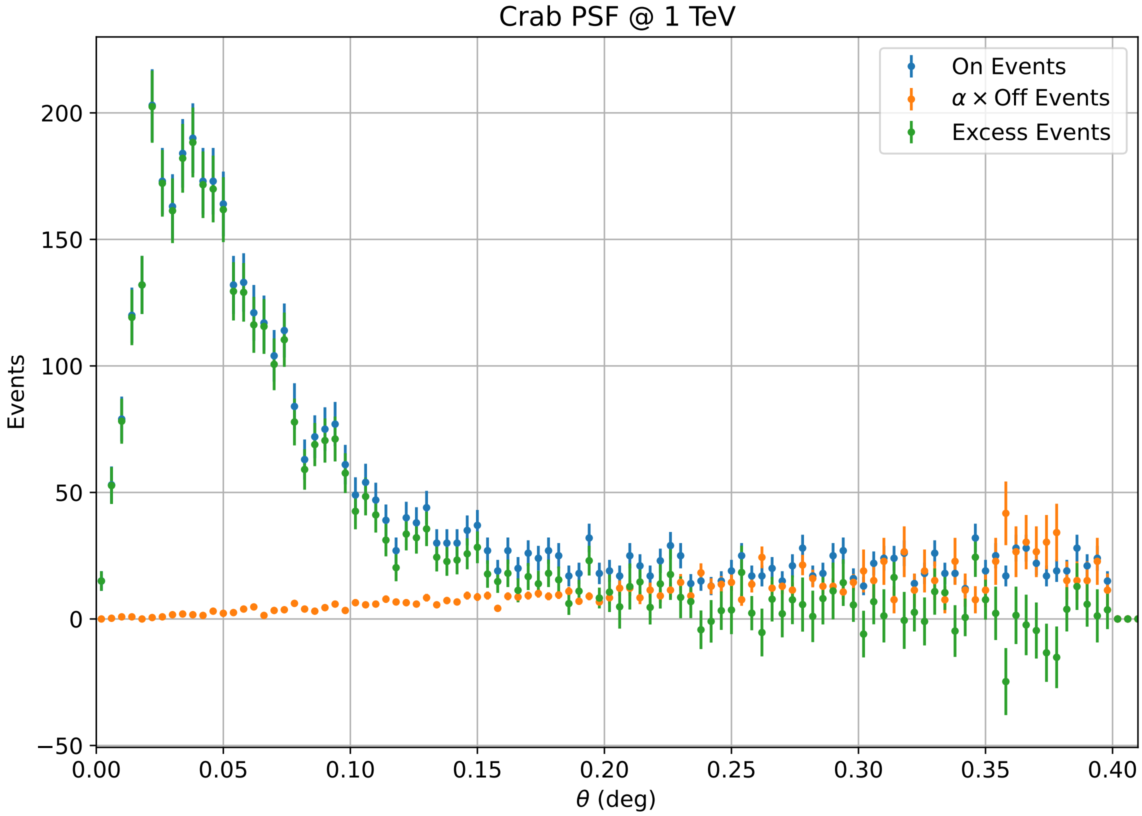

Figure 30: Crab *ON* events (Blue), alpha adjusted *OFF* events (Orange) and excess events (Green) of the Crab nebula at 1 TeV.

4.11.2 Simulated PSF

In order to produce the VERITAS IRFs for each season simulated point source data is passed through the analysis pipeline giving us a number of simulated source gamma-ray events. These simulation files contain a far greater number of gamma-ray events than the Crab data set and are not effected by the θ cut limitations discussed in Section 4.11.1.3 as the simulations contain no background events. This means the simulated events can all simply be binned by energy and θ to produce an energy dependant PSF.

4.11.3 Fitted King Function

A functional form of an instrument's PSF (a PDF of reconstructed events' positions from a point source) can be described by an analytical function known as a "King function" (Read et al. 2011) and is given by:

$$\frac{dP}{d\Omega}(x, y, \sigma_{x,y}, \gamma) = \frac{1}{2\pi}\left(\frac{1}{\sigma_x^2 + \sigma_y^2}\right)\left(1 - \frac{1}{\gamma}\right)\left[1 + \frac{1}{2\gamma}\left(\frac{x^2}{\sigma_x^2} + \frac{y^2}{\sigma_y^2}\right)\right] \tag{9}$$

where dP is the probability to find an event in a solid angle $d\Omega$ at an offset r from the point source, σ_x and σ_y describe the size of the angular distribution in the x or y direction and γ is the weight of distribution in each tail (Ackermann et al. 2013). By assuming the PSF to be symmetrical and including an angular factor of $2\pi r$ to count the number of events per ring the King function can be reduced to:

$$\frac{dP}{dr}(r, \sigma, \gamma) = \frac{r}{\sigma^2}\left(1 - \frac{1}{\gamma}\right)\left[1 + \frac{r^2}{2\gamma\sigma^2}\right]^{-\gamma} \tag{10}$$

where r is the angular distance from the centre of the camera. Figure 31 shows an example of how well the King function fits to both the simulations and data-derived PSF using the LMFIT (Newville et al. 2014) Python package[3]. During the fitting γ, σ and a normalisation constant are all free parameters and a range of energy dependant values for each is found by fitting the King function to the simulation data at multiple energy values across the VERITAS operational energy range. These

---

[3] https://pypi.org/project/lmfit/

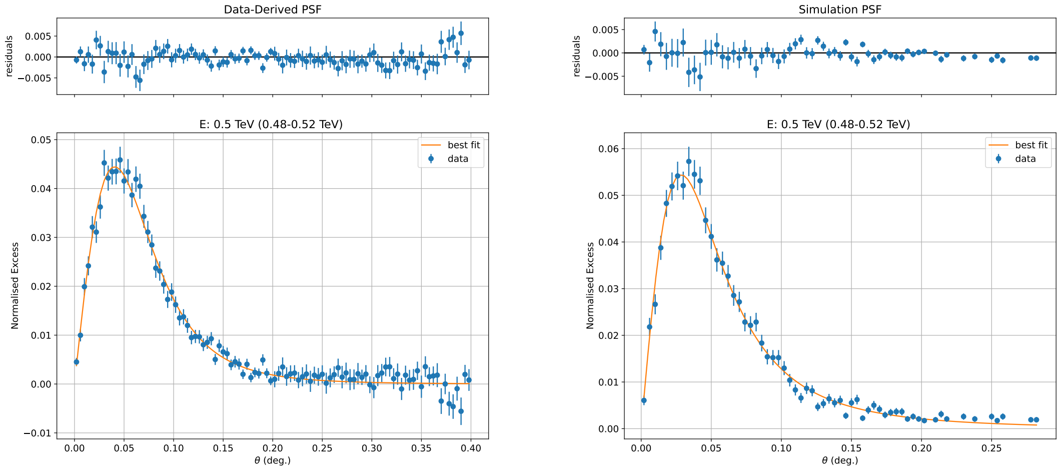

Figure 31: King function fitted to both the Crab Nebula data set (left) and VERITAS simulations (right) at 500 GeV.

are shown in Figures 32, 33 and 34. The parameters that describe the VERITAS King function PSF at any energy in the VERITAS operational range can now be obtained through interpolation. In Figure 35 the King function is shown fitted to both the data-derived PSF and simulated PSF. The simulated PSF is made up of simulations from all epochs spanning the length of all Crab Nebula PSF observations which are weighted based on exposure time per epoch. The 68% containment radius shown in Figure 36 shows the radius at which 68% of all events fall in per energy bin according to both the simulation (orange) and Crab Nebula data (blue). The standard (non ITM) VERITAS PSF has a 68% containment radius of $\sim 0.13°$ at 200 GeV and $\sim 0.07°$ at 1 TeV (Park 2016) the data-derived and simulated PSF show improvements on this at 200 GeV with values of $\sim 0.11°$ and ~ 0.07 ° respectively and the simulated PSF is consistent or slightly more contained at 1 TeV.

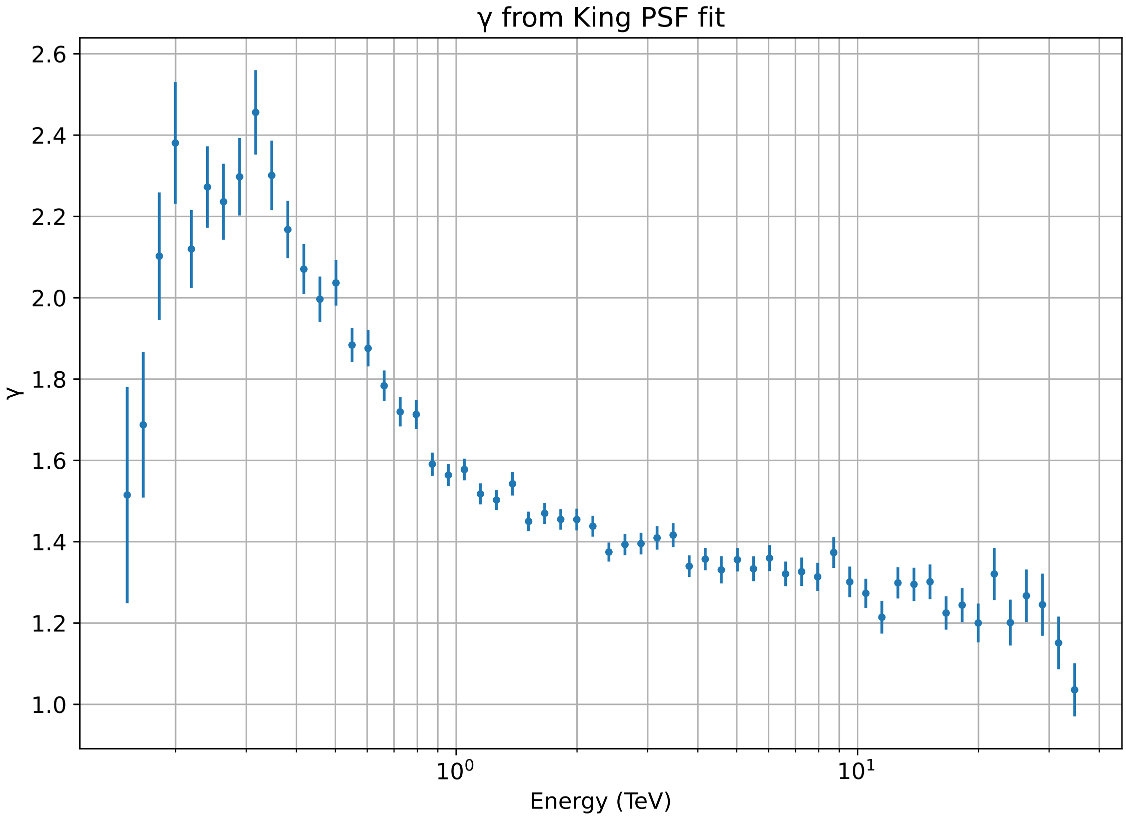

Figure 32: Distribution of the fitted King function γ parameter with respect to energy.

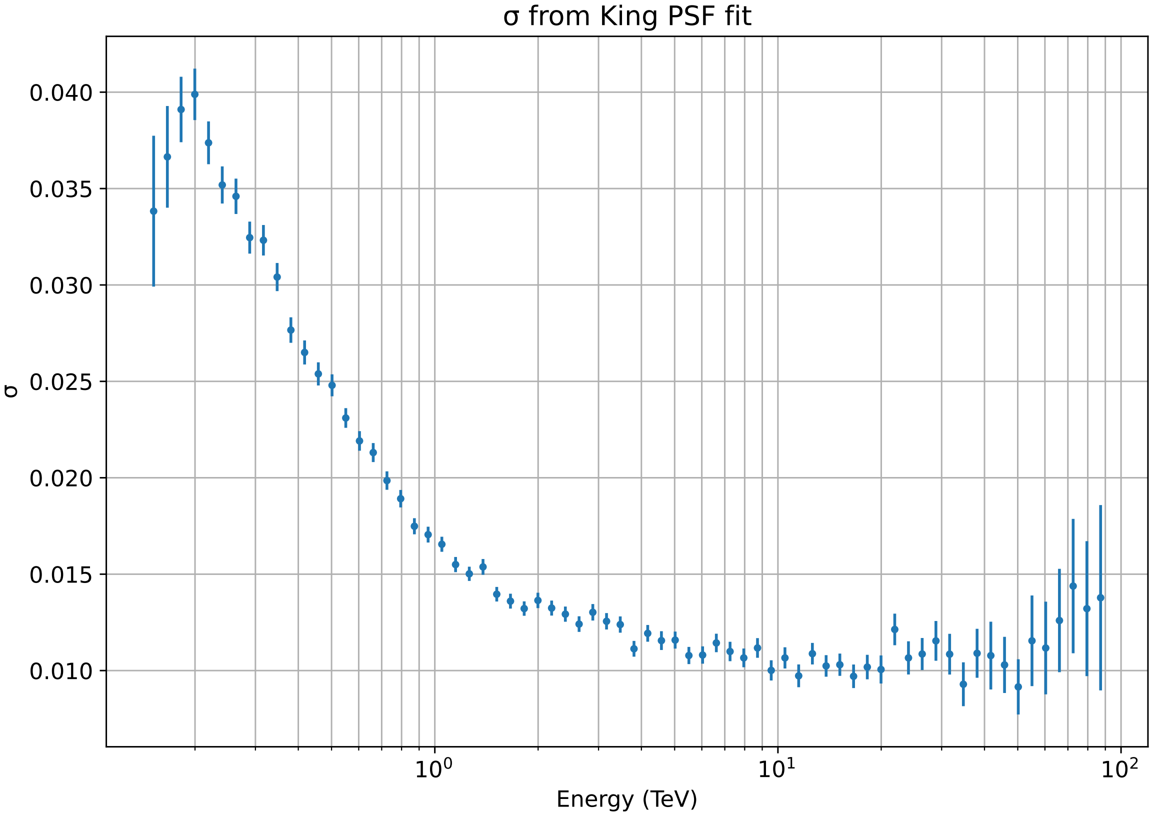

Figure 33: Distribution of the fitted King function σ parameter with respect to energy.

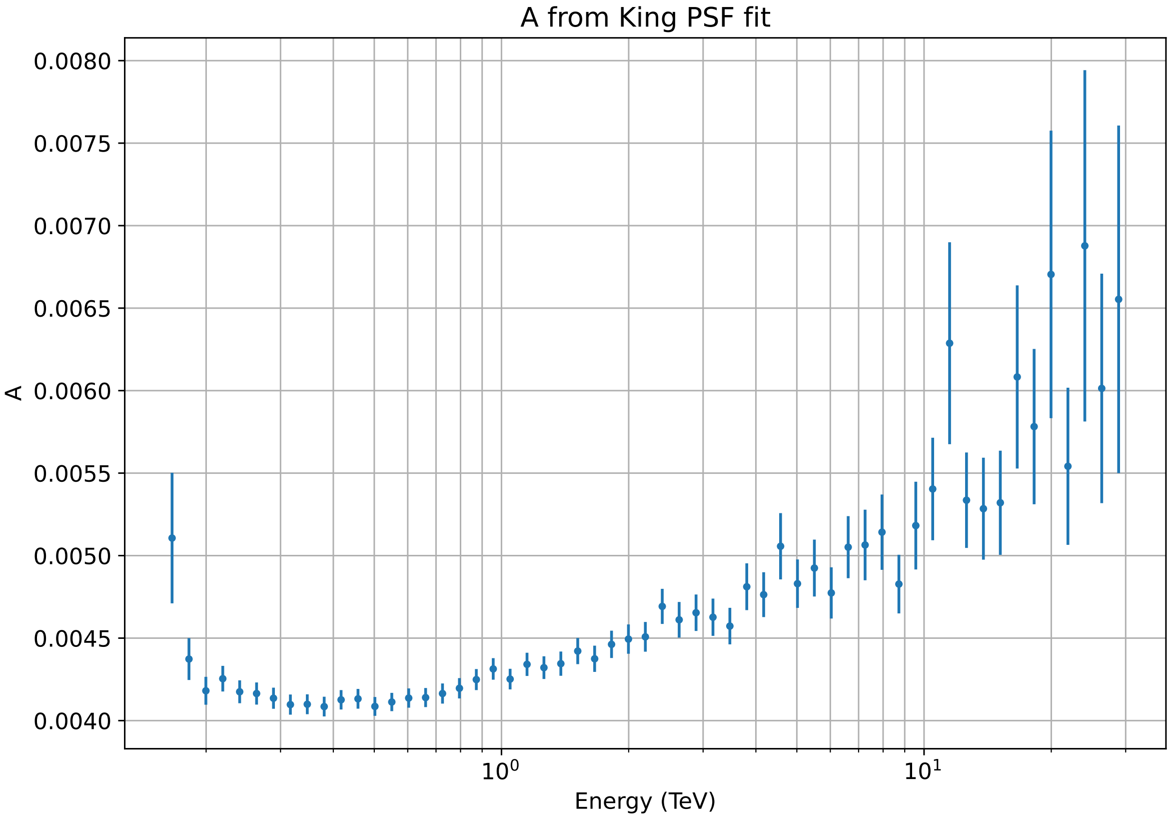

Figure 34: Distribution of the fitted King function scaling parameter (A) with respect to energy.

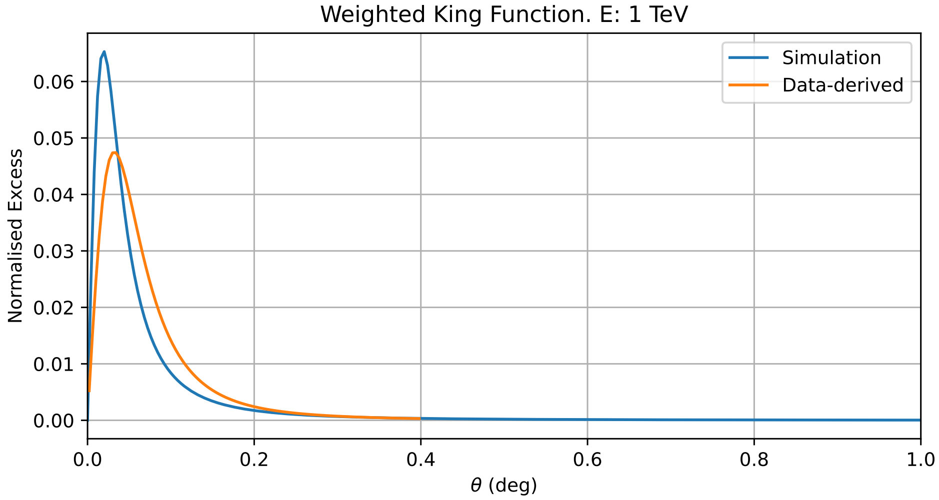

Figure 35: A comparison between the simulated PSF and data-derived PSF. The simulated PSF is made up of simulated PSF from the full range of Crab Nebula observations which are weighted based on the exposure times of those observations.

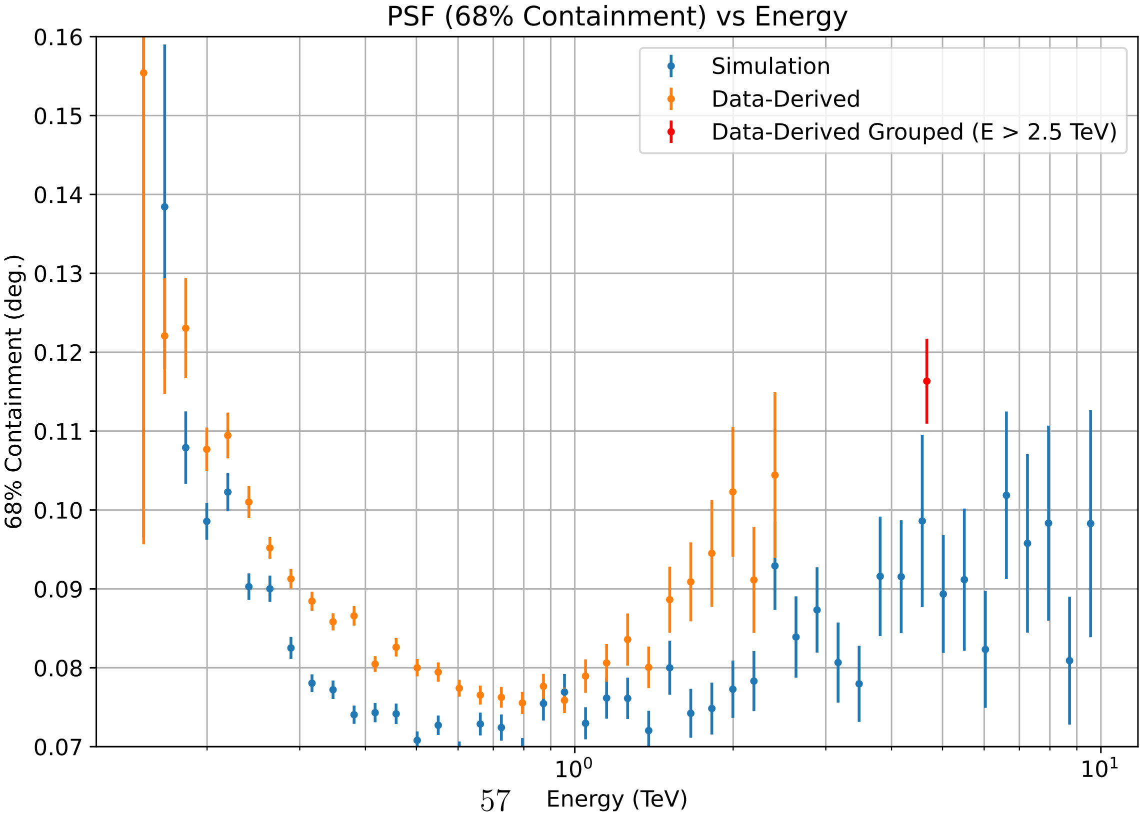

Figure 36: The 68% containment radius of the simulated (blue) and data-derived (orange) VERITAS PSF vs energy bins. Due to limited statistics above 2.5 TeV the final bin of the data-derived PSF is a grouping of all events > 2.5 TeV.

As the data-derived PSF is mostly consistent with past measurements of the VERITAS PSF (from simulations) and at some energies is better contained it is sufficiently accurate to be used in preliminary analyses. The simulated PSF improves on the data-derived PSF and is better contained all across the VERITAS energy range. Due to greater statistics, the simulated PSF also extends to a higher max energy than the data-derived PSF which gives a more complete description of the instrument. As the simulated PSF presented here is derived from ITM simulations it is either better contained or consistent with the standard PSF across the complete VERITAS energy range.

5 Dark Matter

5.1 History and Discovery

Despite being believed to make up roughly 85% of the matter in the universe, the true identity and nature of dark matter (DM) still remains unknown. DM was first discovered by Fritz Zwicky in the 1930s when observing the Coma Cluster (Zwicky 1937). Zwicky found that the mass of the cluster according to measurements of the velocity of galaxies near the edge of the cluster was different to the mass of the cluster according to its brightness. The mass of the Coma Cluster measured by Zwicky was not great enough to gravitationally bind galaxies moving with the velocity of those within the cluster. From this Zwicky assumed the presence of an unseen or "dark" matter. Further evidence to follow Zwicky's claims was later seen in 1939 when the mass-to-luminosity ratio of Andromeda was seen to increase radially. Since the initial discovery of DM there has been even more evidence found for its existence for example, gravitational lensing around galaxy clusters (Natarajan et al. 2017) and anisotropies in the cosmic microwave background (Hinshaw et al. 2009). As gravity is the only fundamental force by which DM has been seen to interact, the study of it relies heavily on theoretical predictions. Current hypotheses for the nature of DM claim weakly interacting massive particles (WIMPs) (Jungman, Kamionkowski, and Griest 1996), axion like particles (ALPs) (Essig et al. 2013), primordial black holes (PBHs) (Zel'dovich and Novikov 1967) or massive compact halo objects (MACHOs) (Griest 1993) could be the identity of DM.

5.2 Observational Evidence For Dark Matter

The existence of DM has been inferred and measured through a range of observational methods, these include

5.2.1 Velocity Dispersion

One of the first indications of the existence of DM was found by Fritz Zwicky upon applying the virial theorem to the Coma cluster (Zwicky 1937). The Coma cluster is a globular cluster containing roughly 1000 galaxies who are close to spherically symmetrically distributed. By taking the virial theorm which for a stable system of bound particles gives a relationship between the time averaged kinetic energy and the total potential energy :

$$\langle T \rangle = -\frac{1}{2} \sum_{k=1}^{N} \langle \mathbf{F}_k \cdot \mathbf{r}_k \rangle \tag{11}$$

where T is the total kinetic energy, N is the number of particles and $\mathbf{F}_k$ is the force applied to particle k and location $\mathbf{r}_k$. Zwicky measured the average mass of a galaxy as :

$$\overline{\sum_i m_i v_i^2} = \overline{\sum_i \sum_{j \neq i} \frac{G m_i m_j}{r_{ij}}} \tag{12}$$

where on the left hand side of this equation is the total mass M of the system times the mean squared velocity. On the right hand side G is the gravitational constant, r_{ij} the distance between two bodies and m_i and m_j the mass of each body. The right hand side of this equation can also be approximated as $\frac{GM^2}{R}$ where M is the total mass of the cluster and R the radius of the cluster. The mass of the cluster can then be approximated as :

$$M = \frac{Rv^2}{G} \tag{13}$$

Taking the known radius of the Coma cluster and calculating the line of sight velocities of the galaxies from their redshift Zwicky found the mass of the Coma cluster to be $\sim 7 \times 10^{13} M_\odot$ and therefore the average galactic mass to be $\sim 7 \times 10^{10} M_\odot$. Zwicky then compared these measured masses to the average galactic luminosity and found a mass-to-light ratio of $\sim 800 \Upsilon_\odot$ instead of the expected value of $2 - 10\Upsilon_\odot$ where $\Upsilon_\odot = 5133$ kg/W which is the solar mass-to-light ratio. This result implied the presence of some non-luminous matter that contributed to the mass and motion of the galaxy.

5.2.2 Rotational Curves

In 1970 a study on the radial velocity of over 65 different regions (with increasing distance from the centre of the galaxy) in the Andromeda galaxy showed a flat

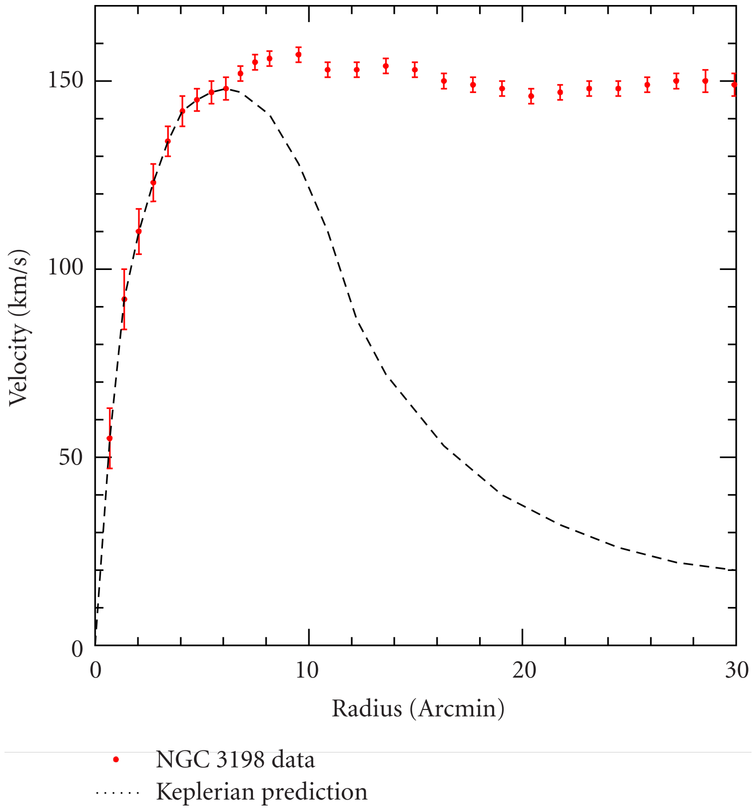

Figure 37: The measured rotational curve of NGC 3198 compared to the rotational velocities as predicted by Kepler (Russell 1964). Image : (Garrett and Dūda 2011) using data from (Begeman 1989)

rotational curve (Rubin and Ford 1970). This meant that the velocities of the regions observed were constant out to large radii instead of decreasing with distance from the centre as expected from Newtonian gravity :

$$v(r) = \sqrt{G\frac{m(r)}{r}} \tag{14}$$

where $v(r)$ is the velocity of an object at radius r, G is the gravitational constant, r is the radial distance from the galactic centre and $m(r)$ is mass contained in r. A follow-up study measuring the rotational curves of 60 galaxies all showed the same flattened rotational curve (Rubin 1983), an example of NGC 3198's flattened rotational curve is shown in Figure 37. Based on Equation 14 rotational velocities will decrease with the increase in radius as the mass contained in a given radius $m(r)$ will eventually remain constant. The results showed that rotational velocities remained constant well beyond the radius containing visible mass sources, from this it was inferred that there must be some non-visible or "dark" mass.

5.2.3 Gravitational Lensing

Einstein's works on General Relativity showed that light can bend around areas of extremely high mass in an effect known as "gravitational lensing". The amount by which the light is bent or "lensed" can be used to measure the mass of the object around which the light is being bent. Gravitational lensing is most easily seen when light from distant bright galaxies is bent around areas of high mass leading to a smeared and distorted image of the source of light. Figure 38 shows an extreme case of gravitational lensing captured by the Hubble Space Telescope where the light from a galaxy is bent in an almost complete circle around a galactic cluster. The mass of the object causing the lensing to occur can be measured with (Schneider, Ehlers, and Falco 1992) :

$$\theta_E = \sqrt{\frac{4GM}{c^2}\frac{d_{LS}}{d_L d_S}} \tag{15}$$

where θ_E is the Einstein radius (the radius of the ring of lensed light), G is the gravitational constant, M is the mass of the object causing the lensing effect, c is the speed of light and d_{LS}, d_L, d_S are the distance between the lensing object and the lensed object (the source of light), the distance to the source and the distance to the lensing object. With this equation the mass of the lensing object can be measured, this can then be compared with the mass according to the luminous matter in the object. In cases where the mass values determined from the lensing effects are not consistent with mass values inferred from luminosity, the presence of DM can be inferred. Furthermore, from measurements of lensed images, details describing the DM distributions can be determined (Amruth et al. 2023).

Figure 38: An example of gravitational lensing as captured by the Hubble Space Telescope. This image shows an Einstein Ring (a ring around a very massive object caused by gravitational lensing) around GAL-CLUS-022058s. (ESA/Hubble & NASA, S. Jha Acknowledgement: L. Shatz)

5.3 Dark Matter and Cosmology

The ΛCDM (Lambda Cold Dark Matter) model, otherwise known as the standard model of cosmology (SMC) is a simple cosmological model that provides a good description of properties of our universe. It is a favoured model as it accurately predicts the structure of the cosmic microwave background (CMB) (Penzias and Wilson 1965), the observed abundance of elements such as hydrogen and the acceleration of the expansion of our Universe (dark energy). The ΛCDM model describes a Universe made of ordinary matter, cold dark matter which is non-baryonic, cold (non-relativistic) and collisionless (interact only weakly and gravitationally), where Λ is the "cosmological constant" which describes the acceleration of the expansion of the Universe (dark or vacuum energy) (Riess et al. 1998). The model predicts that the Universe began at a single expansion event known as the "Big Bang". At the moment of the Big Bang the Universe was in a hot dense plasma state, which shortly after underwent a stage of exponential expansion. Following this the Universe remained in a hot state for several hundred thousands of years, remnants of this state are still detectable in radiation from the CMB. As the Big Bang model correctly predicts observed phenomena such as the anisotropies in the CMB, Universe expansion and distributions of lighter atoms in the Universe it is a popular model to follow. By assuming an isotropic Universe which is homogenously expanding, Friedmann developed a set of equations to describe the expansion of the Universe (Friedman 1922) :

$$\left(\frac{\dot{a}}{a}\right) + \frac{k}{a^2} = \frac{8\pi G}{3}\rho \tag{16}$$

and

$$\frac{\ddot{a}}{a} = -\frac{4\pi G}{3}\left(\rho + \frac{3p}{c^2}\right) + \frac{\Lambda c^2}{3} \tag{17}$$

where a is a relative scale factor which describes the size of the Universe with a value between 0 (Big Bang) and 1 (present), k describes the shape of the curvature of the Universe, G is the gravitational constant, $\frac{\dot{a}}{a}$ is the Hubble constant H(t) which describes how the velocity at which distant galaxies move away from the Earth is related to their distance from the Earth (Hubble 1929), Λ is the cosmological constant which describes how dark energy accelerates the expansion of the universe, p is the pressure density of the Universe and ρ is the energy density. Finally it is possible to rewrite equation 16 in terms of relic density of matter, dark energy and radiation to give :

$$\frac{H^2(z)}{H_0^2} = \Omega_r\left(1+z\right)^4 + \Omega_m\left(1+z\right)^3 + \Omega_k\left(1+z\right)^2 + \Omega_\Lambda \tag{18}$$

where z is a scaled redshift $z = \frac{1-a}{a}$, Ω_m is total matter (dark plus baryonic) in the Universe and $\Omega_k = -\frac{k}{H_0^2}$. Solving this equation with measured values such as H_0 and Ω_r (the radiation density today) allows for predictions of the current relic density of matter in the Universe which can be used to estimate the abundance of dark matter.

5.4 Dark Matter Candidates

Beyond its gravitational interactions with other matter, little is known about the nature of DM itself. In order to explain observational evidence, DM must not interact electromagnetically, must interact with normal matter only through the weak nuclear force and the gravitational force, it must be non-relativistic in order to form the clumps we see around the Universe and it must have a lifetime long enough for it to exist until present times. There is no one ideal candidate DM identity, but instead a collection of potential candidates all of which satisfy models and observations. It should be noted that there may not be one single identity for all of the DM in the Universe but instead contributions from multiple sources.

5.4.1 Weakly Interacting Massive Particles (WIMPs)

Weakly Interacting Massive Particles (WIMPs) (Kamionkowski 1998) (Griest 1993) are one of the most promising DM candidates as they fulfil the requirements set by observations and cosmological theory. In the early dense and hot Universe, DM and SM particles existed in thermal equilibrium where the DM abundance stayed consistent due to its annihilation being cancelled out by its production. As the Universe continued to expand and cool, the WIMP abundance eventually froze out of equilibrium (Cannoni 2015). The freeze out occurred at the point where the WIMP annihilation rate become less than the expansion rate of the Universe. At this point the production of DM ceased as the Universe's temperature was below the WIMP mass and annihilation of DM particles has mostly ceased due to the decreasing likelihood of DM particles interacting. The density of DM at this point is known as the relic density and matches the density of DM that exists today. From the measured relic density a value for the annihilation cross section of DM can be derived (Steigman, Dasgupta, and Beacom 2012) :

$$\langle \sigma_{ann} v \rangle \approx 3 \times 10^{-26} \mathrm{cm}^3 \mathrm{s}^{-1} \tag{19}$$

This is the cross section of a weakly interacting particle. This means that if a DM particle with a cross section smaller than this is detected the WIMP DM model is no longer a viable model. Particles which interact through the strong force or electromagnetism will produce a difference relic abundance, Figure 39 shows the expected relic abundance from strongly, electromagnetically and weakly interacting particles, as well as the equilbrium abundance. The x-axis is a proxy for time and the y-axis is the particle abundance. This is another strong motivation for a WIMP DM and is known as the ”WIMP miracle”. There are other theorised production mechanisms for WIMP DM for example, the ”freeze in” mechanism which will produce a category of WIMPs known as feebly interacting massive particles (FIMPs) (Hall et al. 2010). The freeze-in mechanism assumes the Universe began with no DM which is generated over time though the decay of heavier particles. Unfortunately a particle like this will be harder to detect as they interact with SM particles extremely weakly. On the other hand, in some models FIMPs are not absolutely stable and could decay at some age greater than that of the Universe. If this is the case, FIMPs could yet be detected via indirect methods (5.5.3).

5.4.2 Non-WIMPs

Axions were first postulated in 1977 as a solution for the strong CP problem in Quantum Chromodynamics (QCD) (Peccei and Quinn 1977) but have since become DM candidates. Axions are believed to have a low mass $m_a < 0.01$ eV (Murayama et al. 1998) and couple weakly to other matter (Abbott and Sikivie 1983). It is believed that axions were never in thermal equilibrium making them a candidate for cold DM. If axions have a mass in the range of $10^{-5} - 10^{-2}$ eV they avoid the issue of overclosing the Universe (preventing the Universe from reaching its current age) as well as accounting for current observational constraints (Bergström 2009). Despite these positives, the axion production mechanism is still unclear which leads to uncertainties on their relic density (Marsh 2016).

Primordial Black Holes (PBHs) are theoretical black holes whose existence was first suggested in 1966 (Zel’dovich and Novikov 1967). They were theorised to have formed in the early Universe when dense pockets of matter would collapse under their gravitational force and form a black hole. Depending on which model is followed and its formation time a PBHs could have an initial mass of 10^{-8} kg $< m_{PBH} < 10^3$ $M_\odot$. As black holes have been shown to radiate and emit particles due to quantum gravitational effects (Hawking 1974) a PBH with an initial mass of $m_{PBH} < 10^{12}$ kg would have already evaporated (Villanueva-Domingo, Mena, and Palomares-Ruiz 2021) and therefore would not contribute to the amount of DM in the current universe. PBHs are a favourable DM candidates as they are non-

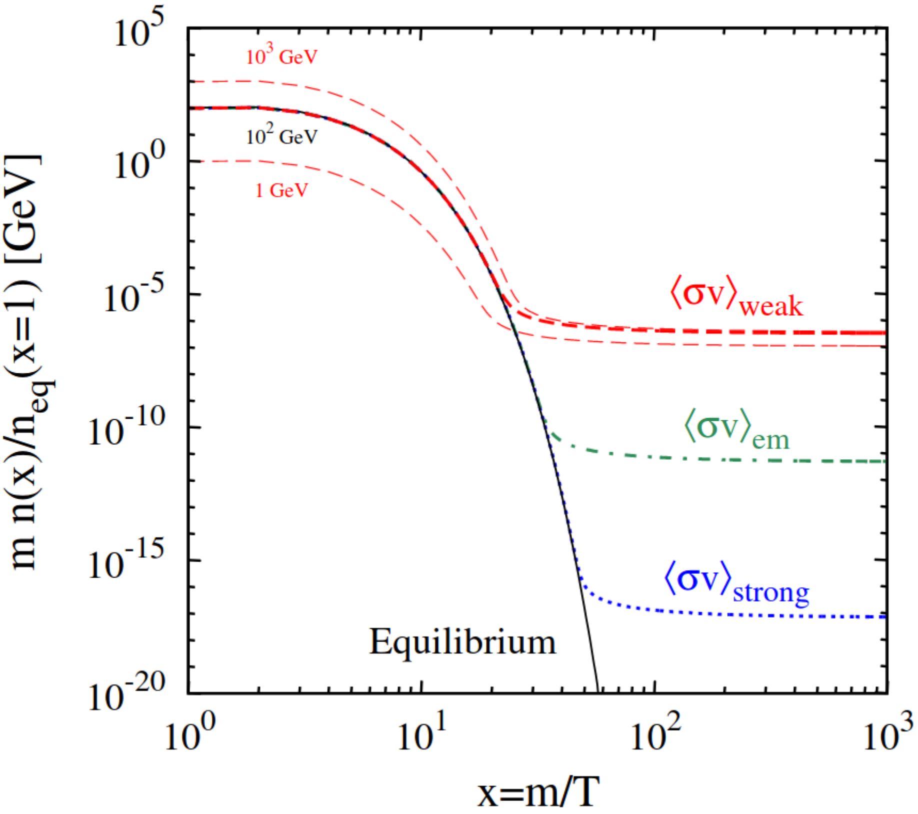

Figure 39: The evolution of WIMP abundance over time. The black curve shows the particle abundance if thermal equilibrium is maintained, the dashed red line shows the abundance of a particle that interacts via the weak nuclear force, the dashed green shows the abundance if DM interacts electromagnetically and the blue dashed line shows the abundance for a particle which interacts by the strong nuclear force. (Steigman, Dasgupta, and Beacom 2012)

baryonic and interact gravitationally although it has been shown that PBHs cannot make up 100% of the DM mass in the Milky Way (MW) and therefore cannot be the lone identity of DM (Bennett et al. 1996a).

Massive Astrophysical Compact Halo Objects (MACHOs) are massive, non-luminous astrophysical objects which emit little to no radiation and have no associated planetary systems. MACHOs are detected through gravitational lensing which occurs when a MACHO passes in front of a source of light. MACHOs are believed to consist of familiar objects such as brown dwarfs, white dwarfs or black hole remnants (Bennett et al. 1996b). This makes MACHOs an appealing identity for DM as no new particles are required to satisfy this theory. Despite the appeal of a MACHO DM, searches for MACHOs in the Large Magellanic Clouds rule out the possibility of them being the sole contributor to the DM content of its halo (Tisserand et al. 2007) as the observed microlensing rate toward the Large Magellanic Clouds is lower than that of a halo which is dominated by MACHOS. This shows there must be a further source of DM.

As the only evidence for DM is through gravitational interactions, it is also possible to explain the evidence with a modified law of gravity. For example, galaxy rotation curves can be explained by modified Newtonian dynamics (MOND) (Milgrom 1983). Unfortunately there is yet to exist a modified law of gravity that can explain all evidence of DM.

5.5 Detecting Dark Matter

DM does not interact electromagnetically, this means it does not emit, absorb or reflect light and therefore is difficult to detect. A range of methods to detect DM that do not rely on DM interacting electromagnetically are now used to study DM. Collider experiments attempt to produce DM through collisions between Standard Model particles in large underground particle accelerators. Direct detection experiments rely on the ambient DM in the Universe colliding with targets made of ordinary matter housed in underground detectors. Finally, indirect detection experiments look to areas of the Universe with large DM content and attempt to observe the products of DM annihilation or decay. Figure 40 shows the beginning and end

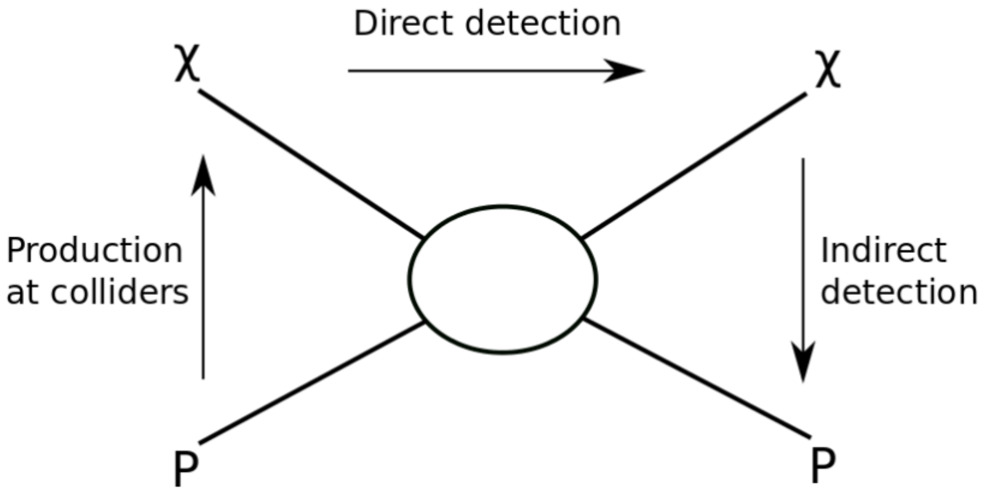

Figure 40: A cartoon visualising the the channels through which each detection method works. In this case χ is the DM particle and P is a SM particle (Marrodán Undagoitia and Rauch 2016)

product of each detection method, i.e. indirect methods look for SM particles produced by DM, direct detection methods looks for signs that DM has rebounded or scattered off of SM particles and collider experiments look for DM produced by SM particles.

5.5.1 Direct Detection

The goal of direct detection experiments is to observe signatures of DM particles scattering off of nuclei in the detector's target (Goodman and Witten 1985). The methods used in direct detection experiments can vary depending on what DM particle is being searched for. For example in searches for WIMP DM, liquid xenon is often used as the medium through which DM is detected. The XENON (Aprile et al. 2011), (Aprile et al. 2016), (Aprile et al. 2020) experiments are a series of experiments in which a large tank of liquid xenon is used as a scintillator, these tanks contain a detector consisting of an array of PMTs. When an incident DM particle collides with the liquid xenon it will release a photon which is seen by the PMTs.

During the interaction with the xenon, electrons are also produced which through the use of an electric field (which also prevents the recombination of the electrons) will drift to the top of the tank and are detected by a second detector. This gives two observations of the same event and allows for a 3D model of the event which can be used for background discrimination. Other direct DM searches use similar concepts i.e. using a chosen medium to convert DM into a detectable form, but may vary the medium used or final state detected. In the case of searches for axions such as the Axion Dark Matter Experiment (ADMX) (Du et al. 2018), magnetic fields are used to convert DM to microwave photons which are then detected. Direct DM searches can look for a range of DM interactions but there has been no successful detection of any DM/SM interaction, results for the spin-independent elastic WIMP-nucleus scattering are shown in Figure 41. In a mass range greater than 3 GeVc^{-2} experiments such as XENONIT (Aprile et al. 2016) and LUX (McKinsey et al. 2010) have achieved the strongest constraints and below that energy range where these experiments do not operate the most constraining limits are placed by DarkSide-50 (Agnes et al. 2018).

5.5.2 Collider Experiments

The goal of DM searches at large underground particle accelerators such as the Large Hadron Collider (LHC) is to accelerate standard model particles up to great energies and collide them with other nuclei, in turn producing DM particles. The DM particles produced in these collisions will not be directly detectable due to their weak interactions with the SM particles that make up the detectors. In order to detect the DM particles instead their existence can be inferred through the conservation of momentum of the collision in what is known as ”missing momentum” signatures. As the net momentum after the collision must be zero, cases where the net momentum of all detected particles does not equal zero will indicate the presence of DM. This method still brings with it some difficulties, for example, SM neutrinos which are produced in the decay of some bosons will lead to similar missing momentum signatures and thus act as a large background that must be modeled before removal. As well as this the production of a new particle which shows similar characteristics to a proposed DM particle does not immediately solve the DM problem, in order to

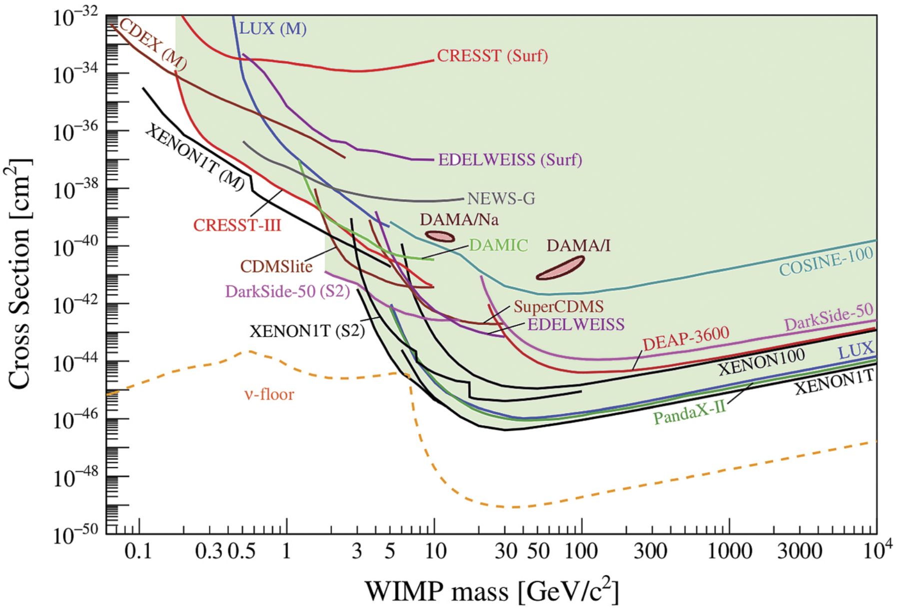

Figure 41: A summary of results from a range of direct detection searches for WIMP-nucleus elastic scattering (Billard et al. 2022). Here the ν - floor is the cross section at which an experiment with a Ge target has a 90% probability to detect a WIMP with a statistical significance of 3σ or more.

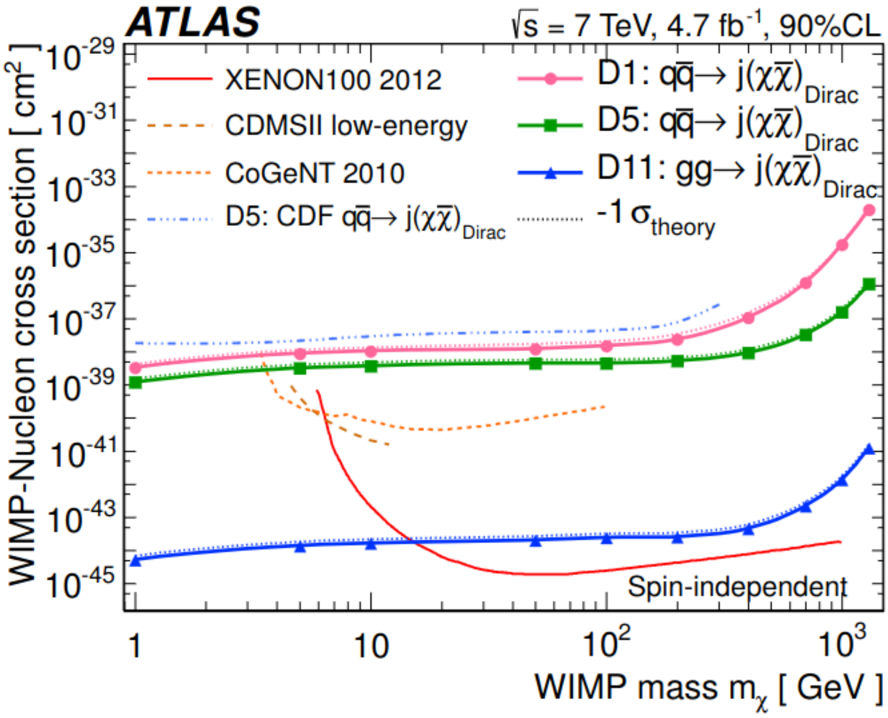

Figure 42: Upper limits placed on the spin-independent WIMP-nucleon scattering cross-section vs WIMP mass m_χ by the ATLAS experiment at the LHC (Aad et al. 2013). The thick solid lines are observed limits with theoretical uncertainties excluded and the thin dotted line is derived from theory. Results are shown alongside results from direct detection experiments XENON100 (Aprile et al. 2012), CDMSII (Ahmed et al. 2011), CoGeNT (Aalseth et al. 2011), CDF (Aaltonen et al. 2012), and CMS (Chatrchyan et al. 2012)

confirm that the produced particle is the same DM that is observed in the rest of the Universe, it also needs to be stable on cosmological timescales and capable of reproducing the DM abundance seen today. Limits placed on the spin-independent WIMP-nucleon scattering cross-section by ATLAS are shown in Figure 42 alongside corresponding results from direct detection experiments.

5.5.3 Indirect Detection

Indirect detection methods do not look directly for DM or DM interactions, but instead these methods look for signatures of DM decay or annihilation into SM gamma rays. DM particles may decay or annihilate into SM particles. Secondary gamma rays produced in the annihilation or decay could be observed with ground-based or space-based telescopes. The presence of DM can be determined from the spectra of the observed photons. As photons are unperturbed as they travel from their source through space, indirect DM searches can focus on areas with high DM content. Indirect searches are unfortunately affected by astrophysical background so targets with high DM annihilation/decay rates and little to no other means of gamma-ray production are preferred targets for an indirect search.

5.6 Targets for Indirect Dark Matter Detection

There are multiple factors that determine the favourability of a source for indirect DM detection. First and foremost is the DM density of the source itself. A greater density of DM in a target will lead to a greater rate of DM decay or annihilation. This does not mean though that the source with the largest DM density is the best target for an indirect DM search. Targets that are harder to observe due to having a larger gamma-ray background or other complicated observing conditions may be less favourable. Some of the targets that will be discussed are shown in Figure 43 along with a visualisation of some of the pros and cons of each target.

5.6.1 Milky Way

The Galactic Centre (GC), located at the centre of the Milky Way is one of the closest ($\sim$8 kpc from Earth) targets for an indirect DM search. Simulations predict a very large DM density (Navarro et al. 2010) in the GC, especially when compared to other candidate targets. Unfortunately there are many VHE gamma-ray sources in the vicinity of the GC which contribute to a complicated background that must be handled when performing the DM search.

A DM halo around the Milky Way is another potential target. Unlike the GC a halo surrounding the galaxy does not contain many sources of astrophysical gamma-

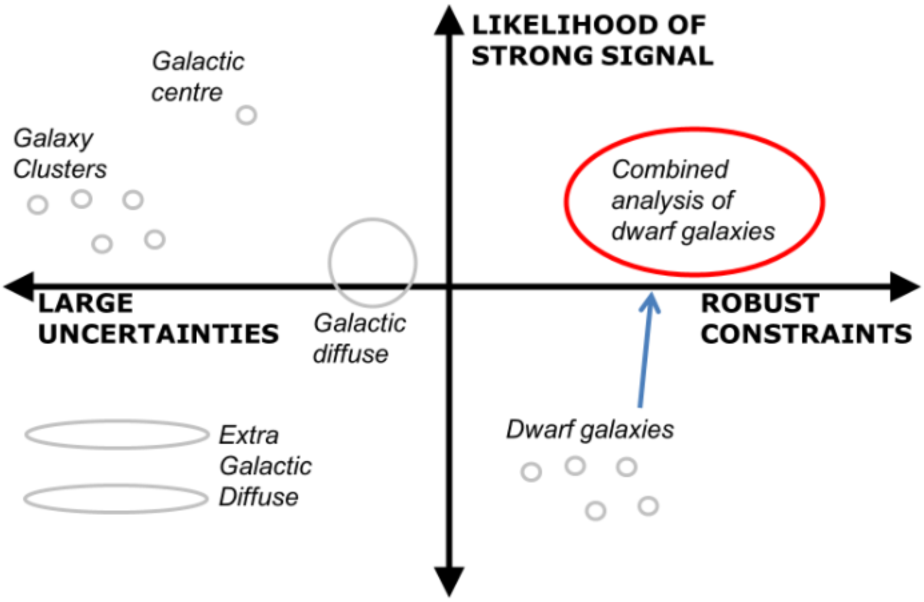

Figure 43: A visualisation of different targets for an indirect DM search showing their pros and cons. Circled is the combined analysis of dSphs which is the focus of this research. (Conrad 2014)

rays and as a result does not suffer from a complicated background, thus making it an easier target to analyse. Unfortunately most DM halo models suggest there is a lower rate of DM annihilation than in the GC.

5.6.2 Neutrinos

Another potential product of DM annihilation is high-energy neutrinos which could be observed by neutrino observatories such as IceCube (Aartsen et al. 2017). DM neutrino searches can be performed on a range of targets such as the Sun, Earth, galaxy clusters and dwarf spheroidal galaxies (dSph). It is expected that WIMPs already present in our solar system will become gravitationally trapped in the Sun and Earth after losing a significant amount of energy through scattering off of nucleons. In dSphs the WIMPs are expected to have been accumulated through gravitational attraction during the formation of the galaxies. Of these targets, the Sun is one of the most promising for a DM search with a neutrino telescope. As the Sun accumulates more DM particles the rate of DM annihilation will grow until it reaches a peak annihilation rate. This peak occurs once equilibrium between capture and annihilation is achieved, a point which is assumed to already been reached (Ibarra, Totzauer, and Wild 2014).

5.7 Dwarf Spheroidal Galaxies

Dwarf spheroidal galaxies are small, DM dominated (Mateo 1998) galaxies in the local group. DSphs are located between 25 kpc and 250 kpc from Earth. They have a low gamma-ray flux due to their low rates of star formation and gas densities leading to a large mass-to-light ratio (greater than $10^{1-3}[M/L_v]_\odot$) (Strigari et al. 2008) and a low baryonic content. The DM density in a dSph can be estimated by the dynamics of the stars within the galaxy (Wolf et al. 2010) , (Walker et al. 2009) , (Martinez et al. 2009) and thus making the results from an indirect DM search in a dSph more robust albeit less constraining than a more DM dense target.

5.8 Results from Gamma-Ray Telescopes

As understanding the nature and identity of DM remains one of the most popular areas of research in modern physics indirect searches for DM have been performed by a range of leading gamma-ray telescopes. These searches are not limited to any one category of targets nor to one specific target within a category. For this reason to present results from all categories of targets used in indirect searches for DM with gamma-ray telescopes would be too broad, instead results from searches in the GC and dSphs with Fermi-LAT, HAWC, H.E.S.S., MAGIC and VERITAS are shown. The Fermi-LAT search uses the largest dataset of any gamma-ray telescope with results from ∼11 years worth of observations of 27 different dSphs (Hoof, Geringer-Sameth, and Trotta 2020). The HAWC collaboration present limits in a search using 507 days for data gathered on 15 dSphs in a DM mass range that extends an order of magnitude greater than Fermi-LAT (Albert et al. 2018). Results from H.E.S.S. show limits which are competitive with past VERITAS studies from 130 hours of observations of 5 different dSphs (Abdalla et al. 2018) and finally results from the MAGIC collaboration show the most constraining limits above a DM mass of ~ 1 TeV (below which Fermi-LAT are most constraining) with 345 hours observations of 4 dSphs (Acciari et al. 2022). Also shown are limits from indirect DM searches in the Galactic Centre with H.E.S.S. (546 hours) (Abdalla et al. 2022) and VERITAS (154 hours) (Ryan 2023) which are the most contstraining of limits due to the large DM content of the GC.

As the VERITAS data set has grown by a factor of ~ 3 since results shown in Figure 44 new analyses including the full data set will further constrain these limits. This search will include the use of improved VERITAS analysis methods and the most up-to-date models of dSphs. The search can also be extended to place limits on the annihilation cross-section of DM in the ultra-heavy mass range. Finally as the DM halos of dSphs are largely extended, the use of an extended-source analysis can be used to obtain larger DM densities in each dSph which will lead to further constraints on the annihilation cross section upper-limits.

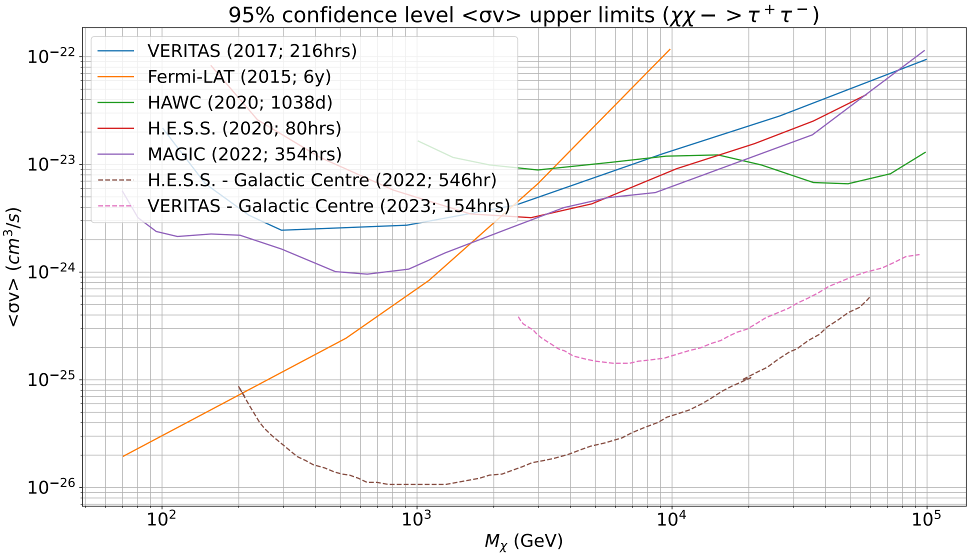

Figure 44: The up-to-date published results for indirect WIMP DM searches by Fermi-LAT, MAGIC, VERITAS, HAWC and H.E.S.S. for the $\tau^+\tau^-$ channel.

6 Indirect Dark Matter Search

As previously discussed, dSphs are ideal targets for an indirect DM search, due to their high mass-to-light ratio and low astrophysical background. Despite no statistically significant detection of a gamma-ray excess from any dSph to date, DM searches can help constrain the thermally averaged annihilation cross-section of WIMP DM. In order to constrain the annihilation cross-section the predicted gamma-ray spectrum is folded through the IRFs and exposures for the VERITAS data sets to generate predicted signal and background counts. A maximum-likelihood analysis is then used to derive the most probable values for thermally-averaged cross sections that cause the predicted and measured counts to agree or to derive upper limits when there are no statistically significance excess counts. This is then applied to all of the VERITAS data on dSphs and all annihilation channels.

Dwarf	Point-Source Exposure (Hours)	Extended-Source Exposure (Hours)
Böotes	13.98	0
Coma Berenices	39.76	22.6
CVn I	9.72	8.46
CVn II	8.14	5.43
Draco II	8.02	3.56
Hercules I	9.46	9.02
Leo I	5.66	5.0
Leo II	11.31	11.31
Leo IV	0.48	0.48
Leo V	1.38	0.47
Segue 1	126.29	51.82
Segue 2	12.51	11.88
Sextans I	7.45	7.45
Triangulum II	29.51	27.47
Ursa Major I	6.63	6.34
Ursa Major II	212.32	175.20
Ursa Minor	135.3	110.16
Total	637.92	456.65

Table 2: Exposure time in hours of the good quality data for each dSph used in the point-source (column 2) and the extended-source (column 3) analysis.

6.1 Target Selection and Dataset

Between the years of 2007 and 2018 VERITAS has amassed a total of 958 hours (638 after data quality checks) of observations combined across 17 dSphs. These data have been collected across two observation schemes: a short exposures survey of less DM-dense galaxies and deep exposures of selected galaxies with greater predicted DM densities. Three dSphs (Segue 1, Ursa Minor, and Ursa Major II) were the focus of deep exposures with more than 100 hours obtained on each target. The remaining 14 dSphs were subjects of the short survey observations. A breakdown of the exposure time per dSph is shown in column 2 of Table 2. The reason for the difference in exposures is discussed in section 6.1.1.

6.1.1 VERITAS Extended Analysis

The integral J-Factor (DM luminosity at a point on the sky, see Section 6.4) of a dSph can be extended well beyond the standard VERITAS point-source cut (Further discussed in Section 6.4). As a result a significant amount of a galaxy's DM density is omitted when performing a point-source analysis. By increasing the VERITAS angular cut the DM density of each dSph will be increased and results obtained will now better represent the true DM density of the dSph. An angular extension of 0.2° was chosen for this analysis in order to greatly increase the amount of DM contained, while also ensuring no impact from the camera gradient on *ON* and *OFF* count rates (see Section 4.8 for further details). As increasing the angular extension increases the size of the *ON* and *OFF* regions, some data becomes unusable as there is a reduced area for *ON* and *OFF* regions and in some cases overlap with exclusion regions leads runs with no *OFF* regions. A visual representation of the *ON* and *OFF* regions of both a point-source and extended-source analysis are shown in figures 45 and 46 respectively and shows how the number of *OFF* regions will decrease with an increase of the angular cut. Any data taken prior to V6 is also unusable in the extended-source analysis as no extended-source ITM IRFs are currently available. Apart from increasing the angular extension the analysis of each dSph remains the same as the point-source analysis. Table 2 shows the exposures of each dSph used in the extended-source analysis.

6.2 Dark Matter Gamma-Ray Spectrum

A prediction of the gamma-ray spectrum produced when DM particles decay or annihilate is required for an indirect DM search. DM particles can decay or annihilate through a range of different channels with the primary SM particles produced being leptons, quarks or bosons where secondary gamma rays are produced through a cascade of decays by the primary products. It is also possible for DM to annihilate directly to gamma rays. Depending on the channel through which DM decays/annihilates the gamma rays produced may be seen as a continuum, or a line emission. Figure 47 shows an example of the gamma-ray spectrum produced by multiple different channels, each of which is considered in an indirect DM search as

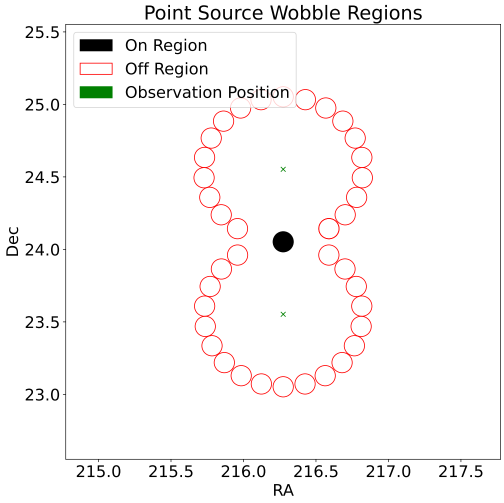

Figure 45: A visualisation of the *ON* (black circles) and *OFF* (red circles) regions of a point-source analysis. The regions produced from both North and South wobble observations are shown with the green cross designating the centre of the camera's FoV for each.

no channel is preferred to another.

When searching in the standard WIMP DM mass range (≤100 TeV) DM annihilation spectra are provided using the *Poor Particle Physicist's Cookbook For Dark Matter (PPPC4DM)* (Cirelli et al. 2011). Through the use of the *PYTHIA* (Sjöstrand, Mrenna, and Skands 2008) and *HERWIG* (Corcella et al. 2001) simulators and the inclusion of electroweak corrections (Ciafaloni et al. 2011), *PPPC4DM* provides the energy spectra of gamma rays at production for each DM channel. From these spectra a value for $\frac{dN}{dE'}$ (the energy spectrum of a single annihilation in the case of a 100% branching ratio into its final state) can be obtained. The nine annihilation channels investigated in this analysis are : $W^+W^-, \tau^+\tau^-, b\bar{b}, t\bar{t}, \gamma\gamma, e^+e^-, \mu^+\mu^-, \nu\overline{\nu}_e, ZZ$.

6.2.1 DM Annihilation Spectrum Beyond Unitarity Limit

Due to the unitarity limit on annihilation into SM particles, point-like DM particles are restricted to masses $<$ 100 TeV (Griest and Seckel 1991). This limit can be bypassed in cases of composite DM particles (Harigaya et al. 2016) or if DM was

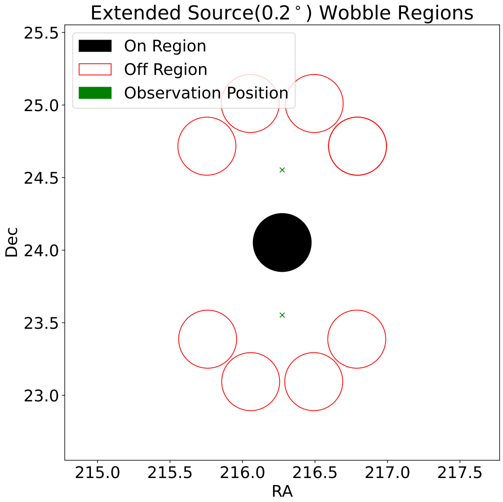

Figure 46: A visualisation of the *ON* (black circles) and *OFF* (red circles) regions of an extended-source analysis with an angular cut of 0.2°. The regions produced from both North and South wobble observations are shown with the green cross designating the centre of the camera's FoV for each.

to decay into a meta-stable dark state before decaying into SM particles (Berlin, Hooper, and Krnjaic 2016). If this is the case ultra-heavy dark matter (UHDM) could produce gamma rays with energies on the order of 10s of TeV (Tak et al. 2022), allowing for an indirect search for UHDM with masses up to 10s of PeV. UHDM annihilation spectra are provided by *HDMSpectrum* (Bauer, Rodd, and Webber 2021). In this analysis, the *HDMSpectrum* is used only for DM masses $>$ 100 TeV. Figure 48 shows a comparison between the $\tau^+\tau^-$ annihilation spectra according to *PPPC4* and *HDM*. Despite the spectra from both PPPC4 and HDM being largely consistent in their overlapping mass range, PPPC4 is chosen for the lower masses because even though HDM covers a mass range down to low TeV it is not recommended below $\sim$ 100 TeV. For this reason, HDM is only adopted in the mass range that is not covered by PPPC4.

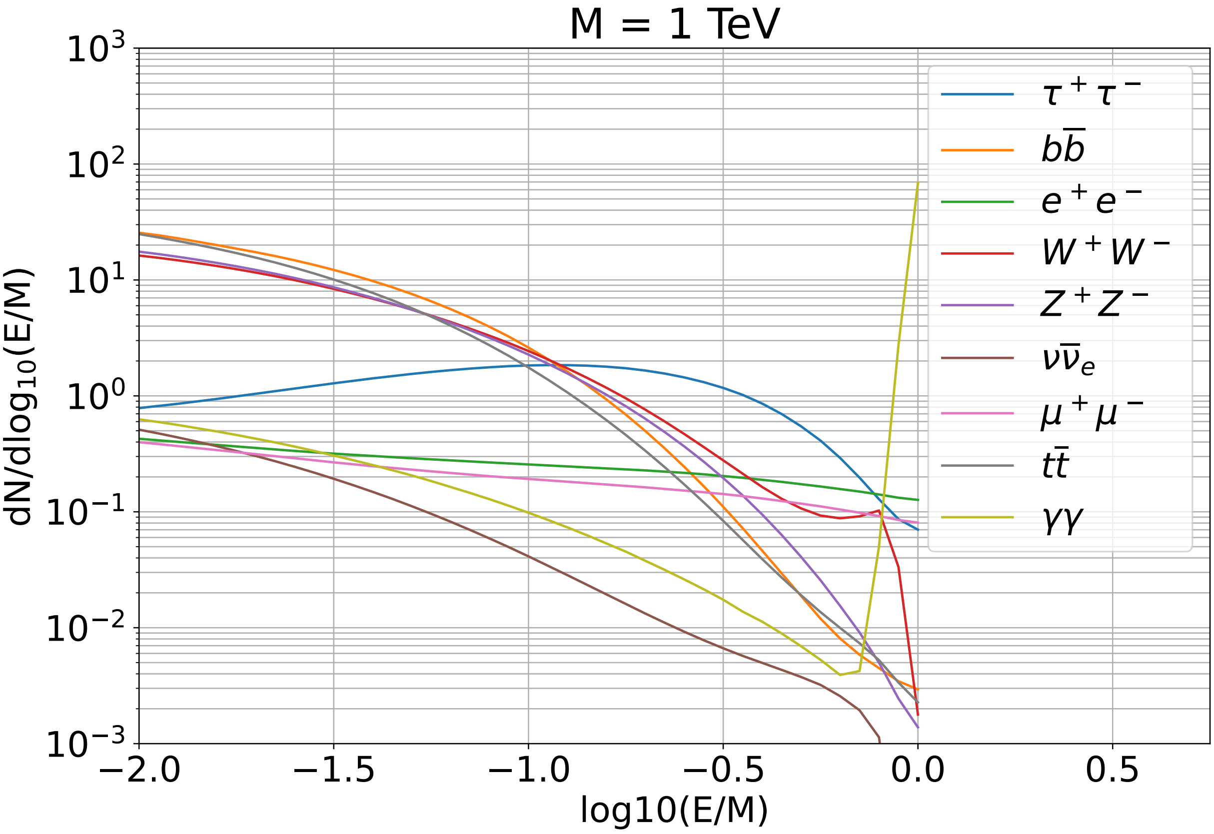

Figure 47: Gamma-ray flux from annihilation at $M_{DM} = 1$ TeV. Each curve represents a different channel through which gamma rays are produced.

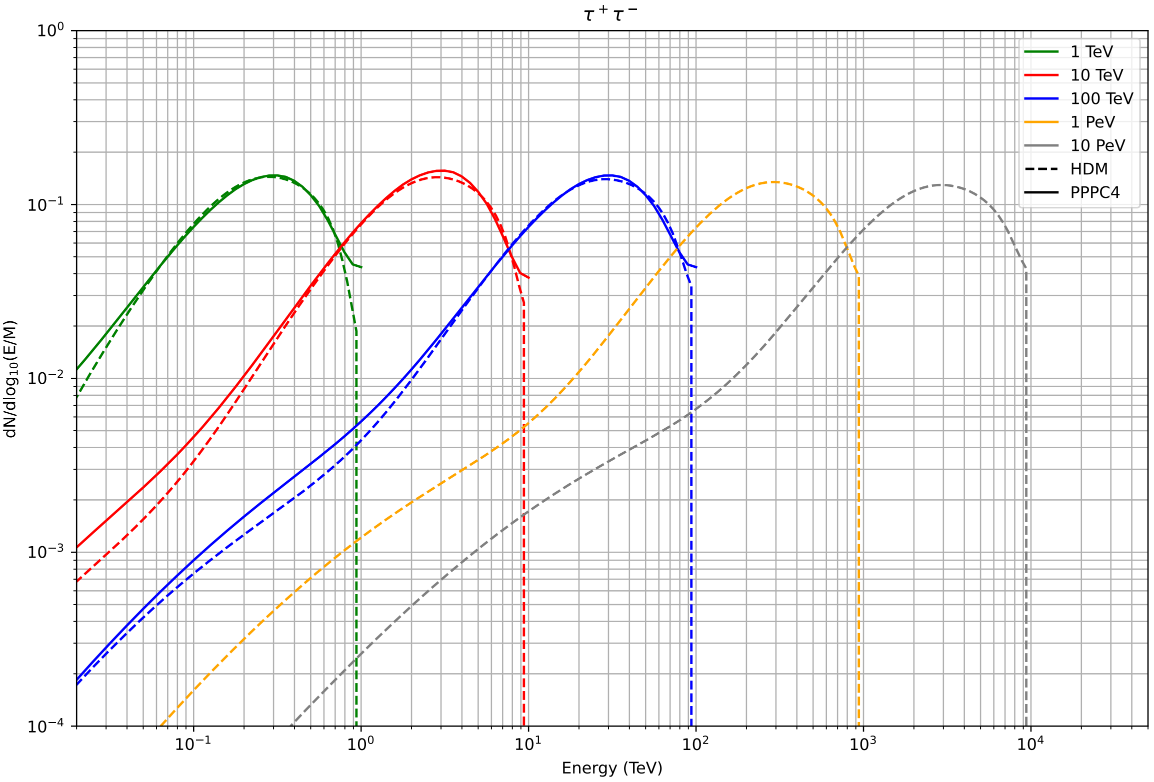

Figure 48: The $\chi\chi \rightarrow \tau^+\tau^-$ annihilation spectra at DM masses of 1 TeV, 100 TeV and 1000 TeV produced with *PPPC4* and *HDM*

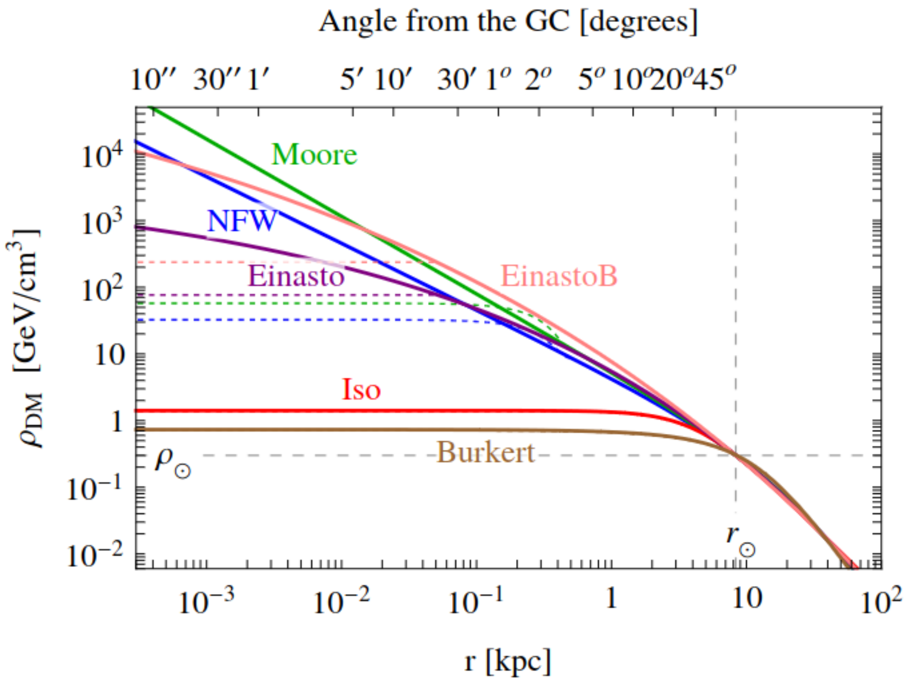

Figure 49: A range of density profiles describing the DM density at the galactic centre (Cirelli et al. 2011).

6.3 Dark Matter Density Profiles

A range of different empirical models describing the DM density profile in a dSph are used in published analyses. These models generally assume the dSph to be spherically symmetric and are motivated by observed parameters such as rotational curves and line-of-sight velocities of stars within the galaxy. Figure 49 shows how various different candidate DM density profiles may describe the DM density in the galactic centre. Some of the popular models used in current research are as follows (in all cases r_s is a scale radius and ρ_s is a scale density) :

6.3.1 The Moore Profile

The Moore profile (Diemand, Moore, and Stadel 2004) is a three parameter function which is derived by simulating cluster halos from which a density profile can be measured. The simulations are verified against the Virgo cluster. The Moore profile is defined as :

$$\rho(r) = \rho_s \left(\frac{r_s}{r}\right)^{1.16} \left(1 + \frac{r}{r_s}\right)^{-1.84} \tag{20}$$

6.3.2 The Einasto Profile

The Einsato profile (Merritt et al. 2006), unlike other models uses a shaping parameter α which when decreased corresponds to a steeper density profile, is defined as :

$$\rho(r) = \rho_s e^{-\frac{2}{\alpha}\left[\left(\frac{r}{r_s}\right)^{\alpha} - 1\right]} \tag{21}$$

6.3.3 The Isothermal Profile

The Isothermal profile (Begeman, Broeils, and Sanders 1991) is more heavily motivated by measurements of galaxy rotation curves than by simulations and is defined as :

$$\rho(r) = \frac{\rho_s}{1 + \left(\frac{r}{r_s}\right)^2} \tag{22}$$

6.3.4 The Burkert Profile

The Burkert profile (Burkert 1995) which like the Isothermal profile is also more motivated by galactic rotational curves is :

$$\rho(r) = \frac{\rho_s}{\left(1 + \frac{r}{r_s}\right)\left(1 + \left(\frac{r}{r_s}\right)^2\right)} \tag{23}$$

6.3.5 The Navarro-Frenk-White Profile

The Navarro-Frenk-White (NFW) profile (Navarro, Frenk, and White 1996) is one of the more commonly used DM density profile models. It is based on N-body simulations and covers a range of masses from dwarf galaxies to galaxy clusters. The NFW density profile is defined as :

$$\rho(r) = \rho_s \frac{r_s}{r}\left(1 + \frac{r}{r_s}\right)^{-2} \tag{24}$$

In this analysis the spherically symmetric NFW DM density profile is used :

$$\rho(r) = \frac{\rho_s}{(r/r_s)(1 + (r/r_s))^2}, \quad \text{if } r < r_t, \text{ otherwise } \rho = 0, \tag{25}$$

the NFW parameters used are obtained from probability density functions presented in (Ando et al. 2020). As these are some of the most up-to-date realisations of DM profiles they were chosen for use in this analysis. In the case of ultra-faint dSphs physically motivated priors based on the circular velocity of a satellite in the host's sub halo are used to produce physically constrained parameters. In the case of classical dSphs (Leo I, Leo II, Sextans and Ursa Minor) previously known parameters are scaled based on dynamical mass (Pace and Strigari 2019). These values are calculated using a Python package[4] provided by the authors which produces the probability density functions (PDFs) for the NFW parameters.

6.4 J-Factors

As most dSphs have extended DM halos the DM distribution throughout a dSph is best described by a differential profile with respect to solid angle. The differential J-Profile is found by integrating the DM density profile (Section 6.3) squared of a dSph along the line-of-sight:

$$\frac{dJ}{d\Omega} = \int_{los} \rho^2 (l, \Omega)\, dl \tag{26}$$

As the DM density profile of a dSph is spherically symmetric an angular J-Profile can be written as:

$$\frac{dJ}{d\theta} = 2\pi \sin\theta \frac{dJ}{d\Omega} \tag{27}$$

---

[4] https://github.com/shinichiroando/dwarf_params

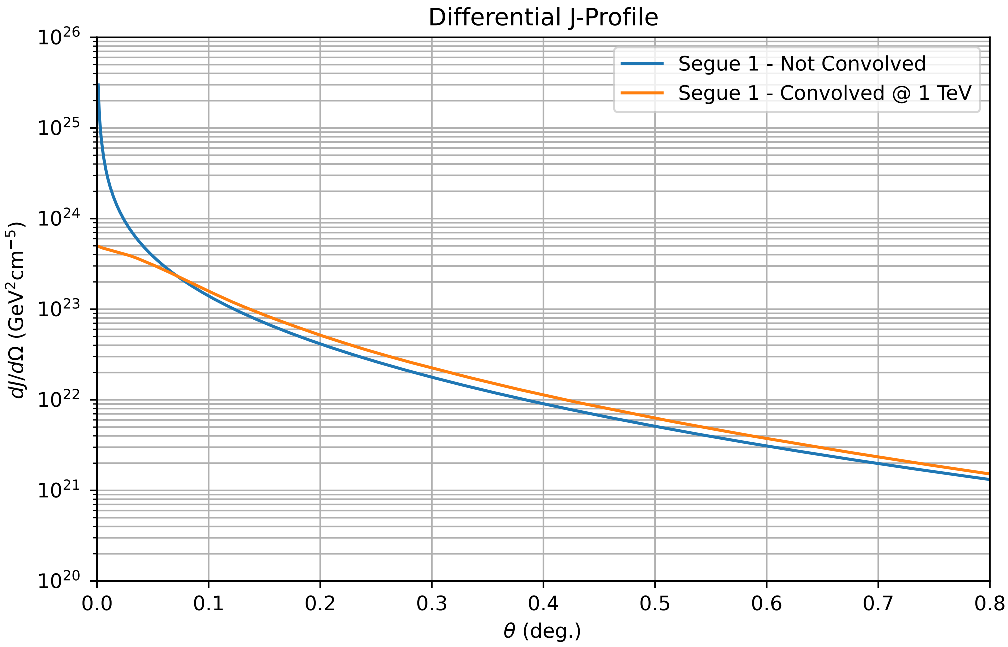

Figure 50: The differential J-Profile of Segue 1, NFW parameters are obtained from Ando+20. It is shown both before (Blue) and after (Orange) being convolved (Section 6.4) with the energy dependent PSF at 1 TeV.

This can now be integrated out to a chosen angular extension to give the J-Factor which describes the DM luminosity at a particular point on the sky. The J-Factor for DM annihilation is:

$$J(\Delta\Omega) = \int_{\Delta\Omega} \int_0^\infty \rho^2(l,\Omega) dl d\Omega \tag{28}$$

and is given in units of GeV^2 cm^{-5} and in the case of decay it is

$$D(\Delta\Omega) = \int_{\Delta\Omega} \int_{los} \rho(l,\Omega) dl d\Omega \tag{29}$$

with units of GeV cm^{-2}. Figures 50 and 51 shows examples of both the differential and angular J-Profiles of Segue 1 respectively.

For each dSph a set of 10000 integral J-Factors are produced using different sets

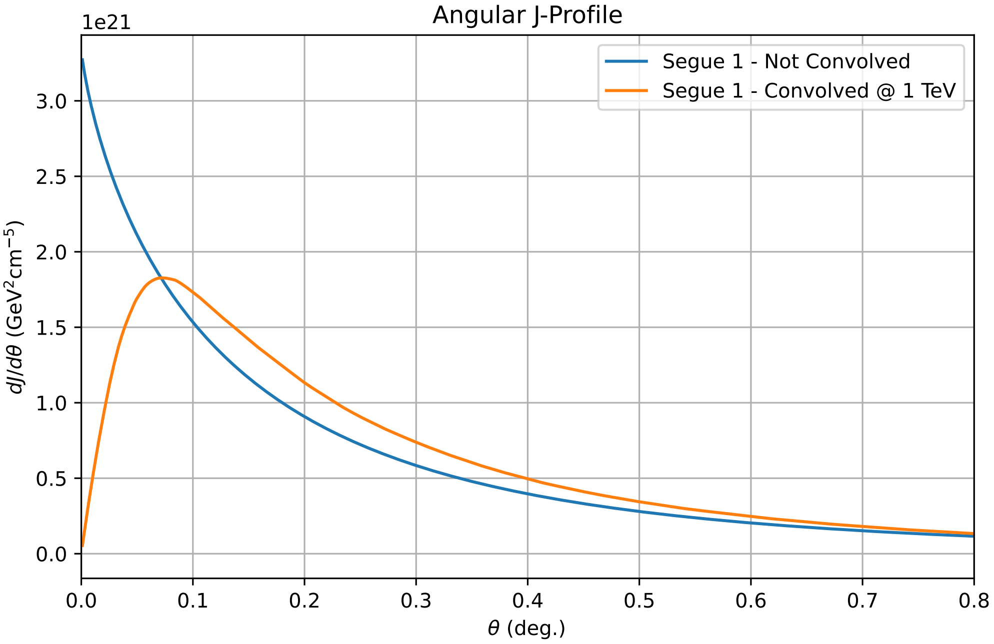

Figure 51: The angular J-Profile of Segue 1, NFW parameters are obtained from Ando+20. It is shown both before (Blue) and after (Orange) being convolved (Section 6.4) with the energy dependent PSF at 1 TeV

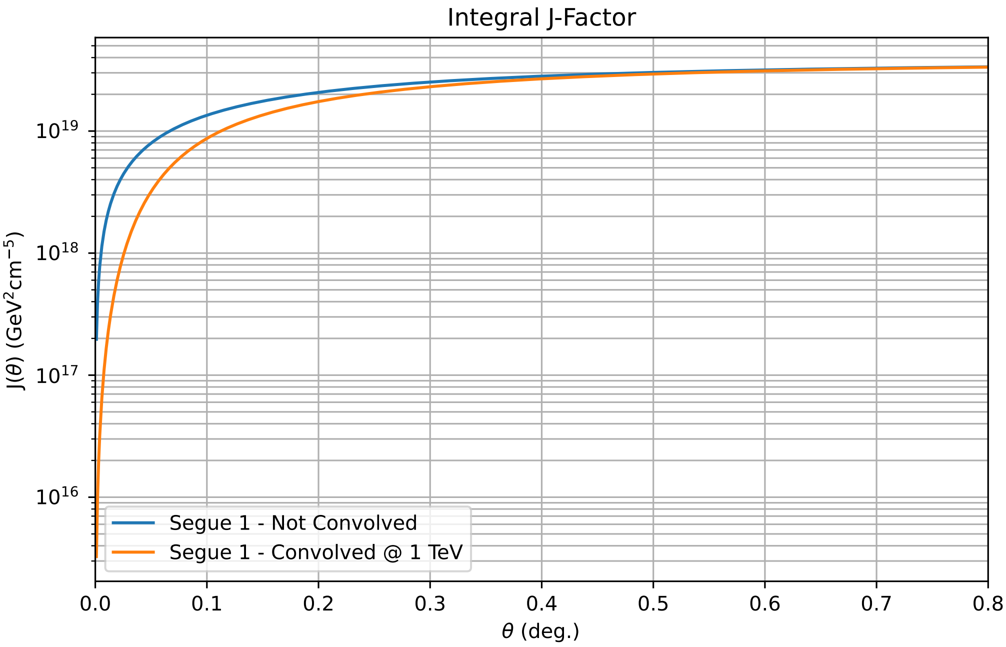

Figure 52: The integral J-Factor of Segue 1 both before (Blue) and after (Orange) being convolved with the energy dependent PSF

of NFW parameters. The integral J-Factor is then convolved with the VERITAS energy dependent PSF. This is most easily done in Fourier space by multiplying the Hankel transforms (Hamilton 2000) of both the PSF and the integral J-Factor and then performing an inverse Hankel transform on the the product of the two. The PyHank[5] Python package is used to perform the Hankel transforms in this thesis. Figure 52 shows an example of an integral J-Factor both before and after being convolved with the energy dependent PSF at 1 TeV. An angular cut comparable to the energy dependent VERITAS PSF is then placed on the convolved integral J-Factor to get an energy dependent value for the DM density in a selected dSph. Figure 53 shows how the integral J-Factor of a dSph can extend up to $> 0.5°$ and is greatly effected by the angular cut. As exact values for the J-Factor of any dSph are unknown and instead NFW parameters are randomly sampled from a probability

---

[5] https://github.com/etfrogers/pyhank

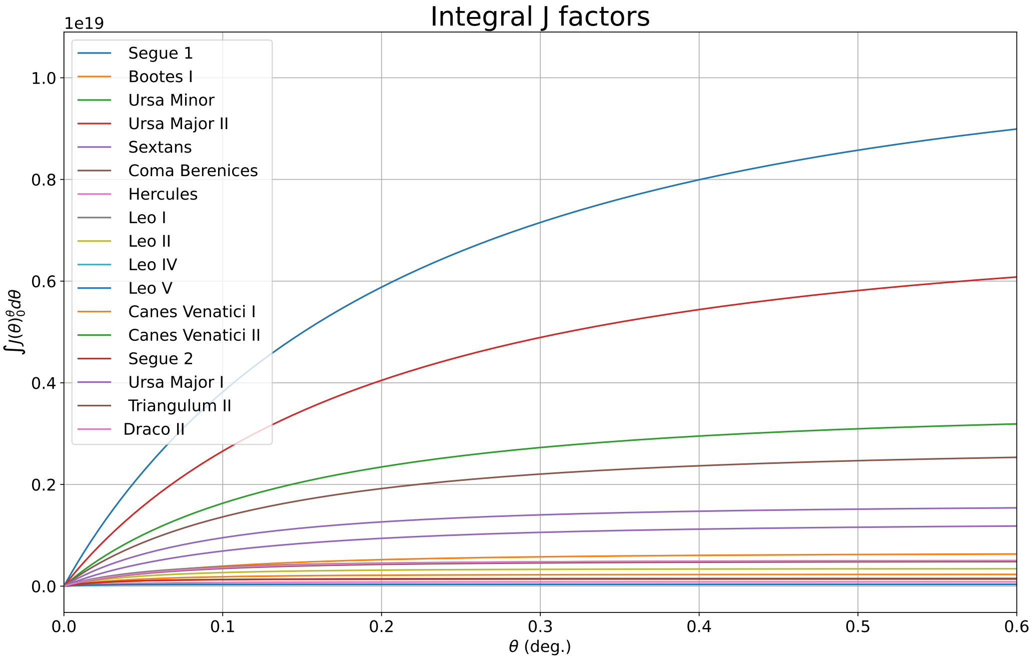

Figure 53: Integral J-Factors (before convolving with the VERITAS PSF) of all 17 dSphs included in this study.

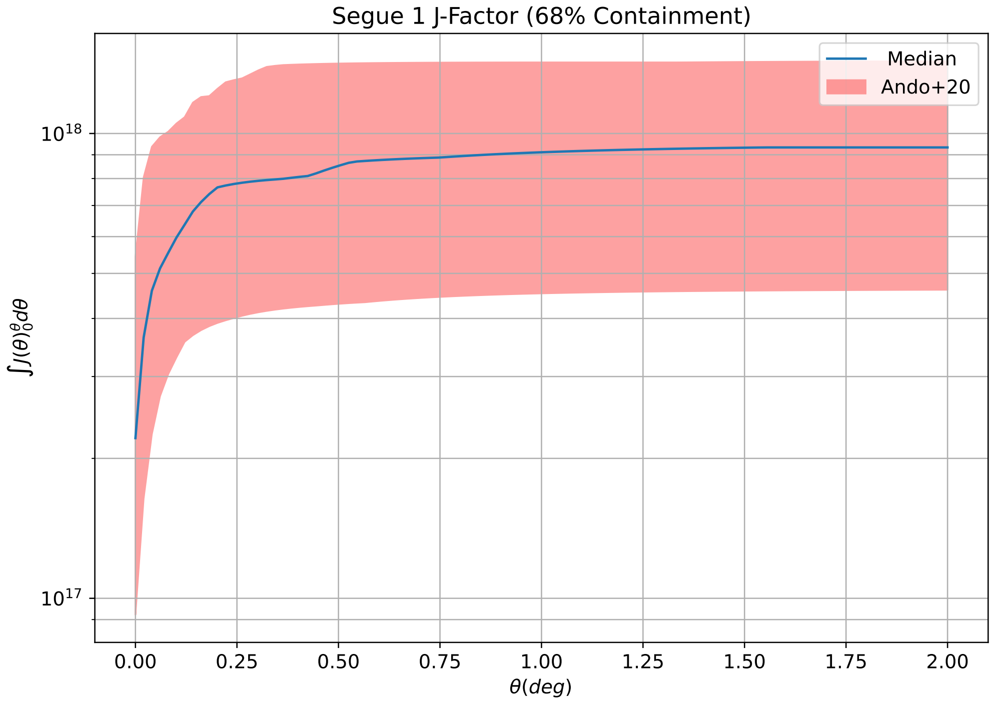

Figure 54: 68% containment fraction from 1000 realisations of Segue 1's J-Factor (shaded band) and the median J-Factor which is the chosen J-Factor for this analysis

density function (PDF) there is an uncertainty factor introduced (see Figure 54) for this reason the median J-Factor of the set is used. This ensures that the DM density in a given dSph is neither overestimated nor underestimated.

6.5 Dark Matter Gamma-Ray Flux

The expected flux of gamma rays from annihilation or decay of DM is based on two terms: the *particle physics factor* (Φ_{PP}) and the J-Factor which is otherwise known as the *astrophysical factor*. The *particle physics factor* contains the gamma-ray spectrum $\frac{dN_\gamma}{dE_\gamma}$ produced by a given decay or annihilation channel, the velocity averaged cross section of the DM particle $\langle\sigma\nu\rangle$ and the DM particle mass m_{DM}. By combining these factors, the predicted gamma-ray flux from DM annihilation is:

$$\phi_s(\Delta\Omega) = \underbrace{\frac{1}{4\pi}\frac{\langle\sigma v\rangle}{2m_{DM}^2}\int_{E_{min}}^{E_{max}}\frac{dN}{dE}dE}_{\Phi_{PP}} \times \underbrace{\int_{\Delta\Omega}\left[\int_{l.o.s.}\rho^2(\mathbf{r})dl\right]d\Omega'}_{J-Factor} \tag{30}$$

and from decay by :

$$\phi_s(\Delta\Omega)\underbrace{\frac{1}{4\pi}\frac{\Gamma}{m_{DM}}\int_{E_{min}}^{E_{max}}\frac{dN_\gamma}{dE_\gamma}dE_\gamma}_{\Phi_{PP}} \times \underbrace{\int_{\Delta\Omega}\left[\int_{l.o.s.}\rho(\mathbf{r})dl\right]d\Omega'}_{J-Factor} \tag{31}$$

as the DM gamma-ray flux from annihilation is greater than from decay and the rate of annihilation is proportional to the square of the DM density which favours the VERITAS data set only upper limits will only be placed on the annihilation cross-section in this analysis.

6.6 Maximum Likelihood Analysis

When a set of unknown parameters can be used to describe a model or function, often the best methods of finding the estimate for these parameters is through the use of a maximum likelihood estimation (MLE). A MLE relies on finding the values for each parameter which will maximise the likelihood of the observed results occurring. Assuming there are N measurements of some independent variable : $\{x\}$ and a variable dependent on $\{x\}$: $\{y\}$ and a functional relationship which describes them :

$$y_i = f\left(x_i, a_1, a_2, ..., a_m\right) = \{y\} = f\left(\{x\}, \{a\}\right) \tag{32}$$

the goal of an MLE is to find the most probable values for $\{a\}$. In order to do this, a normalised probability P_i of whether the observed data y_i agrees with the predicted $f(x_i)$ is generated.

$$P_i \equiv P\left(x_i; a_1, a_2, ..., a_m\right) = P\left(x_i, \{a\}\right) \tag{33}$$

The likelihood is then the product of these individual probabilities :

$$\mathcal{L} = \prod_{i=1}^{N} P_i \tag{34}$$

In order to ease computation the natural log of the likelihood function is commonly used:

$$\ln \mathcal{L} = \sum_{i=1}^{N} \ln P_i \tag{35}$$

$\mathcal{L}$ can then be maximised in order to find the values for each parameter that best describes the data :

$$\left.\frac{\delta \ln \mathcal{L}}{\delta a_j}\right|_{\{\hat{a}_j\}} = 0 \tag{36}$$

If N is large enough ($> \sim 10$ ("Central Limit Theorem" 2008)) the errors are then assumed to be Gaussian. For Gaussian errors maximising $\log \mathcal{L}$ is equivalent to minimising χ^2:

$$-2 \log \mathcal{L} \sim \chi^2 \tag{37}$$

Then the χ^2 distribution (or -2log $\mathcal{L}$) will be parabolic at its minimum and

$$\frac{1}{\sigma^2} = -\frac{\delta^2 \ln \mathcal{L}}{\delta a^2} \tag{38}$$

where σ^2 is the variance. Confidence intervals can also be estimated from changes from the minimum in the χ^2 distribution. As a one-sided confidence interval is used in this analysis the 95% upper limits correspond to -2log $\mathcal{L}$ = -2.71 as for a one-sided confidence interval

$$\chi^2 (x, 1) = 2C - 2 \tag{39}$$

where C is the χ^2 test critical value.

6.6.1 Likelihood Ratio Test

The "Likelihood Ratio Test" can be used to compare how much better one model describes data than another. This is traditionally done by comparing the null hypothesis to an alternative hypothesis. The Likelihood ratio can then be defined as

:

$$Ratio = \frac{\mathcal{L}_{null}}{\mathcal{L}_{measured}} \tag{40}$$

where $\mathcal{L}_{null}$ is the likelihood of the null hypothesis and $\mathcal{L}_{measured}$ is the likelihood of the measured data. Wilk's theorem (Wilks 1938) states that this ratio will be χ^2 distributed where the number of degrees of freedom given by the difference in free parameters between the two models. The test statistic (TS) is then :

$$TS = -2\log\left(\frac{\mathcal{L}_{null}}{\mathcal{L}_{measured}}\right) \tag{41}$$

where the TS can be used as a means to measure how much better $\mathcal{L}_{measured}$ describes the data than the null hypothesis. As a χ^2 distribution with 1 DOF is equivalent to a Gaussian squared, the significance of a detection is given by $\sqrt{TS}$. In the case of this research the likelihood ratio test can be used to estimate a value for $\langle\sigma v\rangle$ by comparing the null hypothesis ($\langle\sigma v\rangle = 0$) to the likelihood profile with respect to b (the background) and $\langle\sigma v\rangle$. Where the likelihood profile is obtained by varying the value of $\langle\sigma v\rangle$ and b while keeping all other parameters constant and calculating the likelihood function at each point.

6.6.2 Maximum-Likelihood Methods for an Indirect DM Search

A maximum-likelihood method (MLM) can be used to estimate gamma-ray (g) and background (b) fluxes IACT (Rolke, López, and Conrad 2005). By taking the number of observed events in the *ON* region as $N_{on} = N_g + N_b$ where N_g and N_b are the number of gamma-ray and background events in the *ON* region respectively and the number of observed events in the *OFF* region as N_{off}. The following likelihood function can be defined as the product of two Poisson probabilities :

$$\mathcal{L} = \frac{(g+\alpha b)^{N_{on}}}{N_{on}!}e^{-(g+\alpha b)} \times \frac{(b)^{N_{off}}}{N_{off}!}e^{-b} \tag{42}$$

where α is the background normalisation factor defined in Section 4.5.1. For a DM search the likelihood function can be improved by the addition of the DM gamma-ray spectrum. The alternative likelihood function which is modified to account for the DM gamma-ray spectrum is :

$$\mathcal{L} = \frac{(g+\alpha b)^{N_{on}} e^{-(g+\alpha b)}}{N_{on}!} \frac{b^{N_{off}} e^{-b}}{N_{off}!} \prod_{i=1}^{N_{on}} P_i(E_i|M, \langle\sigma\nu\rangle) \tag{43}$$

where g is the expected flux from DM decay/annihilation at a given DM mass and velocity-averaged cross section :

$$g = \frac{\langle\sigma\nu\rangle\, T_{obs}}{4\pi 2 m_{DM}^2} \int_0^\infty \int_0^\infty \frac{dN}{dE'} J(E')A(E')D(E|E')dE'dE \tag{44}$$

where T_{obs} is the total exposure time, $\frac{dN}{dE'}$ is DM annihilation spectrum, $J(E')$ is the integrated J-factor convolved with the instrument's energy-dependant PSF, $A(E')$ is the instrument's effective area and $D(E|E')$ is the energy dispersion matrix (the probability of an *ON* event with true energy E' having a reconstructed energy E). $P_i(E_i|M, \langle\sigma\nu\rangle)$ is the probability of measuring an *ON* event i with energy E_i :

$$P_i(E_i|M, \langle\sigma\nu\rangle) = \frac{\alpha b p_{off}(E_i) + g p_{on}(E_i)}{\alpha b + g} \tag{45}$$

where $p_{on/off}$ are the expected differential probabilities from the *ON* and *OFF* regions. In the case of this analysis p_{off} is generated from a normalised distribution of the energies of all background events and p_{on} is generated from the normalised histogram of expected DM events. The negative of the log likelihood function $(-\log\mathcal{L})$ is then minimised with respect to $\langle\sigma\nu\rangle$ and b (a nuisance parameter) :

$$\log\mathcal{L} = N_{off}\ log\ b - g - (1+\alpha)b + \sum_{i=1}^{N_{on}} log(\alpha b p_{off,i} + g p_{on,i}) \tag{46}$$

The sensitivity of this analysis can be improved through the use of a joint likelihood analysis where the likelihood functions from each dSph is combined :

$$\mathcal{L}_{combined} = \prod_{i=1}^{NdSph} \mathcal{L}_i\left(\langle\sigma\nu\rangle\, ; b_i|D_i\right) \tag{47}$$

The minimisation of the MLE (Equation 46) is performed using pyROOT - a python implementation of ROOT (Brun et al. 2019). Two parameters are kept free during the minimisation : b the expected number of background events and $\langle\sigma v\rangle$ the velocity

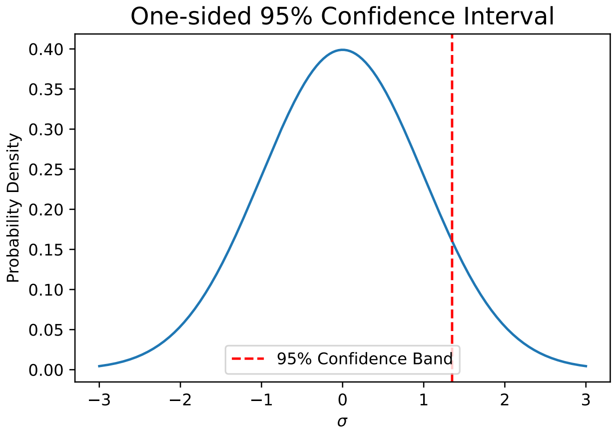

Figure 55: Example of a one-sided 95% confidence level upper limit.

averaged annihilation cross-section. The significance of the DM signal over the background is calculated by :

$$\lambda = -2 \log \frac{\mathcal{L}_{null}}{\mathcal{L}_{alt}} \tag{48}$$

where in the case of this analysis the null hypothesis is the case with no signal ($\langle \sigma v \rangle = 0$) and only b will vary in the minimisation. The alternative hypothesis is the case where $\langle \sigma v \rangle \neq 0$ and both $\langle \sigma v \rangle$ and b are allowed to vary. If $\lambda < 25$ which is the equivalent to 5σ an upper limit can by obtained with the likelihood profile by finding the value for $\langle \sigma v \rangle$ that corresponds to $\Delta log\mathcal{L} = 1.35$ - the one-sided 95% confidence interval. Figure 55 shows an example of a one-sided 95% confidence level upper limit. The upper limit value of 1.35 corresponds to the 90% upper limit of a two-sided confidence interval as 90% in the two-sided case (45% + 45%) is equal to the one-sided value of 95% one-sided (50% + 45%).

6.7 Expected Limits

If the observations taken for this experiment were taken multiple times and the remainder of the analysis left unchanged a distribution of upper limits (ULs) is expected due to statistical fluctuations. These fluctuations can be measured by producing a set of random *ON* and *OFF* events and repeating the analysis for each.

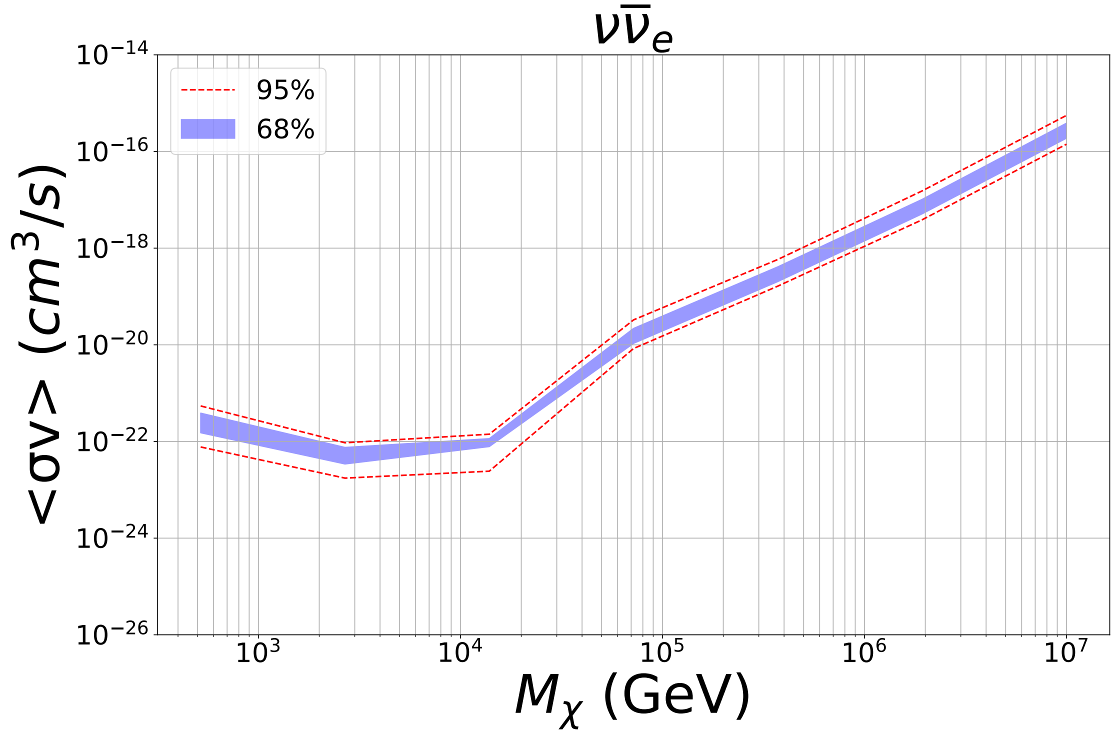

Figure 56: Expected bands (blue band represents the 68% containment and red dashed lines represents the 95% containment) of combined likelihood analysis due to statistical fluctuations on both *ON* and *OFF* events produced with 50 realisations of the data set.

This is done by filling the *ON* and *OFF* event lists with Poisson randomised events taken with replacement from the true data set, then performing the analysis as discussed. 68% and 95% containment bands are then placed on the results. Figure 56 shows an example of the expected limits from a single combined extended-source analysis.

7 Results

Presented in this chapter are the results of both the point-source and extended-source analyses of 17 dSphs (16 in the case of the extended-source analysis). In both cases the results of the standard VERITAS analyses are shown first. Following this the presence of DM annihilation signals are tested with a MLE and finally upper limits on the thermally averaged cross-section $\langle \sigma \nu \rangle$ of DM annihilation are shown. These limits are placed on 9 different annihilation channels through the use of a combined likelihood analysis of all 16 (extended source) or 17 (point source) dSphs.

7.1 Point-Source Analysis

Standard VERITAS moderate ITM cuts are chosen for the ITM point source analysis of each dSph. Moderate cuts are used in order to maximise sensitivity in the 100 GeV to 10 TeV mass range. As Fermi-LAT upper limits dominate in the mass range below this it was determained that the benefits that would come from the use of soft cuts would be outweighed by the negatives. In all cases an angular cut of 0.07° is applied and the reflected region background estimation is used. The significance distributions of the skymaps of each dSph is first checked to ensure there is no leaking of *ON* events into the background. This is done finding the Li&Ma significance (Li and Ma 1983) at points covering the whole of the skymap (while excluding the *ON* region). For a field with no gamma-ray source one should expect the significance distributions to be normally distributed around 0 with a standard deviation of 1. As the significance distributions of all dSphs adhere to these criteria, the source analysis can progress and the significance of the *ON* region is then measured. The results of the standard VERITAS point-source analyses are presented in Table 3 where columns 2 and 3 show the number of *ON* and *OFF* counts, column 4 shows the significance of the signal in the *ON* region above the background (using (Li and Ma 1983) equation 17) and column 5 shows the background normalisation factor. There is no significant signal above the background from any dSph.

Dwarf	Exposure [Hours]	N_{ON} [counts]	N_{OFF} [counts]	α	Significance [σ]
Böotes I	13.98	112	1981	0.065	-1.5
Coma Berenices	39.76	239	3234	0.067	1.4
CVn I	9.72	46	695	0.064	0.2
CVn II	8.14	23	434	0.061	-0.7
Draco II	8.02	16	245	0.067	-0.1
Hercules I	9.46	45	849	0.061	-1
Leo I	5.66	23	385	0.067	-0.7
Leo II	11.31	63	1092	0.066	-1.1
Leo IV	0.48	3	59	0.060	-0.3
Leo V	1.38	2	50	0.066	-0.7
Segue I	126.29	1434	21080	0.068	0.0
Segue II	12.51	89	631	0.063	-0.8
Sextans I	7.45	33	1262	0.060	0.2
Triangulum II	29.51	159	2602	0.061	0.0
Ursa Major I	6.63	37	568	0.059	0.6
Ursa Major II	212.32	924	14418	0.064	0.2
Ursa Minor	135.3	598	9759	0.064	-1.1

Table 3: Results of the VERITAS analysis of 17 dSphs. The second and third columns give the counts of gamma-like events in the *ON* and *OFF* regions. The excess significance is given in the fourth column in terms of standard deviations above the background.

Figure 57 shows the distribution of the significance of excesses from each dSph compared to the expected distribution from a field with no gamma-ray source. The similarity between the two distributions shows the lack of any gamma-ray source. Also shown is the cumulative significance distribution from all dSphs accumulated by dSph. The cumulative significance distribution of all dSphs achieves a significance of $\sim 0.1\sigma$, which is below 5σ (the value for a statistically significant detection to be achieved). This also shows that there is no source of gamma rays present.

7.1.1 Dark Matter Upper Limits

Each of the nine annihilation channels (e^+e^-, $\mu^+\mu^-$, $\tau^+\tau^-$, $t\bar{t}$, $b\bar{b}$, W^+W^-, ZZ, $\gamma\gamma$, and $\nu_e\bar{\nu}_e$) are tested with the use of a MLE. In all cases, there is no evidence for the presence of DM annihilation signals. Table 4 shows the significance for

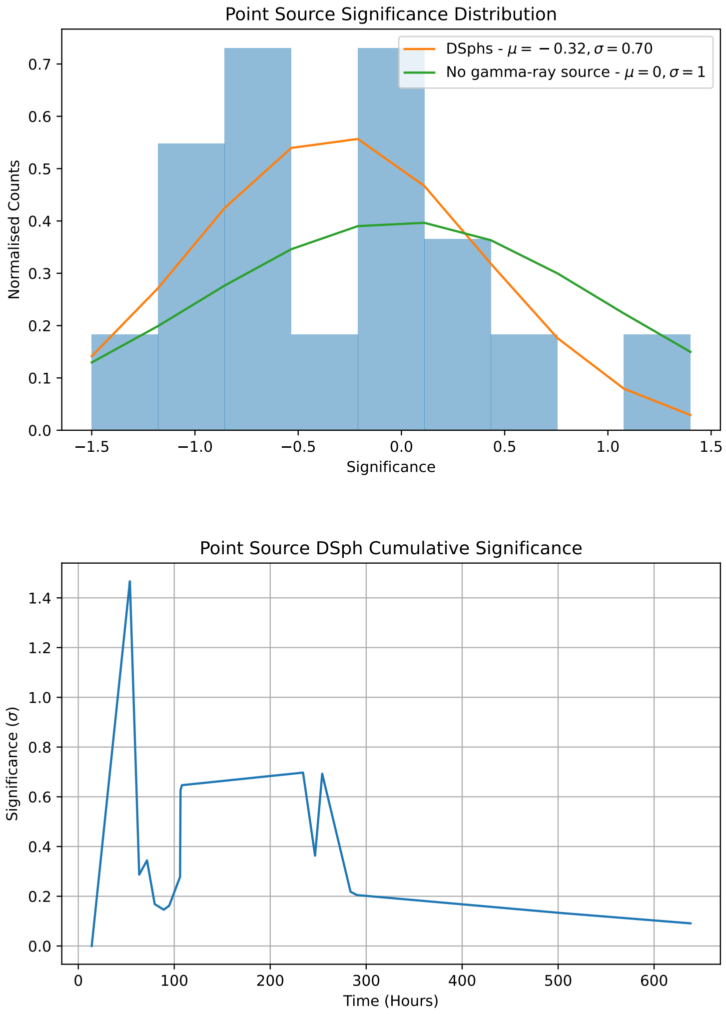

Figure 57: The significance distribution of the 17 point-source analyses (top) the orange curve is a normal distribution fitted to the distribution, the green curve shows the expected distribution of a field with no gamma-ray sources. There is no indication of a gamma-ray excess from the significance distribution. The cumulative significance (bottom) also shows no indication of a gamma-ray excess.

dSph	e^+e^-	$\mu^+\mu^-$	$\tau^+\tau^-$	$t\bar{t}$	$b\bar{b}$	W^+W^-	ZZ	$\gamma\gamma$	$\nu_e\bar{\nu}_e$
Bootes	0	0	0	0	0	0	0	0	0
Coma Berenices	0.53	0.53	1.2	1.32	1.24	1.02	1.35	0	1.32
CVn I	0.79	0.79	0.54	0.24	0.32	0.56	0.19	0.97	0.39
CVn II	0	0	0	0	0	0	0	0	0
Draco II	0.59	0.59	0.02	0	0.01	0.04	0	0.93	0
Hercules I	0	0	0	0	0	0	0	0.19	0
Leo I	0	0	0	0	0	0	0	0.11	0
Leo II	1.55	1.55	0.94	1.67	1.03	0.97	0.98	2.32	1.61
Leo IV	0.64	0.64	0.58	0.87	1.01	0.4	0.95	1.01	0.3
Leo V	0	0	0	0	0	0	0	0	0
Segue I	0.11	0.11	1.15	0.22	0.22	0.02	0.01	1.76	0.01
Segue II	0	0	0	0	0	0	0	0	0
Sextans I	1.47	1.47	1.26	1.7	1.7	1.7	1.63	2.55	1.57
Triangulum II	0	0	0	0	0	0	0	0	0
Ursa Major I	0.19	0.21	0.57	0.59	0.46	0.57	0.59	0	0.92
Ursa Major II	2.18	2.16	0.61	0.6	0.59	0.91	0.54	2.79	0.53
Ursa Minor	1.32	1.33	0	0.14	0.41	0	0	1.02	2.87

Table 4: The peak significance of signal from the point-source analysis of each dSph in each annihilation channel.

each dSph in each annihilation channel. 95% upper limits are placed on $\langle\sigma\nu\rangle$ at 8 logarithmically distributed masses between 100 GeV and 10 PeV through the use of a MLE as discussed in Section 6.6.2. Each panel of Figure 59 corresponds to a specific annihilation channel and within each panel the upper limits for each dSph are presented. The results from each of the 17 dSphs are also combined in order to maximise statistics and achieve generally more constraining upper limits. The black curves in Figure 59 show the results from the joint analysis of all 17 dSphs in each annihilation channel. Figure 58 shows an example of the combined (and individual dSph) likelihood profiles used when deriving the 95% upper limit.

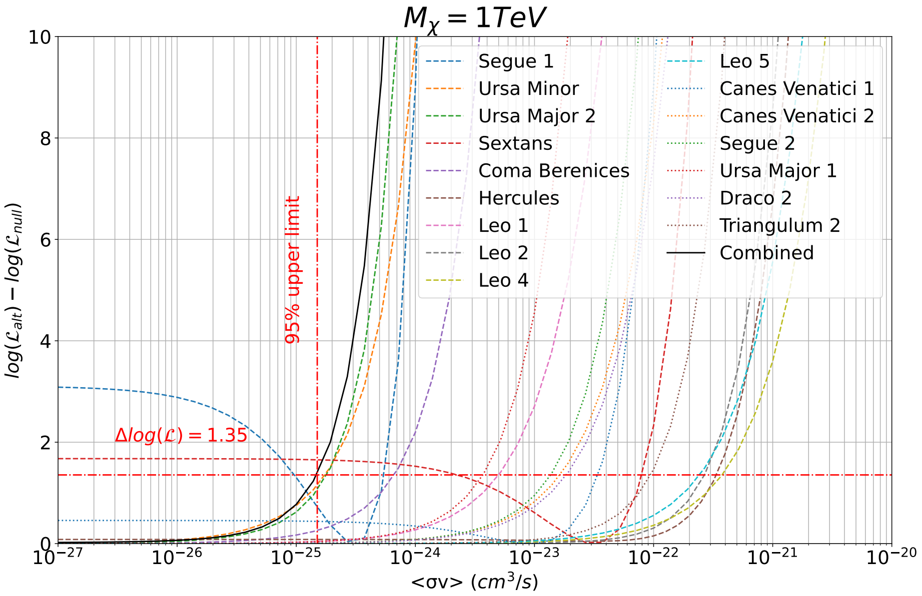

Figure 58: Likelihood curves from the joint analysis of 17 dSphs with a DM mass of 1 (TeV). The horizontal line corresponds to the one-sided 95% upper limit.

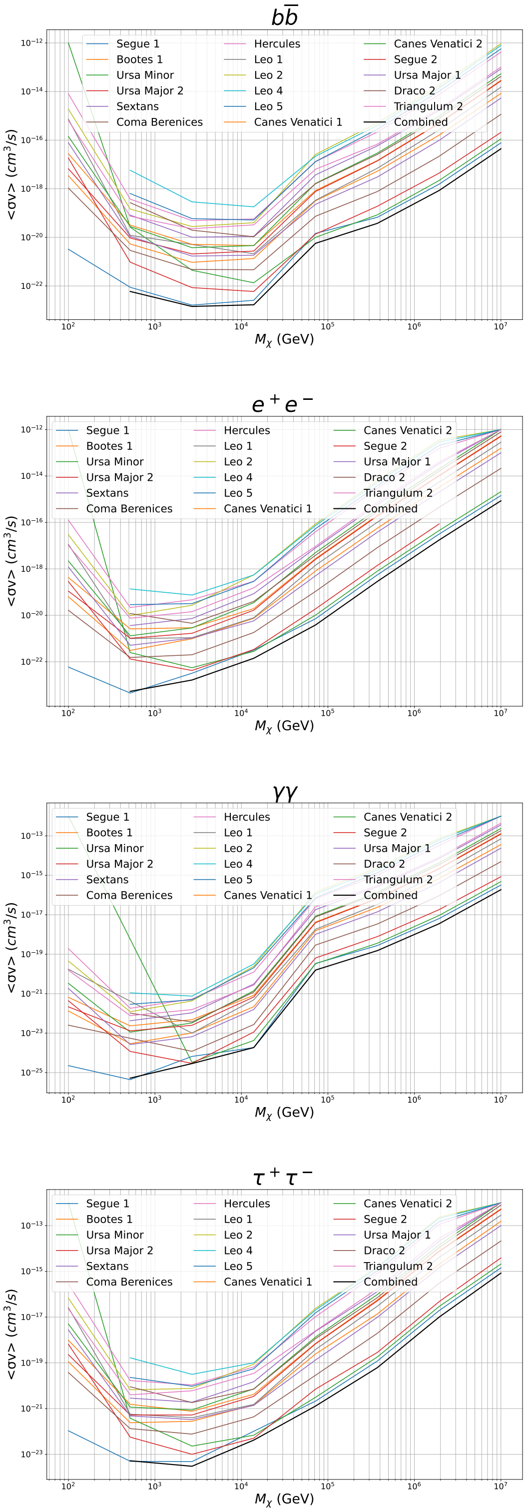

Figure 59: The 95% upper limit on the DM annihilation cross section for each of the 17 dSphs (point source). Each panel shows the results of each dSph in four annihilation channels (the remainder are presented in the appendix of this thesis) as well as the combined limit (black).

As discussed in Section 6.7, statistical fluctuations in *ON* and *OFF* events will affect the results of the upper limit search. A set of 50 limits are produced for each annihilation channel in each dSph, where each limit is found by producing a randomised data set based on the true measured data set with the J-Factor held constant. These limits are then combined and the 68% and 95% containment bands are found. For each limit produced *ON* and *OFF* events are randomly sampled with replacement from measured *OFF* with the number of events being randomly chosen where:

$$N_{ON} = Pois\left(\alpha N_{OFF}\right) \tag{49}$$

and

$$N_{OFF} = Pois\left(N_{OFF}\right) \tag{50}$$

Figure 60 shows the 68% containment (blue shaded), 95% (red dashed) containment and measured upper limit (black) of the joint MLE expected limits for each annihilation channel.

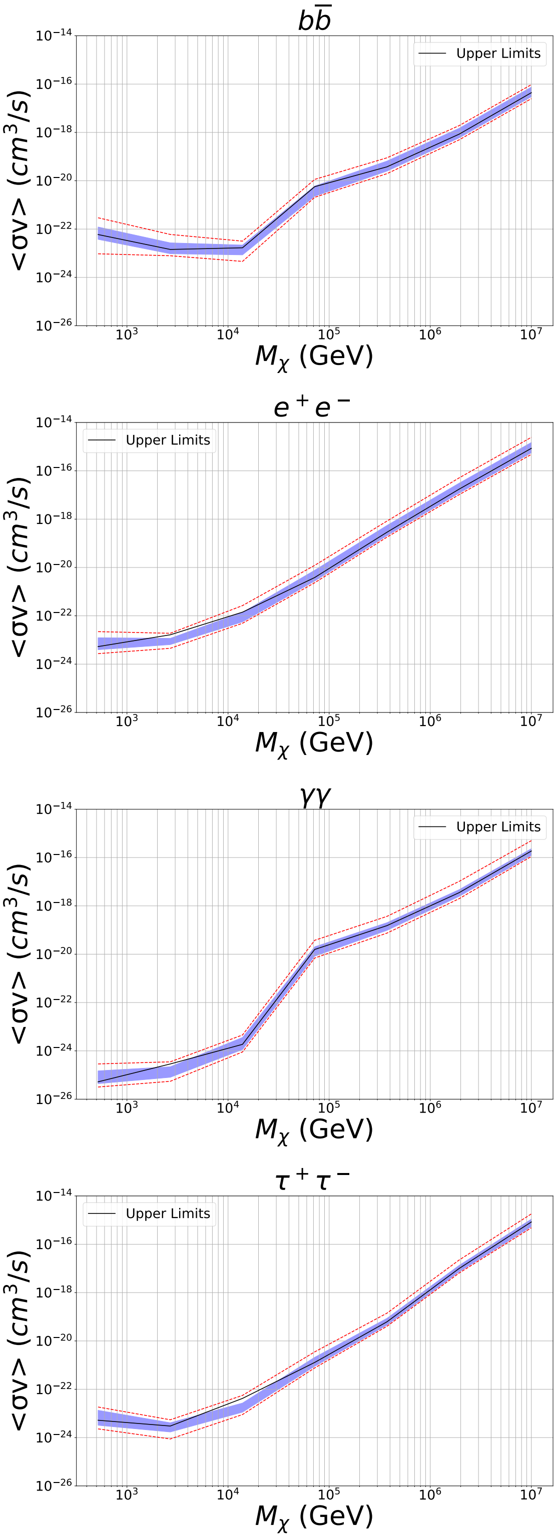

Figure 60: 68% (blue bands) and 95% (dashed red) expected limits for DM annihilation cross section for each of the 17 dSphs (point source). The measured upper limits (black) which fall within the bounds of the expected limits are also shown. Bands are generated from 50 random realisations of the signal and background. Once again the remaining channels are shown in the appendix of this thesis

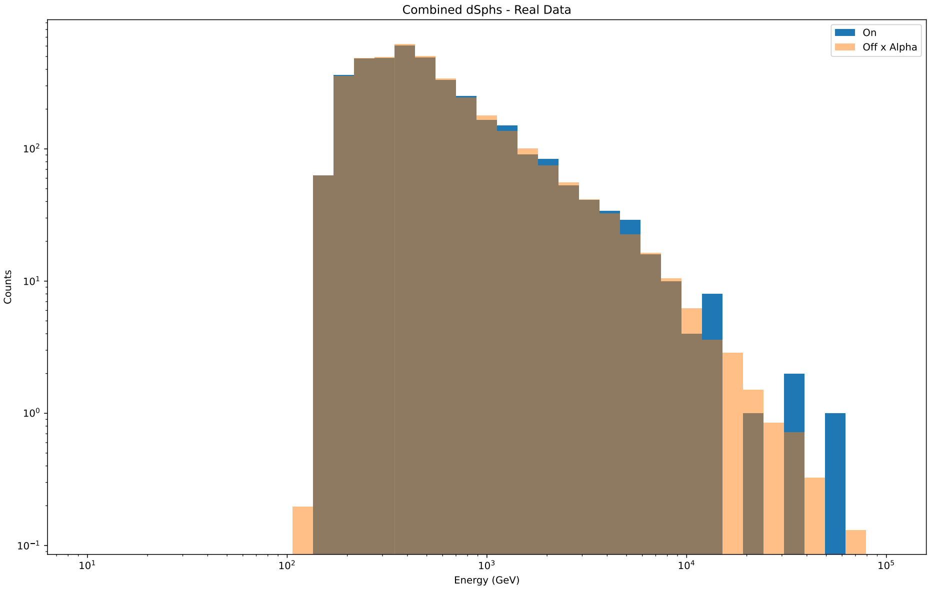

Figure 61: Energy distribution of ON and αOFF events (all 17 data sets combined) of the true data used in the upper limit calculation.

As the measured upper limits fall within the bounds of the Poisson fluctuations it can be used as a means of validation of the limits measured. The expected limits also show the most constraining limits that could have been achieved under this experiment's conditions. Figures 61 and 62 show examples of the energy distribution of the measured and a single set of randomised ON and OFF events.

The value of the J-Factor has a significant impact on the upper limit search. The median J-Factor of a set of 10000 J-Factor realisations is used for this analysis. Figure 63 shows the 68% containment obtained from 50 different J-Factor realisations. Finally Figure 64 compares the upper limits from the joint MLE of all 17 dSphs in the $\chi\chi \rightarrow \tau^+\tau^-$ annihilation channel to the most recent published results from other indirect DM searches. This work presents some of the earliest and most constraining upper limits in the ultra-heavy DM mass range ($M_{DM} > 100$ TeV). Below the ultra-heavy mass range the limits derived from this work appear mostly comparable to the current state of the art. It is important to note here that to make

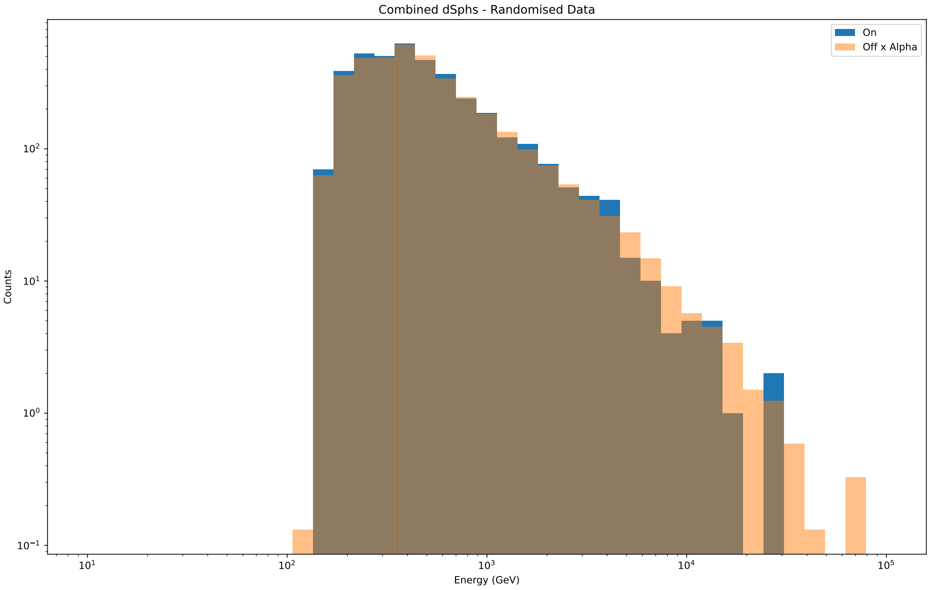

Figure 62: Energy distribution of ON and αOFF events (all 17 data sets combined) of one set of randomised data used in the expected limits calculation.

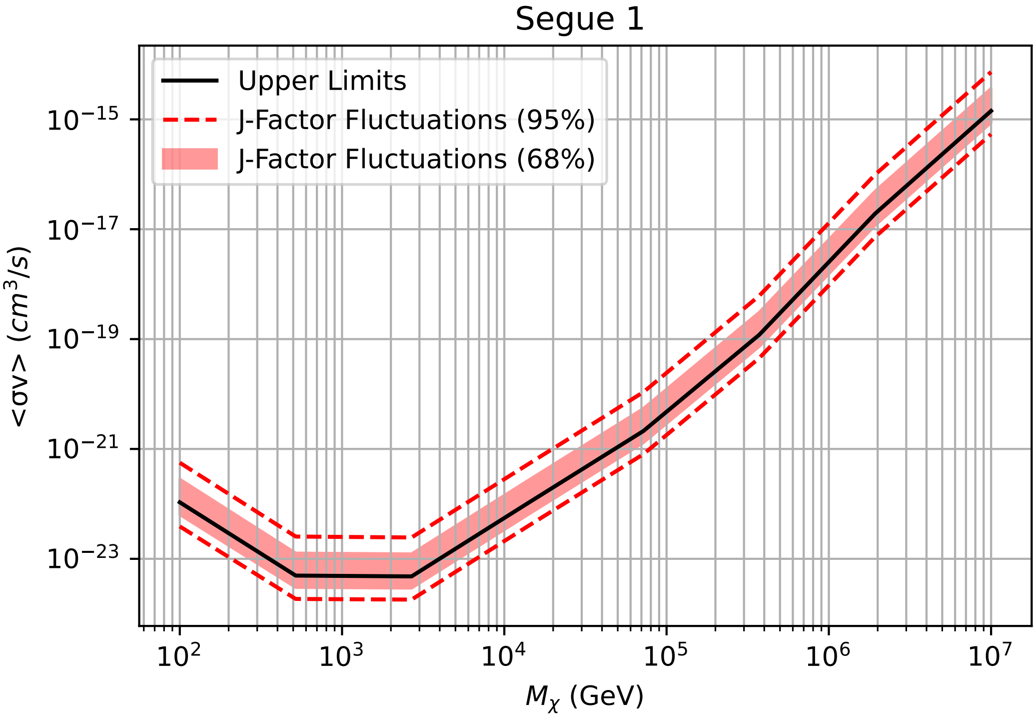

Figure 63: Segue I annihilation cross section upper limits. The shaded (dotted-line) uncertainty band shows the 68% (95%) containment obtained from 50 realizations of viable dark matter density profiles. The black line is the result achieved using the median of 10000 viable J-Factors.

a fair comparison between these results the values of the J-Factors used in the analyses must be considered (see Section 7.2). The upper limits presented here do not pass the expected thermally averaged annihilation cross section for a thermal-relic DM scenario (dashed horizontal line in Figure 64). If the annihilation cross section was measured below this value the "WIMP Miracle" as it is currently interpreted would be disproved. As this limit is not reached the WIMP DM model can not yet be ruled out. In order to reach the relic limit at $\sim$ 2 TeV VERITAS would require a data set with 100 times the exposure of the current VERITAS data set. This can be predicted as $\langle\sigma v\rangle_{t_1} / \langle\sigma v\rangle_{t_2} \propto t_2/t_1$ and the current VERITAS upper limit at M_χ = 2 TeV is $3\times10^{-24} cm^3 s^{-1}$.

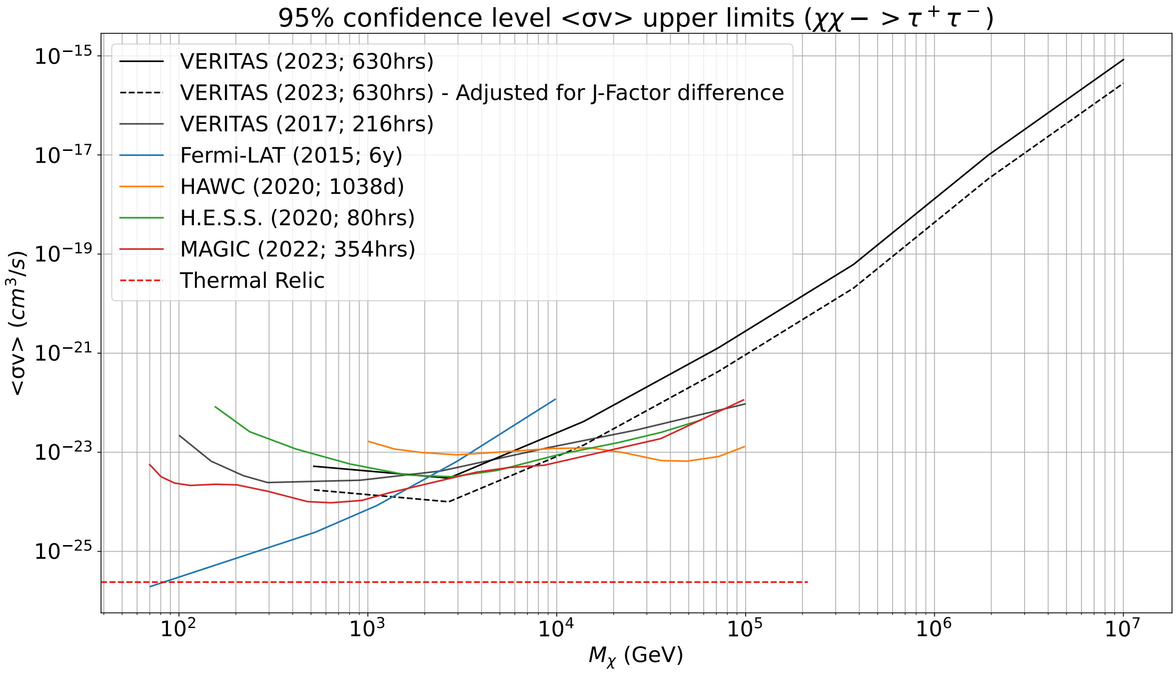

Figure 64: VERITAS upper limit curves obtained from point source analyses of 17 dSphs compared with other published upper limit curves including a past VERITAS result (grey) (Archambault et al. 2017). All curves show 95% confidence upper limits on the dark matter thermally averaged annihilation cross section for the $\tau^{+}\tau^{-}$ annihilation channels. The solid black line shows the limits found in this analysis and the dashed black line is the same curve lowered by a factor of 3 in order to account for the ratio of Ando+20 to GS+15 J-Factors. The results from other searches are (Hoof, Geringer-Sameth, and Trotta 2020) (Fermi-LAT; blue line), (Acciari et al. 2022) (MAGIC; red line), (Abdalla et al. 2018) (H.E.S.S.; green line), and (Albert et al. 2018) (HAWC; orange line). The horizontal red dashed line is the expected thermally averaged annihilation cross section for a thermal-relic DM scenario ($\langle\sigma\nu\rangle \approx 2.4\times$ 10 $^{-26}$ cm^3/s).

From limits placed on $\langle\sigma\nu\rangle$ above the unitarity limit, upper limits on the potential geometrical cross section of a non-point-like DM particle can be found. Through the relationship:

$$\langle\sigma\nu\rangle \leq 4\pi\frac{(1+M_{\chi}v_{rel}R)^{2}}{M_{\chi}^{2}v_{rel}} \tag{51}$$

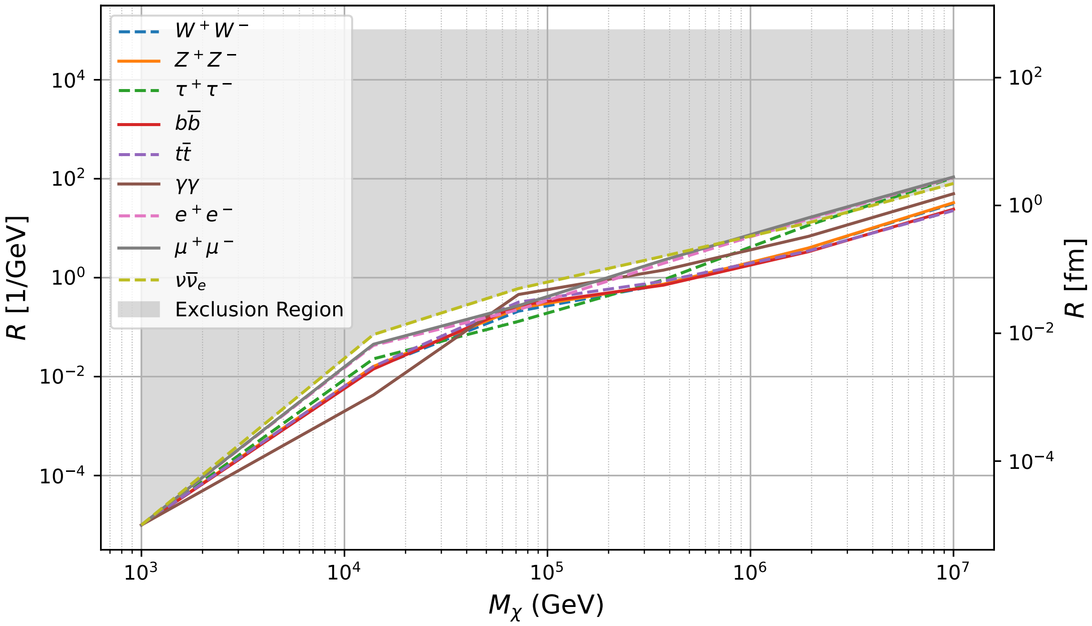

Figure 65: 95% confidence upper limits curves on the radius (femtometers) and 1/E, of a UHDM particle from the combined point-source analysis. The nine annihilation channels considered are all shown. The shaded areas show exclusion regions set by this analysis.

where the relative velocity between dark matter particles in dSph $v_{rel}/c = 2 \times 10^{-5}$ (Martinez et al. 2011) and R is the radius of a composite UHDM particle. Figure 65 shows the upper limits placed on the size of radius of the UHDM particle. This shows that below a DM mass of 10 PeV, DM particles with a radius greater than $\sim$ 5 fm can be rejected in all channels.

7.2 J-Factor Comparison

Table 5 shows the J-Factor estimates from GS+15 and Ando+20 as well as the ratio of them to each other. In most cases the J-Factors estimated by Ando+20 are smaller than those estimated by GS+15 (Geringer-Sameth, Koushiappas, and Walker 2015) (a popular estimation used in other analyses), which leads to a less

Dwarf	$\log_{10}J(0.5^o)$ [GeV^2/cm^5]		ratio
	Ando+20	GS+15	
Böotes I	$17.77^{+0.23}_{-0.24}$	$18.24^{+0.40}_{-0.37}$	2.95
Coma Berenices	$18.37^{+0.30}_{-0.33}$	$19.02^{+0.37}_{-0.41}$	4.47
CVn I	$17.38^{+0.11}_{-0.11}$	$17.44^{+0.37}_{-0.28}$	1.15
CVn II	$17.19^{+0.37}_{-0.47}$	$17.65^{+0.45}_{-0.43}$	2.88
Hercules I	$16.93^{+0.34}_{-0.39}$	$16.86^{+0.74}_{-0.68}$	0.85
Leo I	$17.70^{+0.07}_{-0.08}$	$17.84^{+0.20}_{-0.16}$	1.38
Leo II	$17.54^{+0.10}_{-0.10}$	$17.97^{+0.20}_{-0.18}$	2.69
Leo IV	$16.56^{+0.57}_{-0.66}$	$16.32^{+1.06}_{-1.69}$	0.58
Leo V	$16.58^{+0.60}_{-0.69}$	$16.37^{+0.94}_{-0.87}$	0.62
Segue I	$18.91^{+0.39}_{-0.48}$	$19.36^{+0.32}_{-0.35}$	2.82
Segue II	$17.23^{+0.58}_{-0.99}$	$16.21^{+1.06}_{-0.98}$	0.10
Sextans I	$18.05^{+0.25}_{-0.29}$	$17.92^{+0.35}_{-0.29}$	0.74
Ursa Major I	$18.19^{+0.22}_{-0.25}$	$17.87^{+0.56}_{-0.33}$	0.48
Ursa Major II	$18.79^{+0.36}_{-0.48}$	$19.42^{+0.44}_{-0.42}$	4.27
Ursa Minor	$18.47^{+0.20}_{-0.22}$	$18.95^{+0.26}_{-0.18}$	3.02

Table 5: The J-factor comparison between Ando+20 and GS+15. Columns 2 and 3 show the J-Factor values at 0.5°, Column 4 shows the ratio of GS+15 to Ando+20. Draco II and Triangulum II are not included here due to their absence in (Geringer-Sameth, Koushiappas, and Walker 2015).

constraining upper limit. The difference between the two estimations ranges from a factor of roughly 0.5 to 4.5. The cases in which Ando+20 predicts a greater J-Factor are in dSphs with lower DM densities and as a result have a small contribution to the combined analysis. Most notably the GS+15 J-Factor estimations in Segue I and Ursa Major II are 2.82 and 4.27 times greater than Ando+20. The GS+15 and Ando+20 estimations of the J-Factor of Segue I are shown in Figure 66. In both cases the bands are the 68% containment fraction produced from 10000 different J-Factor realisations. As these are the two largest J-Factors and the largest VERITAS exposures, it has a significant effect on the upper limits measured in this work.

7.3 Extended-Source Analysis

For the extended source analysis moderate ITM cuts are once again used, but unlike the point source analysis an angular cut of 0.2° is used (See Section 4.8 for details

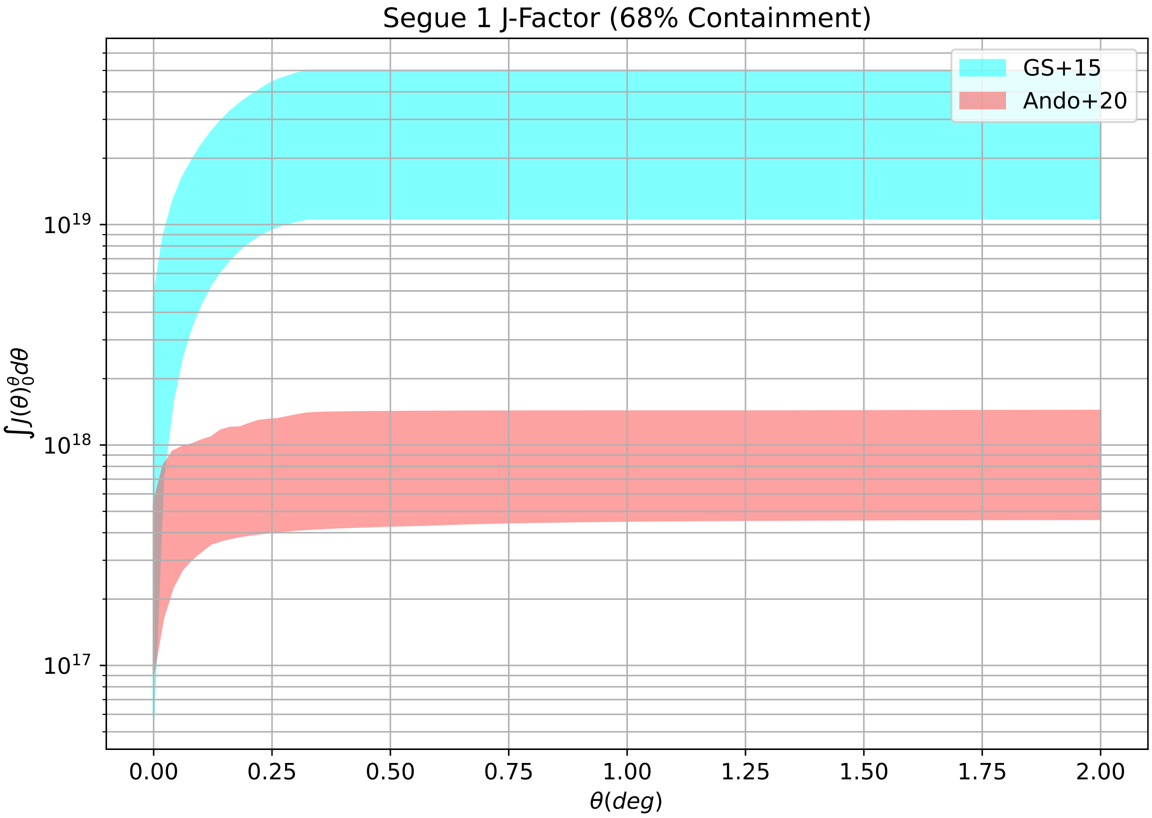

Figure 66: 68% containment of 10000 realisations of Segue I's J-Factor according to GS+15 (blue) and Ando+20 (red). The approximately order-of-magnitude difference between the two results in an approximately order-of-magnitude increase in the value of upper limits placed on the annihilation cross section.

Dwarf	Exposure [hours]	N_{ON} [counts]	N_{OFF} [counts]	α	Significance [σ]
Coma Berenices	22.6	1237	1229	1	0.2
CVn I	8.46	344	1116	0.5	-0.5
CVn II	5.43	220	601	0.5	0.5
Draco II	3.56	122	157	0.5	0.6
Hercules I	9.02	346	1092	0.5	-2.3
Leo I	5.0	229	725	0.25	1.1
Leo II	11.31	589	1339	0.33	0.5
Leo IV	0.48	23	90	0.33	-1.2
Leo V	0.47	22	39	0.5	0.4
Segue I	51.82	2914	5304	0.5	-2.4
Segue II	11.88	795	3386	0.25	-1.6
Sextans I	7.45	329	1580	0.2	0.7
Triangulum II	27.47	1291	6255	0.2	1.0
Ursa Major I	6.34	291	1284	0.2	1.9
Ursa Major II	175.20	7352	16115	0.33	-0.3
Ursa Minor	110.16	3858	7202	0.5	-0.5

Table 6: Results of the VERITAS extended analysis of 16 dSphs. The second and third columns give the counts of gamma-like events in the *ON* and *OFF* regions. The detection significance is given in the fourth column in terms of standard deviations above the background. The final column is the background normalisation factor, note that every value in this column is a unit fraction as the number of background regions in each analysis must remain constant.

on why this angular cut was chosen). Table 6 shows the results of the standard VERITAS extended source analysis where the columns are the same as those in Table 3. The change in the values of α is caused by the increase in angular cut. As the sizes of the *ON* and *OFF* regions grows *OFF* regions will begin to overlap and must then be omitted. This can also lead to a reduction in exposure time as data with no *OFF* regions cannot be used. There is once again no significant signal above the background from any dSph. Böotes I is omitted from the extended-source analysis as all Böotes I data are taken prior to VERITAS's V6 epoch so no extended-source IRFs are available. Figure 67 shows the significance distribution and cumulative significance of the extended-source analysis. Once again there is no indication of the presence of a gamma-ray source with a maximum significance of $\sim$

2.2 σ being achieved.

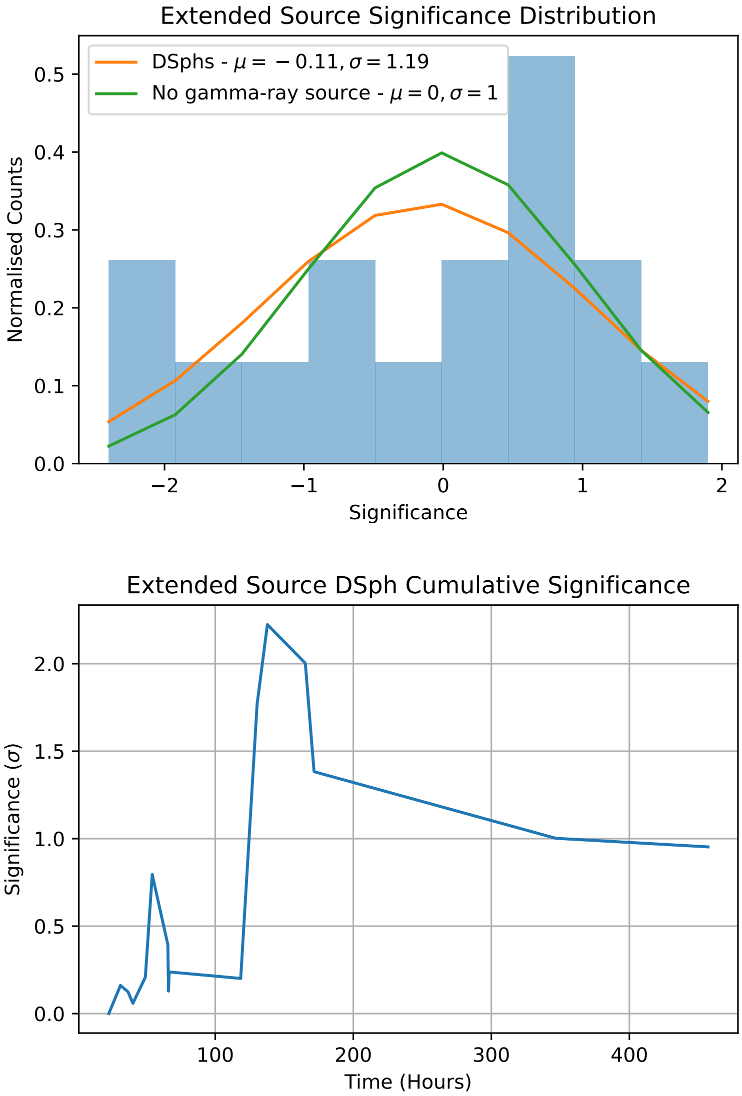

Figure 67: The significance distribution of the 16 extended-source analyses(top) the orange curve is a normal distribution fitted to the distribution, the green curve shows the expected distribution of a field with no gamma-ray sources. There is no indication of a gamma-ray excess from the significance distribution. The cumulative significance (bottom) also shows no indication of a gamma-ray excess.

dSph	e^+e^-	$\mu^+\mu^-$	$\tau^+\tau^-$	$t\bar{t}$	$b\bar{b}$	W^+W^-	ZZ	$\gamma\gamma$	$\nu_e\bar{\nu}_e$
Coma Berenices	0.21	0.15	0.05	0.06	0.07	0.05	0.05	0.06	0.6
CVn I	0	0	0	0	0	0	0	0	0
CVn II	2.31	2.29	1.96	2.10	2.21	1.99	2.10	1.93	1.50
Draco II	1.4	1.42	0.12	0.3	0.51	0	0.85	2.71	0
Hercules I	0	0	0	0	0	0	0	0	0
Leo I	0.81	0.79	0.1	0.14	0.15	0.41	0.21	0.68	0.21
Leo II	1.81	1.8	2.07	2.16	2.13	2.06	2.16	2.58	2
Leo IV	0	0	0	0	0	0	0	0.25	0
Leo V	0.87	0.85	0.89	0.76	0.74	0.72	0.72	1.65	0.73
Segue I	0	0	0	0	0	0	0	0	0
Segue II	0	0	0	0	0	0	0	0	0
Sextans I	0.78	0.81	1.13	0.62	0.75	0.85	0.78	1.17	0.65
Triangulum II	0.69	0.71	0.56	0.22	0.36	0.58	0.31	0	0.91
Ursa Major I	1.9	1.9	1.83	1.77	1.65	2.24	1.63	1.82	2.2
Ursa Major II	1.54	1.39	0	0	0	0	0	1.24	0
Ursa Minor	0.9	0.794	0.02	0.02	0.02	0.02	0.03	0	0

Table 7: The peak significance of signal from the extended-source analysis of each dSph in each annihilation channel.

7.3.1 Dark Matter Upper Limits

The results for the extended source analysis presented below follow the same structure as Section 7.1.1. There is once again no evidence for the presence of DM annihilation signals from dSph, the significance from each dSph in each channel is shown in Table 7.

Each panel in Figure 68 shows the upper limits from each annihilation channel for a given dSph with the combined analysis shown in black.

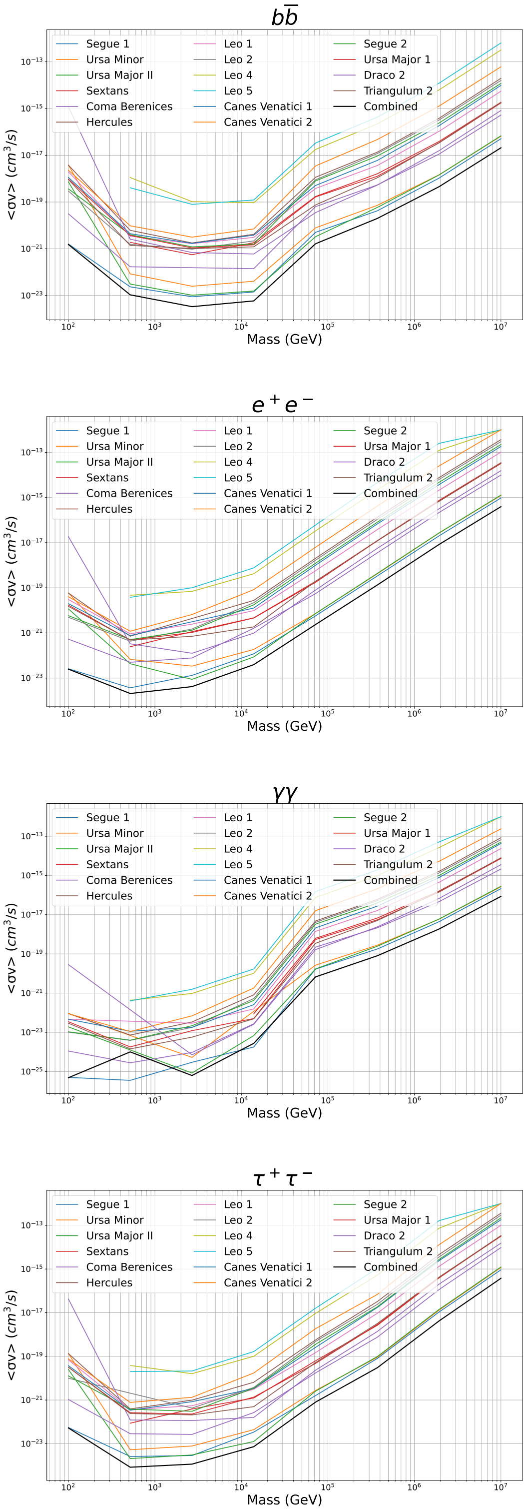

Figure 68: The 95% upper limit on the DM annihilation cross section for each of the 16 dSphs (extended source). Each panel shows the results of each dSph in a given annihilation channel (The remaining channels are shown in the appendix of this thesis).

The expected limits from the joint analysis of each annihilation channel is presented in Figure 69 and a comparison between this analysis and other indirect DM searches is shown in Figure 70.

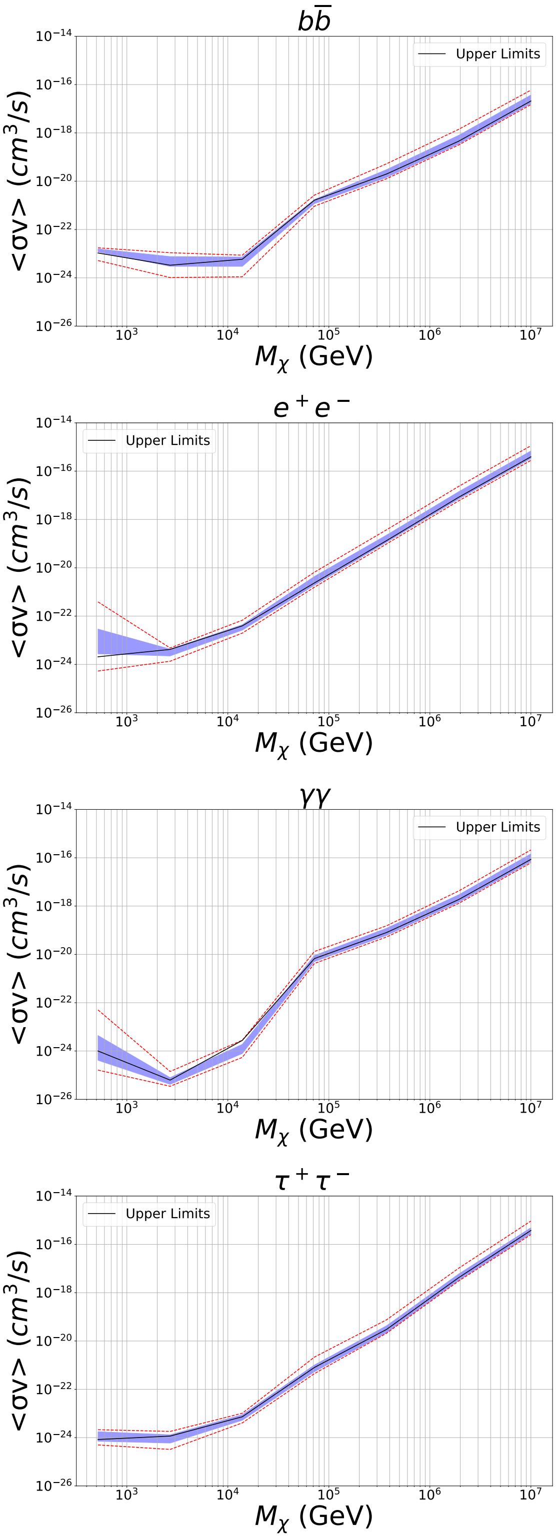

Figure 69: 68% (blue bands) and 95% (dashed red) expected limits for DM annihilation cross section for each of the 16 dSphs (extended source). Bands are generated from 50 random realisations of the signal and background. Once again the remaining channels are shown in the appendix of this thesis.

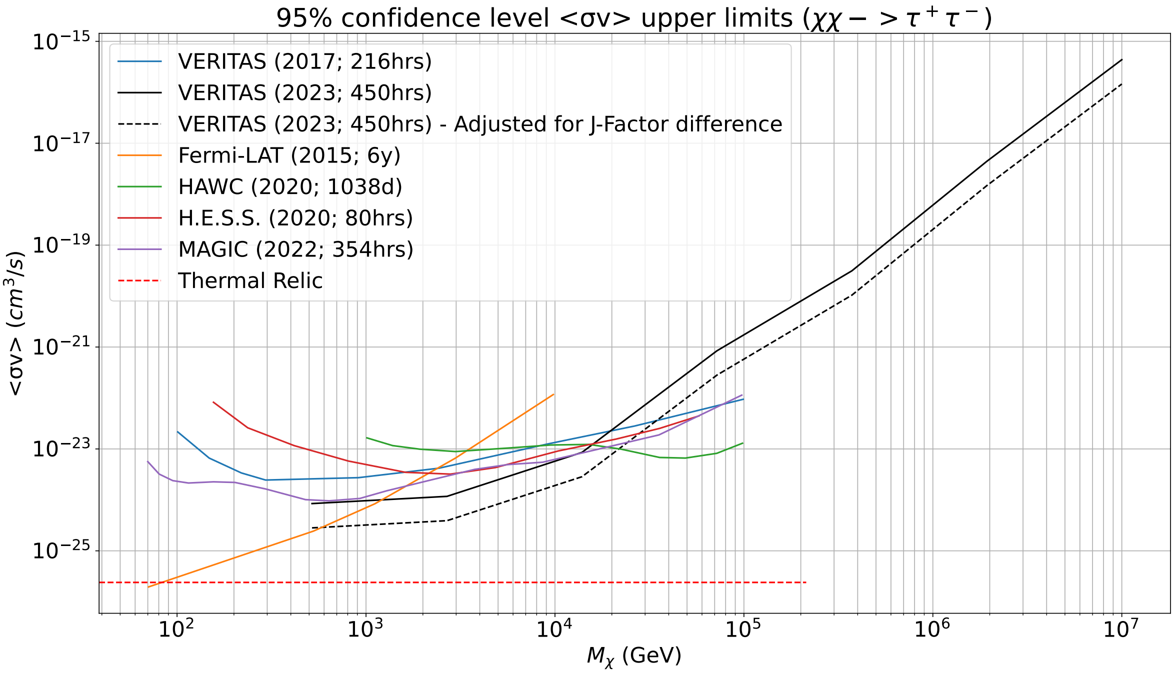

Figure 70: VERITAS upper limit curves obtained from 16 extended dSphs compared with other published upper limit curves (black solid and black dashed). All other curves are the same as those shown in Figure 64

Once again the results from this analysis set the only upper limits in the UHDM mass range. Below the UHDM mass range and in VERITAS's most sensitive mass range ($\sim 1 - 100$ TeV) this analysis places the most constraining limits on the thermally averaged annihilation cross-section of WIMP DM by an indirect search despite the use of the smaller physically motivated J-Factors presented by Ando+20. Once again the thermal relic cross section is not reached so the WIMP DM model remains valid. In order to reach the thermal relic cross section the VERITAS data set would have to grow by a factor of ~ 50. Once again an upper limit on the radius of UHDM particles can be found from the results of the combined extended-source analysis shown in Figure 71. This shows that below a DM mass of 10 PeV, DM particles with a radius greater than ~ 2 fm can be rejected in all channels.

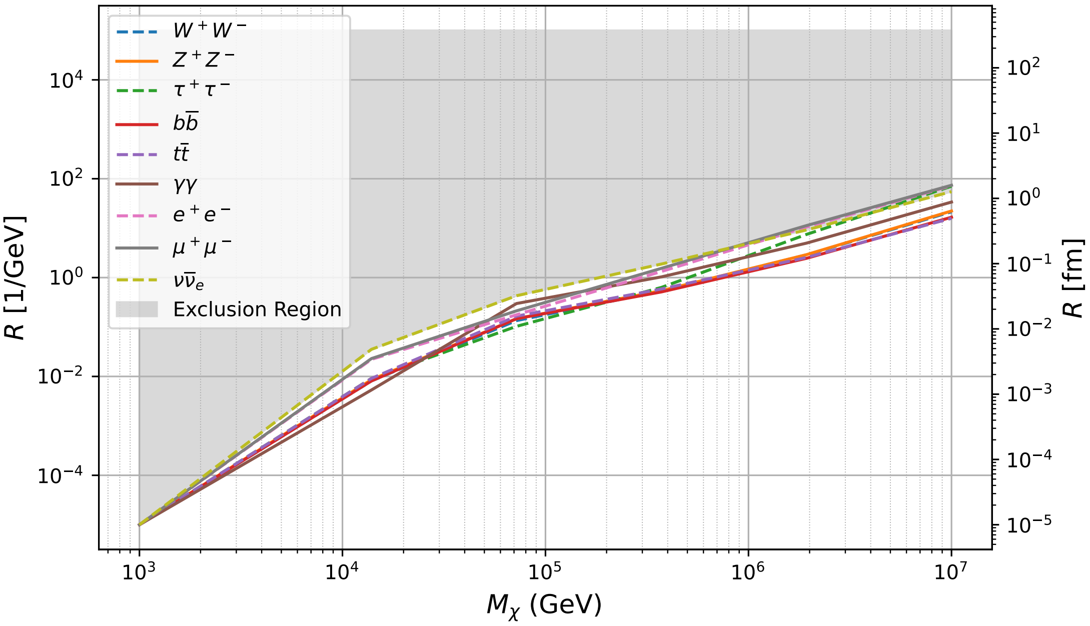

Figure 71: 95% confidence upper limits curves on the radius (femtometers) and 1/E, of a UHDM particle from the combined extended-source analysis. The nine annihilation channels considered are all shown. The shaded areas show exclusion regions set by this analysis.

Dwarf	Point Source	Extended Source
Bootes I	1.48e+17	4.26e+17
Coma Berenices	5.9e+17	1.67e+18
CVn I	8.54e+16	1.91e+17
CVn II	5.94e+16	1.28e+17
Draco II	2.99e+18	9.25e+18
Hercules I	3.35e+16	7.21e+16
Leo I	1.68e+17	3.98e+17
Leo II	1.24e+17	2.79e+17
Leo IV	1.63e+16	3.36e+16
Leo V	1.49e+16	3.06e+16
Segue I	1.53e+18	4.95e+18
Segue II	5.73e+16	1.22e+17
Sextans I	2.81e+17	8.05e+17
Triangulum II	1.57e+17	3.77e+17
Ursa Major I	4.10e+17	1.10e+18
Ursa Major II	1.07e+18	3.46e+18
Ursa Minor	6.41e+17	1.98e+18

Table 8: Median J-Factor values used in the point-source analysis (0.07°) and extended-source analysis (0.2°)

7.4 Point-Source vs Extended-Source Analysis

The motivation behind an extended-source analysis is to increase the J-Factor of each dSph (A comparison between the point and extended J-Factors used in this thesis are shown in Table 8). This increase comes at the sacrifice of background statistics as can be seen in Tables 3 and 6. Figure 72 shows the combined upper limits in a single annihilation channel from the point-source and extended-source analysis. The limits placed by the extended-source analysis are on average ~ 3 times more constraining (which is approximately proportional to the differences in J-Factors) than those placed by the point-source analysis. This shows that an extended-source analysis is a more constraining method and an improvement on the point-source analysis. The use of an extended-source analysis also provides more constraining upper limits on the radius of a composite DM particle by a factor of ~ 1.6.

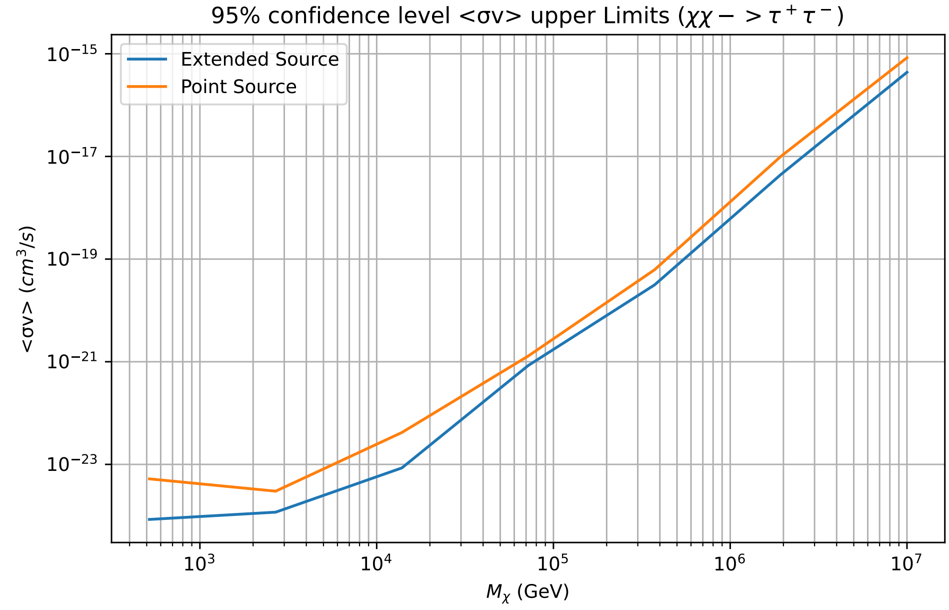

Figure 72: VERITAS upper limit curves ($\chi\chi \to \tau^+\tau^-$) obtained from 16 extended dSphs (blue) and the upper limits obtained from 17 point dSphs (orange).

8 Conclusion and Future Prospects

The aim of this research was to perform an indirect DM search in dSph with the entire VERITAS data set. As dSphs are not believed to be a source of gamma rays from other astrophysical processes, a statistically significant detection of any dSph could be considered a sign of a detection of DM annihilation. Alongside this, constraints were placed on the DM thermally averaged cross-section through the use of a MLE (even the case of no statistically significant detection of any dSph). This research includes the use of the complete VERITAS dSph data set (630 hours from 17 dSphs), improved analysis techniques (ITM), extends to the previously only once-probed ultra-heavy DM mass range ($M_{DM} > 100$ TeV), more physically motivated J-Factors (Ando+20) and the largest angular cuts applied to dSphs to date (0.2°).

In order to perform the point source analysis with the use of an ITM, new methods of deriving the VERITAS PSF were required. In the absence of the simulations used in IRF production a data-derived (Crab) PSF was first produced and used in preliminary analyses. Following the production of the VERITAS simulations a simulated PSF was derived and validated against the data-derived PSF. After finding no statistically significant excess from any dSph, upper limits could be placed on the thermally averaged annihilation cross-section of WIMP DM with the use of up-to-date physically motivated J-Factors. This search was also extended to the UHDM mass range to give some of the first upper limits on DM annihilation above $M_{DM} \approx 100$ TeV by an indirect DM search.

As dSph J-Factors are angularly extended well beyond the standard VERITAS point-source extension an extended-source analysis contains a greater amount of the galaxy's DM halo. This results in a larger J-Factor which will in turn produce more constraining upper limits on the annihilation cross-section. A study to measure the largest angular cut achievable with VERITAS found that each dSph could be analysed out to 0.2°. This allowed for a larger J-Factor compared to the point-source analysis at the sacrifice of background statistics. Once again there was no statistically significant detection of an excess from any dSph. Upper limits were once again placed on the thermally averaged cross-section up to the UHDM mass range.

8.1 Point-Source Analysis

The upper limits found from the point source analysis are consistent with the up-to-date results from other indirect searches despite using smaller, physically motivated J-Factors. If the difference in J-Factors is accounted for these are the most constraining limits from any indirect search in the $\sim 100 - 1000$ GeV DM mass range. The extended search places even more constraining limits on the annihilation cross-section where it places the most constraining upper limits in the $\sim 100 - 1000$ GeV DM mass range with the more constraining Ando+20 J-Factors. In both cases the upper limits measured are larger than the predicted thermal relic cross-section and therefore the WIMP model can not be ruled out. In order for a VERITAS point-source analysis to achieve upper limits constraining enough to reach the predicted thermal relic cross-section a data set $\sim$ 100 times larger ($\sim$ 60000 hours) would be required. Not only is gathering a data set this large impossible for an instrument with the duty cycle and range of targets of VERITAS, but a data set of that size will have a large degree of systematic errors and therefore a different approach or instrument would be required. For example these results could be further improved through advancements in instrument sensitivity, this could come in the form of improved gamma-hadron separation techniques such as using machine learning techniques to improve gamma ray identification (Oie et al. 2023). As with any IACT analysis, the improvement of instrument sensitivity will also have a great impact on the results produced. Figure 73 shows the sensitivity of current and future gamma-ray experiments where CTA will be the most sensitive instrument in the $10^{-2} - 10^{1}$ TeV energy range. With this sensitivity CTA predict that through a point-source analysis with a dSph data set equivalent in size to the one used in this analysis upper limits on the thermally averaged cross section can be further constrained by roughly a factor of 10 (Saturni 2023).

While Figure 73 shows that CTA is the most promising experiment in the standard DM mass range. Instruments such as SWGO and LHAASO will have the ability to further the search to higher masses than shown in this thesis with the best sensitivity in the UHDM mass range. As these are also some of the first results presented in the UHDM mass range by an indirect DM search and as such there

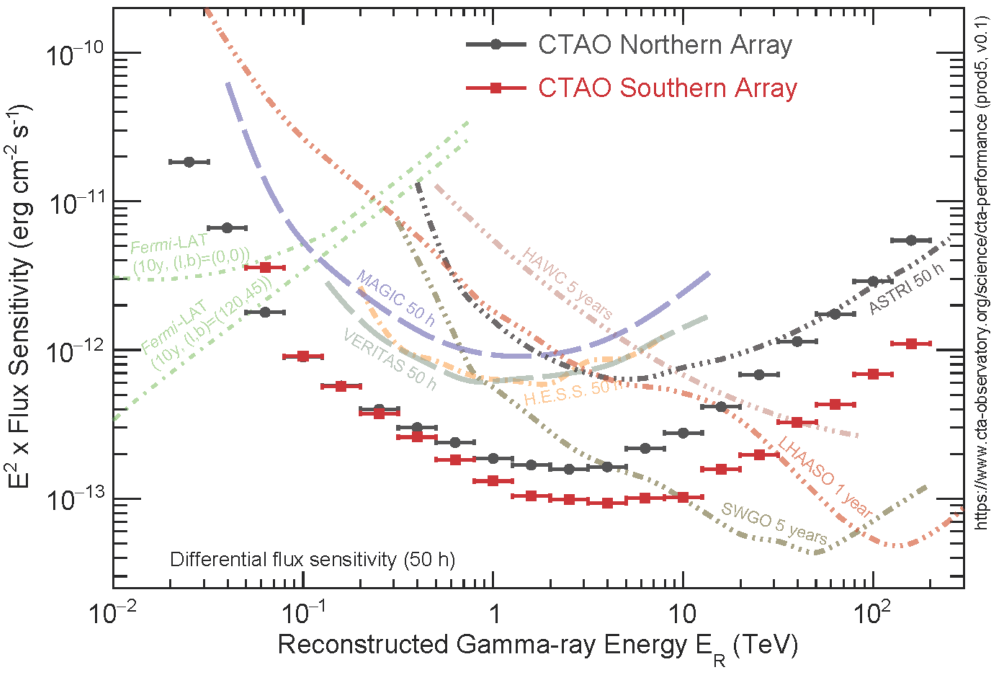

Figure 73: Differential flux sensitivity of current and future gamma-ray observatories. Image : CTA performance website[7].

remains a large potential for further studies in the area, for example LHAASO has placed constraints on the decay lifetime of UHDM (LHAASO Collaboration et al. 2022). But with these early results, limits have been placed on both the annihilation cross section up to a DM mass of 10 PeV and on the radius of composite DM particles. The measure of the statistical uncertainties in this analysis are also measured though randomised realisations of signal and background events which show that the presented results are consistent with the null hypothesis. Statistical approaches and predictions can also be used to improve background estimation, this can become particularly useful when searching for DM in the ultra-heavy mass range as the number of *OFF* events may not be enough to get an appropriate statistics for an MLE analysis. The background estimation could potentially be performed by way of extrapolation. Finally despite all results discussed in this thesis focusing on the annihilation cross section of WIMP DM in 9 different channels, all analyses could be extended to include DM decay or further decay anor annihilation channels such as the Higgs or Wino channels.

8.2 Extended-Source Analysis

While results from the extended source analysis are presented in this thesis, a detailed optimisation study to find the optimum extensions for each individual dSph could also lead to more constraining upper limits. For example Fermi-LAT show how an extended-source analysis can improve detection significance and lead to more constraining cross-section upper limits (Di Mauro, Stref, and Calore 2020). Improvements in the IACT extended-source analysis such as optimised IRFs or different background estimation methods could also lead to more constraining limits. An extended-source analysis is not only beneficial to indirect DM searches in dSphs, but should be considered for indirect DM searchers in all targets. For example unidentified Fermi-LAT Objects (Hoof, Geringer-Sameth, and Trotta 2020) which despite appearing as point-like sources to Fermi-LAT could host an extended DM Halo. Past studies by VERITAS have also shown through the use of simulations that if a DM signal does exist an indirect DM search will be benefited by an extended-

---

[7] https://www.cta-observatory.org/science/ctao-performance

source analysis (Giuri and VERITAS Collaboration 2022). This is achieved by the addition of a θ term in the MLM analysis making a 2 dimensional DM search. As this thesis has shown the benefits and possibility of an extended-source analysis of dSphs with VERITAS the application of the 2D DM analysis to an extended dSph data set is the next step in improving results of an indirect DM search. Along side this a dedicated study into the optimisation of the extended-source analysis prior to this will add to this improvement.

8.3 Targets

Through the use of N-body simulations the Aquarius Project predicts there could be up to $\sim$ 150 dSphs in the MW halo (Springel et al. 2008) meaning only about half of the dSphs have been discovered to date. Future experiments such as the Vera C. Rubin Observatory (Ivezić et al. 2019) can potentially discover $\sim$ 60 new candidate dSphs. Projections of CTA and Fermi-LAT measured cross section upper limits with only dSphs that might be found by the Vera C. Rubin Observatory predict further constraints than those presented in this thesis (Ando et al. 2019). Further studies on or re-evaluations of current J-Factors could both lead to better constraints on cross-section upper limits. For example the Five-hundred-meter Aperture Spherical Telescope (FAST) (Jiang et al. 2019) a radio telescope in China probe the possibility of inverse Compton emission from electrons produced in UHDM annihilation (Guo et al. 2023).

8.4 Multi-Instrument Search

Further contributions to multi-instrument indirect DM searches such as (Kerszberg et al. 2023) will lead to the most constraining DM limits from an indirect search in dSphs. These further contributions may come in the form of updated results from experiments which are already part of the campaign (Fermi-LAT, HAWC, H.E.S.S., MAGIC and VERITAS) or from new instruments such as LHAASO, CTA and SWGO. The models used in the current multi-instrument DM search include annihilation channels where the final state is neutrinos. With the addition of updated methods, results from neutrino experiments such as IceCube, ANTARES, and

KM3NeT could be merged with results from gamma-ray observatories in order to produce the first ever multi-messenger DM search.

8.5 Summary

The results presented in this thesis show the improvements made to a standard point source indirect DM search with VERITAS. These improvements stem from updated analysis methods and a larger data set. These results also show that for any further groundbreaking results to be achieved by an experiment like VERITAS improvements in sensitivity and analysis techniques are required as larger data sets are not sufficient. Instruments such as CTA will have the sensitivity to further constrain measurements of the DM cross section and the use of an extended-source analysis as shown in this thesis will contribute further to the quality of their results. It has been shown that by probing the UHDM mass range constraints can be placed on not only the DM thermally averaged cross section but also the DM lifetime and geometrical cross section of heavy DM, but as this area of research is still in its early phases, further studies and theories could lead to breakthroughs in our understanding of the nature or identity of DM.

References

Aad, G. et al. (Apr. 2013). “Search for dark matter candidates and large extra dimensions in events with a jet and missing transverse momentum with the ATLAS detector”. In: *Journal of High Energy Physics* 2013, 75, p. 75. arXiv: `1210.4491 [hep-ex]`.

Aalseth, C. E. et al. (Apr. 2011). “Results from a Search for Light-Mass Dark Matter with a p-Type Point Contact Germanium Detector”. In: 106.13, 131301, p. 131301. arXiv: `1002.4703 [astro-ph.CO]`.

Aaltonen, T. et al. (May 2012). “Search for Dark Matter in Events with One Jet and Missing Transverse Energy in pp Collisions at s=1.96TeV”. In: 108.21, 211804, p. 211804. arXiv: `1203.0742 [hep-ex]`.

Aartsen, M. G. et al. (Mar. 2017). “The IceCube Neutrino Observatory: instrumentation and online systems”. In: *Journal of Instrumentation* 12.3, P03012. arXiv: `1612.05093 [astro-ph.IM]`.

Abbott, L. F. and P. Sikivie (Jan. 1983). “A cosmological bound on the invisible axion”. In: *Physics Letters B* 120.1-3, pp. 133–136.

Abdalla, H. et al. (Nov. 2018). “Searches for gamma-ray lines and ’pure WIMP’ spectra from Dark Matter annihilations in dwarf galaxies with H.E.S.S.” In: 2018.11, 037, p. 037. arXiv: `1810.00995 [astro-ph.HE]`.

Abdalla, H. et al. (Sept. 2022). “Search for Dark Matter Annihilation Signals in the H.E.S.S. Inner Galaxy Survey”. In: 129.11, 111101, p. 111101. arXiv: `2207.10471 [astro-ph.HE]`.

Acciari, V. A. et al. (Mar. 2022). “Combined searches for dark matter in dwarf spheroidal galaxies observed with the MAGIC telescopes, including new data from Coma Berenices and Draco”. In: *Physics of the Dark Universe* 35, 100912, p. 100912. arXiv: `2111.15009 [astro-ph.HE]`.

Acharya, B.S. et al. (2013). “Introducing the CTA concept”. In: *Astroparticle Physics* 43. Seeing the High-Energy Universe with the Cherenkov Telescope Array - The Science Explored with the CTA, pp. 3–18. ISSN: 0927-6505.

Acharyya, A. et al. (Sept. 2023). “Multiwavelength Observations of the Blazar PKS 0735+178 in Spatial and Temporal Coincidence with an Astrophysical Neutrino Candidate IceCube-211208A”. In: 954.1, 70, p. 70. arXiv: `2306.17819 [astro-ph.HE]`.

Ackermann, M. et al. (Mar. 2013). “Determination of the Point-spread Function for the Fermi Large Area Telescope from On-orbit Data and Limits on Pair Halos of Active Galactic Nuclei”. In: 765.1, 54, p. 54. arXiv: `1309.5416 [astro-ph.HE]`.

Adams, C. B. et al. (Sept. 2021). “An Archival Search for Neutron-star Mergers in Gravitational Waves and Very-high-energy Gamma Rays”. In: 918.2, 66, p. 66. arXiv: `2106.01386 [astro-ph.HE]`.

Adams, C. B. et al. (Feb. 2022). “The throughput calibration of the VERITAS telescopes”. In: 658, A83, A83. arXiv: `2111.04676 [astro-ph.IM]`.

Agnes, P. et al. (Nov. 2018). “DarkSide-50 532-day dark matter search with low-radioactivity argon”. In: 98.10, 102006, p. 102006. arXiv: `1802.07198 [astro-ph.CO]`.

Aharonian, F.A., W. Hofmann, A.K. Konopelko, and H.J. Völk (1997). “The potential of ground based arrays of imaging atmospheric Cherenkov telescopes. I. Determination of shower parameters”. In: *Astroparticle Physics* 6.3, pp. 343–368. ISSN: 0927-6505.

Ahmed, Z. et al. (Apr. 2011). “Results from a Low-Energy Analysis of the CDMS II Germanium Data”. In: 106.13, 131302, p. 131302. arXiv: `1011.2482 [astro-ph.CO]`.

Albert, A. et al. (Feb. 2018). “Dark Matter Limits from Dwarf Spheroidal Galaxies with the HAWC Gamma-Ray Observatory”. In: 853.2, 154, p. 154. arXiv: `1706.01277 [astro-ph.HE]`.

Albert, J. et al. (Feb. 2008). “VHE γ-Ray Observation of the Crab Nebula and its Pulsar with the MAGIC Telescope”. In: 674.2, pp. 1037–1055. arXiv: `0705.3244 [astro-ph]`.

Amruth, Alfred et al. (June 2023). “Einstein rings modulated by wavelike dark matter from anomalies in gravitationally lensed images”. In: *Nature Astronomy* 7, pp. 736–747. arXiv: `2304.09895 [astro-ph.CO]`.

Ando, Shin’ichiro et al. (2019). “Discovery prospects of dwarf spheroidal galaxies for indirect dark matter searches”. In: *Journal of Cosmology and Astroparticle Physics* 2019.10, p. 040.

Ando, Shin’ichiro, Alex Geringer-Sameth, Nagisa Hiroshima, Sebastian Hoof, Roberto Trotta, and Matthew G. Walker (Sept. 2020). “Structure formation models weaken limits on WIMP dark matter from dwarf spheroidal galaxies”. In: 102.6, 061302, p. 061302. arXiv: `2002.11956 [astro-ph.CO]`.

Aprile, E. et al. (Apr. 2011). “Design and performance of the XENON10 dark matter experiment”. In: *Astroparticle Physics* 34.9, pp. 679–698. arXiv: `1001.2834 [astro-ph.IM]`.

Aprile, E. et al. (Nov. 2012). “Dark Matter Results from 225 Live Days of XENON100 Data”. In: 109.18, 181301, p. 181301. arXiv: `1207.5988 [astro-ph.CO]`.

Aprile, E. et al. (Apr. 2016). “Physics reach of the XENON1T dark matter experiment.” In: 2016.4, 027, p. 027. arXiv: `1512.07501 [physics.ins-det]`.

Aprile, E. et al. (Nov. 2020). “Projected WIMP sensitivity of the XENONnT dark matter experiment”. In: 2020.11, 031, p. 031. arXiv: `2007.08796 [physics.ins-det]`.

Archambault, S. et al. (Apr. 2017). “Dark matter constraints from a joint analysis of dwarf Spheroidal galaxy observations with VERITAS”. In: 95.8, 082001, p. 082001. arXiv: `1703.04937 [astro-ph.HE]`.

Bauer, Christian W., Nicholas L. Rodd, and Bryan R. Webber (June 2021). “Dark matter spectra from the electroweak to the Planck scale”. In: *Journal of High Energy Physics* 2021.6, 121, p. 121. arXiv: `2007.15001 [hep-ph]`.

Begeman, K. G. (Oct. 1989). “HI rotation curves of spiral galaxies. I. NGC 3198.” In: 223, pp. 47–60.

Begeman, K. G., A. H. Broeils, and R. H. Sanders (1991). “Extended rotation curves of spiral galaxies: Dark haloes and modified dynamics”. In: *Mon. Not. Roy. Astron. Soc.* 249, p. 523.

Bennett, D. P. et al. (Jan. 1996a). “The MACHO Project Dark Matter Search”. In: *Clusters, Lensing, and the Future of the Universe*. Ed. by Virginia Trimble and Andreas Reisenegger. Vol. 88. Astronomical Society of the Pacific Conference Series, p. 95. arXiv: `astro-ph/9510104 [astro-ph]`.

— (Jan. 1996b). “The MACHO Project Dark Matter Search”. In: *Clusters, Lensing, and the Future of the Universe*. Ed. by Virginia Trimble and Andreas Reisenegger. Vol. 88. Astronomical Society of the Pacific Conference Series, p. 95. arXiv: `astro-ph/9510104 [astro-ph]`.

Berge, D., S. Funk, and J. Hinton (May 2007). “Background modelling in very-high-energy γ-ray astronomy”. In: 466.3, pp. 1219–1229. arXiv: `astro-ph/0610959 [astro-ph]`.

Bergström, Lars (Oct. 2009). “Dark matter candidates”. In: *New Journal of Physics* 11.10, 105006, p. 105006. arXiv: `0903.4849 [hep-ph]`.

Berlin, Asher, Dan Hooper, and Gordan Krnjaic (Sept. 2016). “PeV-scale dark matter as a thermal relic of a decoupled sector”. In: *Physics Letters B* 760, pp. 106–111. arXiv: `1602.08490 [hep-ph]`.

Billard, Julien et al. (May 2022). “Direct detection of dark matter-APPEC committee report”. In: *Reports on Progress in Physics* 85.5, 056201, p. 056201. arXiv: `2104.07634 [hep-ex]`.

Brun, Rene et al. (Aug. 2019). *root-project/root: v6.18/02*. Version v6-18-02.

Bühler, R. and R. Blandford (June 2014). “The surprising Crab pulsar and its nebula: a review”. In: *Reports on Progress in Physics* 77.6, 066901, p. 066901. arXiv: `1309.7046 [astro-ph.HE]`.

Burkert, A. (July 1995). “The Structure of Dark Matter Halos in Dwarf Galaxies”. In: 447, pp. L25–L28. arXiv: astro-ph/9504041 [astro-ph].

Cannoni, Mirco (Mar. 2015). “Exact theory of freeze-out”. In: *European Physical Journal C* 75, 106, p. 106. arXiv: 1407.4108 [hep-ph].

Cawley, M. F., D. J. Regan, K. Gibbs, P. W. Gorham, R. C. Lamb, D. F. Liebing, P. K. MacKeown, N. A. Porter, V. J. Stenger, and T. C. Weekes (Aug. 1985). “Observations of the Crab Nebula at Energies ¿ 4X10**11 EV”. In: *19th International Cosmic Ray Conference (ICRC19), Volume 1*. Vol. 1. International Cosmic Ray Conference, p. 131.

“Central Limit Theorem” (2008). In: *The Concise Encyclopedia of Statistics*. New York, NY: Springer New York, pp. 66–68. ISBN: 978-0-387-32833-1.

Chatrchyan, S. et al. (Sept. 2012). “Search for dark matter and large extra dimensions in monojet events in pp collisions at sqrt {s} = {7} TeV”. In: *Journal of High Energy Physics* 2012, 94, p. 94. arXiv: 1206.5663 [hep-ex].

Christiansen, J. and VERITAS Collaboration (July 2017). “Characterization of a Maximum Likelihood Gamma-Ray Reconstruction Algorithm for VERITAS”. In: *35th International Cosmic Ray Conference (ICRC2017)*. Vol. 301. International Cosmic Ray Conference, p. 789. arXiv: 1708.05684 [astro-ph.IM].

Ciafaloni, Paolo, Denis Comelli, Antonio Riotto, Filippo Sala, Alessandro Strumia, and Alfredo Urbano (Mar. 2011). “Weak corrections are relevant for dark matter indirect detection”. In: 2011.3, 019, p. 019. arXiv: 1009.0224 [hep-ph].

Cirelli, Marco, Gennaro Corcella, Andi Hektor, Gert Hütsi, Mario Kadastik, Paolo Panci, Martti Raidal, Filippo Sala, and Alessandro Strumia (Mar. 2011). “PPPC 4 DM ID: a poor particle physicist cookbook for dark matter indirect detection”. In: 2011.3, 051, p. 051. arXiv: 1012.4515 [hep-ph].

Conrad, Jan (Nov. 2014). “Indirect Detection of WIMP Dark Matter: a compact review”. In: *arXiv e-prints*, arXiv:1411.1925, arXiv:1411.1925. arXiv: 1411.1925 [hep-ph].

Corcella, Gennaro, Ian G. Knowles, Giuseppe Marchesini, Stefano Moretti, Kosuke Odagiri, Peter Richardson, Michael H. Seymour, and Bryan R. Webber (Jan. 2001). "HERWIG 6: an event generator for hadron emission reactions with interfering gluons (including supersymmetric processes)". In: *Journal of High Energy Physics* 2001.1, 010, p. 010. arXiv: hep-ph/0011363 [hep-ph].

Davies, John M. and Eugene S. Cotton (1957). "Design of the quartermaster solar furnace". In: *Solar Energy* 1.2, pp. 16–22. ISSN: 0038-092X.

de Naurois, Mathieu and Loïc Rolland (Dec. 2009). "A high performance likelihood reconstruction of γ-rays for imaging atmospheric Cherenkov telescopes". In: *Astroparticle Physics* 32.5, pp. 231–252. arXiv: 0907.2610 [astro-ph.IM].

Di Mauro, Mattia, Martin Stref, and Francesca Calore (Nov. 2020). "Investigating the detection of dark matter subhalos as extended sources with Fermi-LAT". In: 102.10, 103010, p. 103010. arXiv: 2007.08535 [astro-ph.HE].

Diemand, Jürg, Ben Moore, and Joachim Stadel (Sept. 2004). "Convergence and scatter of cluster density profiles". In: 353.2, pp. 624–632. arXiv: astro-ph/0402267 [astro-ph].

Du, N. et al. (Apr. 2018). "Search for Invisible Axion Dark Matter with the Axion Dark Matter Experiment". In: 120.15, 151301, p. 151301. arXiv: 1804.05750 [hep-ex].

Essig, R. et al. (Oct. 2013). "Dark Sectors and New, Light, Weakly-Coupled Particles". In: *arXiv e-prints*, arXiv:1311.0029, arXiv:1311.0029. arXiv: 1311.0029 [hep-ph].

Fegan, David J. (Sept. 1997). "TOPICAL REVIEW: ?/hadron separation at TeV energies". In: *Journal of Physics G Nuclear Physics* 23.9, pp. 1013–1060.

Fishman, Gerald J. and Charles A. Meegan (1995). "Gamma-Ray Bursts". In: *Annual Review of Astronomy and Astrophysics* 33.1, pp. 415–458. eprint: https://doi.org/10.1146/annurev.aa.33.090195.002215.

Frank, I. M. and I. E. Tamm (1937). “Coherent visible radiation of fast electrons passing through matter”. In: *Compt. Rend. Acad. Sci. URSS* 14.3, pp. 109–114.

Friedman, A. (1922). “On the Curvature of space”. In: *Z. Phys.* 10, pp. 377–386.

Fuente, Eduardo de la, Tomas Oceguera-Becerra, Guillermo García-Torales, and José Luis García-Luna (2013). “The High Altitude Water Čerenkov (HAWC) TeV Gamma Ray Observatory”. In: *Cosmic Rays in Star-Forming Environments*. Ed. by Diego F. Torres and Olaf Reimer. Berlin, Heidelberg: Springer Berlin Heidelberg, pp. 439–446. ISBN: 978-3-642-35410-6.

Garrett, Katherine and Gintaras Dūda (Jan. 2011). “Dark Matter: A Primer”. In: *Advances in Astronomy* 2011, 968283, p. 968283. arXiv: `1006.2483 [hep-ph]`.

Geringer-Sameth, Alex, Savvas M. Koushiappas, and Matthew Walker (Mar. 2015). “Dwarf Galaxy Annihilation and Decay Emission Profiles for Dark Matter Experiments”. In: 801.2, 74, p. 74. arXiv: `1408.0002 [astro-ph.CO]`.

Giuri, C. and VERITAS Collaboration (Mar. 2022). “VERITAS dark matter search in dwarf Spheroidal galaxies: an extended source analysis”. In: *37th International Cosmic Ray Conference*, p. 515. arXiv: `2108.06083 [astro-ph.HE]`.

Goodman, Mark W. and Edward Witten (1985). “Detectability of Certain Dark Matter Candidates”. In: *Phys. Rev. D* 31. Ed. by M. A. Srednicki, p. 3059.

Griest, Kim (Jan. 1993). “The Search for the Dark Matter: WIMPs and MACHOs”. In: *Texas/PASCOS 1992: Relativistic Astrophysics and Particle Cosmology*. Ed. by Carl W. Akerlof and Mark A. Srednicki. Vol. 688, p. 390. arXiv: `hep-ph/9303253 [astro-ph]`.

Griest, Kim and David Seckel (1991). “Three exceptions in the calculation of relic abundances”. In: *Phys. Rev. D* 43 (10), pp. 3191–3203.

Guo, Wen-Qing, Yichao Li, Xiaoyuan Huang, Yin-Zhe Ma, Geoff Beck, Yogesh Chandola, and Feng Huang (May 2023). “Constraints on dark matter annihilation from the FAST observation of the Coma Berenices dwarf galaxy”. In: 107.10, 103011, p. 103011. arXiv: `2209.15590 [astro-ph.HE]`.

Häffner, S. (2014). “Studies of cosmic-ray electrons with the H.E.S.S. experiment using an advanced reconstruction technique”. In:

Hall, J., V. V. Vassiliev, D. B. Kieda, J. Moses, T. Nagai, and J. Smith (July 2003). “Veritas CFDs”. In: *International Cosmic Ray Conference*. Vol. 5. International Cosmic Ray Conference, p. 2851.

Hall, Lawrence J., Karsten Jedamzik, John March-Russell, and Stephen M. West (Mar. 2010). “Freeze-in production of FIMP dark matter”. In: *Journal of High Energy Physics* 2010, 80, p. 80. arXiv: `0911.1120 [hep-ph]`.

Hamilton, A. J. S. (Feb. 2000). “Uncorrelated modes of the non-linear power spectrum”. In: 312.2, pp. 257–284. arXiv: `astro-ph/9905191 [astro-ph]`.

Hanna, D., A. McCann, M. McCutcheon, and L. Nikkinen (Jan. 2010). “An LED-based flasher system for VERITAS”. In: *Nuclear Instruments and Methods in Physics Research A* 612.2, pp. 278–287. arXiv: `0911.2015 [astro-ph.IM]`.

Harigaya, Keisuke, Masahiro Ibe, Kunio Kaneta, Wakutaka Nakano, and Motoo Suzuki (Aug. 2016). “Thermal relic dark matter beyond the unitarity limit”. In: *Journal of High Energy Physics* 2016.8, 151, p. 151. arXiv: `1606.00159 [hep-ph]`.

Hawking, S. W. (Mar. 1974). “Black hole explosions?” In: 248.5443, pp. 30–31.

Hillas, A. M. (Aug. 1985). “Cerenkov Light Images of EAS Produced by Primary Gamma Rays and by Nuclei”. In: *19th International Cosmic Ray Conference (ICRC19), Volume 3*. Vol. 3. International Cosmic Ray Conference, p. 445.

Hinshaw, G. et al. (Feb. 2009). “Five-Year Wilkinson Microwave Anisotropy Probe Observations: Data Processing, Sky Maps, and Basic Results”. In: 180.2, pp. 225–245. arXiv: `0803.0732 [astro-ph]`.

Hinton, J. A. and HESS Collaboration (Apr. 2004). “The status of the HESS project”. In: 48.5-6, pp. 331–337. arXiv: `astro-ph/0403052 [astro-ph]`.

Holder, J. (Jan. 2005). “Exploiting VERITAS Timing Information”. In: *29th International Cosmic Ray Conference (ICRC29), Volume 5*. Vol. 5. International Cosmic Ray Conference, p. 383. arXiv: `astro-ph/0507450 [astro-ph]`.

Holder, J. et al. (Dec. 2008). “Status of the VERITAS Observatory”. In: *American Institute of Physics Conference Series*. Ed. by Felix A. Aharonian, Werner Hofmann, and Frank Rieger. Vol. 1085. American Institute of Physics Conference Series, pp. 657–660. arXiv: `0810.0474 [astro-ph]`.

Holder, Jamie (Oct. 2015). “Atmospheric Cherenkov Gamma-ray Telescopes”. In: arXiv: `1510.05675 [astro-ph.IM]`.

Hoof, Sebastian, Alex Geringer-Sameth, and Roberto Trotta (Feb. 2020). “A global analysis of dark matter signals from 27 dwarf spheroidal galaxies using 11 years of Fermi-LAT observations”. In: 2020.2, 012, p. 012. arXiv: `1812.06986 [astro-ph.CO]`.

Hubble, Edwin (Mar. 1929). “A Relation between Distance and Radial Velocity among Extra-Galactic Nebulae”. In: *Proceedings of the National Academy of Science* 15.3, pp. 168–173.

Ibarra, Alejandro, Maximilian Totzauer, and Sebastian Wild (Apr. 2014). “Higher order dark matter annihilations in the Sun and implications for IceCube”. In: 2014.4, 012, p. 012. arXiv: `1402.4375 [hep-ph]`.

Ivezić, Željko et al. (Mar. 2019). “LSST: From Science Drivers to Reference Design and Anticipated Data Products”. In: 873.2, 111, p. 111. arXiv: `0805.2366 [astro-ph]`.

Jelley, J. V. (July 1955). “SPECIAL ARTICLE: Cerenkov radiation and its applications”. In: *British Journal of Applied Physics* 6.7, pp. 227–232.

Jiang, Peng, Bo Peng, Di Li, and Renxin Xu (Mar. 2019). “The Science and Technology of FAST”. In: *arXiv e-prints*, arXiv:1903.07240, arXiv:1903.07240. arXiv: `1903.07240 [astro-ph.HE]`.

Jungman, G., M. Kamionkowski, and K. Griest (Mar. 1996). “Supersymmetric dark matter”. In: 267, pp. 195–373. arXiv: `hep-ph/9506380 [hep-ph]`.

Kamionkowski, M. (Jan. 1998). “WIMP and Axion Dark Matter”. In: *High Energy Physics and Cosmology, 1997 Summer School*. Ed. by E. Gava, A. Masiero, K. S. Narain, S. Randjbar-Daemi, G. Senjanovic, A. Smirnov, and Q. Shafi. Vol. 14, p. 394. arXiv: `hep-ph/9710467 [hep-ph]`.

Kerszberg, Daniel, Céline Armand, Eric Charles, Mattia di Mauro, Chiara Giuri, J Patrick Harding, Tjark Miener, Emmanuel Moulin, Louise Oakes, Vincent Poireau, et al. (2023). “Search for dark matter annihilation with a combined analysis of dwarf spheroidal galaxies from Fermi-LAT, HAWC, HESS, MAGIC and VERITAS”. In: *PoS* ICRC2023, p. 1426.

Kieda, D. B. (Jan. 2013). “The Gamma Ray Detection Sensitivity of the Upgraded VERITAS Observatory”. In: *International Cosmic Ray Conference*. Vol. 33. International Cosmic Ray Conference, p. 1124. arXiv: `1308.4849 [astro-ph.IM]`.

Krawczynski, H., D. A. Carter-Lewis, C. Duke, J. Holder, G. Maier, S. Le Bohec, and G. Sembroski (July 2006). “Gamma hadron separation methods for the VERITAS array of four imaging atmospheric Cherenkov telescopes”. In: *Astroparticle Physics* 25.6, pp. 380–390. arXiv: `astro-ph/0604508 [astro-ph]`.

Le Bohec, S. et al. (Oct. 1998). “A new analysis method for very high definition imaging atmospheric Cherenkov telescopes as applied to the CAT telescope.” In: *Nuclear Instruments and Methods in Physics Research A* 416.2, pp. 425–437. arXiv: `astro-ph/9804133 [astro-ph]`.

LHAASO Collaboration, S. Ando, M. Chianese, D. F. G. Fiorillo, G. Miele, and K. C. Y. Ng (Oct. 2022). “Constraints on heavy decaying dark matter from 570 days of LHAASO observations”. In: *arXiv e-prints*, arXiv:2210.15989, arXiv:2210.15989. arXiv: `2210.15989 [astro-ph.HE]`.

Li, T. P. and Y. Q. Ma (Sept. 1983). “Analysis methods for results in gamma-ray astronomy.” In: 272, pp. 317–324.

Ma, Xin-Hua et al. (2022). “Chapter 1 LHAASO Instruments and Detector technology *”. In: *Chinese Physics C* 46.3, p. 030001.

Marrodán Undagoitia, Teresa and Ludwig Rauch (Jan. 2016). “Dark matter direct-detection experiments”. In: *Journal of Physics G Nuclear Physics* 43.1, 013001, p. 013001. arXiv: `1509.08767 [physics.ins-det]`.

Marsh, David J. E. (July 2016). “Axion cosmology”. In: 643, pp. 1–79. arXiv: `1510.07633 [astro-ph.CO]`.

Martinez, Gregory D., James S. Bullock, Manoj Kaplinghat, Louis E. Strigari, and Roberto Trotta (June 2009). “Indirect Dark Matter detection from Dwarf satellites: joint expectations from astrophysics and supersymmetry”. In: 2009.6, 014, p. 014. arXiv: `0902.4715 [astro-ph.HE]`.

Martinez, Gregory D., Quinn E. Minor, James Bullock, Manoj Kaplinghat, Joshua D. Simon, and Marla Geha (2011). “A complete spectroscopic survey of the Milky Way satellite Segue 1: dark matter content, stellar membership, and binary properties from a Bayesian analysis”. In: *The Astrophysical Journal* 738.1, p. 55.

Mateo, Mario L. (Jan. 1998). “Dwarf Galaxies of the Local Group”. In: 36, pp. 435–506. arXiv: `astro-ph/9810070 [astro-ph]`.

McCann, A., D. Hanna, J. Kildea, and M. McCutcheon (Jan. 2010). “A new mirror alignment system for the VERITAS telescopes”. In: *Astroparticle Physics* 32.6, pp. 325–329. arXiv: `0910.3277 [astro-ph.IM]`.

McKinsey, D N et al. (2010). “The LUX dark matter search”. In: *Journal of Physics: Conference Series* 203.1, p. 012026.

Merritt, David, Alister W. Graham, Ben Moore, Jürg Diemand, and Balša Terzić (Dec. 2006). “Empirical Models for Dark Matter Halos. I. Nonparametric Construction of Density Profiles and Comparison with Parametric Models”. In: 132.6, pp. 2685–2700. arXiv: `astro-ph/0509417 [astro-ph]`.

Milgrom, M. (July 1983). “A modification of the Newtonian dynamics as a possible alternative to the hidden mass hypothesis.” In: 270, pp. 365–370.

Mohanty, G., S. Biller, D.A. Carter-Lewis, D.J. Fegan, A.M. Hillas, R.C. Lamb, T.C. Weekes, M. West, and J. Zweerink (1998). “Measurement of TeV gamma-ray spectra with the Cherenkov imaging technique". In: *Astroparticle Physics* 9.1, pp. 15–43. ISSN: 0927-6505.

Moiseev, A. A., R. C. Hartman, J. F. Ormes, D. J. Thompson, M. J. Amato, T. E. Johnson, K. N. Segal, and D. A. Sheppard (June 2007). "The anti-coincidence detector for the GLAST large area telescope". In: *Astroparticle Physics* 27.5, pp. 339–358. arXiv: `astro-ph/0702581 [astro-ph]`.

Murayama, H., G. G. Raffelt, C. Hagmann, K. van Bibber, and L. J. Rosenberg (1998). "Axions and other very light bosons: in Review of Particle Physics (RPP 1998)". In: *Eur. Phys. J. C* 3, pp. 264–271.

Natarajan, Priyamvada et al. (June 2017). "Mapping substructure in the HST Frontier Fields cluster lenses and in cosmological simulations". In: 468.2, pp. 1962–1980. arXiv: `1702.04348 [astro-ph.GA]`.

Navarro, Julio F., Carlos S. Frenk, and Simon D. M. White (May 1996). "The Structure of Cold Dark Matter Halos". In: 462, p. 563. arXiv: `astro-ph/9508025 [astro-ph]`.

Navarro, Julio F., Aaron Ludlow, Volker Springel, Jie Wang, Mark Vogelsberger, Simon D. M. White, Adrian Jenkins, Carlos S. Frenk, and Amina Helmi (Feb. 2010). "The diversity and similarity of simulated cold dark matter haloes". In: 402.1, pp. 21–34. arXiv: `0810.1522 [astro-ph]`.

Netzer, Hagai (Aug. 2015). "Revisiting the Unified Model of Active Galactic Nuclei". In: 53, pp. 365–408. arXiv: `1505.00811 [astro-ph.GA]`.

Newville, Matthew, Till Stensitzki, Daniel B. Allen, and Antonino Ingargiola (Sept. 2014). *LMFIT: Non-Linear Least-Square Minimization and Curve-Fitting for Python*. Version 0.8.0.

Oie, Grant, Lucy Fortson, Ramana Sankar, Kameswara Mantha, and Deivid Ribeiro (2023). "Application of Long Short-Term Memory (LSTM) Deep Learning Networks on Very-High-Energy Gamma-Ray Classification with VERITAS". In: *PoS* ICRC2023, p. 692.

Pace, Andrew B. and Louis E. Strigari (Jan. 2019). "Scaling relations for dark matter annihilation and decay profiles in dwarf spheroidal galaxies". In: 482.3, pp. 3480–3496. arXiv: `1802.06811 [astro-ph.GA]`.

Park, Nahee (2016). "Performance of the VERITAS experiment". In: *PoS* ICRC2015, p. 771. arXiv: `1508.07070 [astro-ph.IM]`.

Parsons, R. D. and J. A. Hinton (Apr. 2014). "A Monte Carlo template based analysis for air-Cherenkov arrays". In: *Astroparticle Physics* 56, pp. 26–34. arXiv: `1403.2993 [astro-ph.IM]`.

Peccei, R. D. and Helen R. Quinn (June 1977). "CP conservation in the presence of pseudoparticles". In: 38.25, pp. 1440–1443.

Penzias, A. A. and R. W. Wilson (July 1965). "A Measurement of Excess Antenna Temperature at 4080 Mc/s." In: 142, pp. 419–421.

Perkins, Jeremy S., G. Maier, and VERITAS Collaboration (Mar. 2010). "VERITAS Telescope 1 Relocation: Details and Improvements". In: *AAS/High Energy Astrophysics Division #11*. Vol. 11. AAS/High Energy Astrophysics Division, p. 39.04.

Punch, M. et al. (Aug. 1992). "Detection of TeV photons from the active galaxy Markarian 421". In: 358.6386, pp. 477–478.

Quinn, J. et al. (1996). "Detection of Gamma Rays with E gt; 300 GeV from Markarian 501". In: *The Astrophysical Journal* 456.2, p. L83.

Read, A. M., S. R. Rosen, R. D. Saxton, and J. Ramirez (Oct. 2011). "A new comprehensive 2D model of the point spread functions of the XMM-Newton EPIC telescopes: spurious source suppression and improved positional accuracy". In: 534, A34, A34. arXiv: `1108.4835 [astro-ph.IM]`.

Rebillot, P. F., J. H. Buckley, P. Dowkontt, and K. Kosack (July 2003). "The VERITAS Flash ADC Electronics System". In: *International Cosmic Ray Conference*. Vol. 5. International Cosmic Ray Conference, p. 2827.

Riess, Adam G. et al. (Sept. 1998). “Observational Evidence from Supernovae for an Accelerating Universe and a Cosmological Constant”. In: 116.3, pp. 1009–1038. arXiv: `astro-ph/9805201 [astro-ph]`.

Roache, E., R. Irvin, J. S. Perkins, K. Harris, A. Falcone, J. Finley, and T. Weeks (Jan. 2008). “Mirror Facets for the VERITAS Telescopes”. In: *International Cosmic Ray Conference*. Vol. 3. International Cosmic Ray Conference, pp. 1397–1400.

Rolke, Wolfgang A., Angel M. López, and Jan Conrad (Oct. 2005). “Limits and confidence intervals in the presence of nuisance parameters”. In: *Nuclear Instruments and Methods in Physics Research A* 551.2-3, pp. 493–503. arXiv: `physics/0403059 [physics.data-an]`.

Rubin, V. C. (June 1983). “Dark matter in spiral galaxies”. In: *Scientific American* 248, pp. 96–106.

Rubin, Vera C. and Jr. Ford W. Kent (Feb. 1970). “Rotation of the Andromeda Nebula from a Spectroscopic Survey of Emission Regions”. In: 159, p. 379.

Russell, J. L. (1964). “Kepler’s Laws of Planetary Motion: 1609–1666”. In: *The British Journal for the History of Science* 2.1, 1–24.

Ryan, James L. (2023). “Search for Dark Matter Annihilation Signals in the Galactic Center Halo with VERITAS”. In: *PoS* ICRC2023, p. 794.

Saturni, Francesco Gabriele et al. (2023). “Dark matter searches in dwarf spheroidal galaxies with the Cherenkov Telescope Array”. In: *PoS* ICRC2023, p. 1366.

Schneider, Peter, Jürgen Ehlers, and Emilio E. Falco (1992). *Gravitational Lenses*.

Sjöstrand, Torbjörn, Stephen Mrenna, and Peter Skands (June 2008). “A brief introduction to PYTHIA 8.1”. In: *Computer Physics Communications* 178.11, pp. 852–867. arXiv: `0710.3820 [hep-ph]`.

Springel, V., J. Wang, M. Vogelsberger, A. Ludlow, A. Jenkins, A. Helmi, J. F. Navarro, C. S. Frenk, and S. D. M. White (Dec. 2008). “The Aquarius Project:

the subhaloes of galactic haloes". In: 391.4, pp. 1685–1711. arXiv: 0809.0898 [astro-ph].

Steigman, Gary, Basudeb Dasgupta, and John F. Beacom (July 2012). "Precise relic WIMP abundance and its impact on searches for dark matter annihilation". In: 86.2, 023506, p. 023506. arXiv: 1204.3622 [hep-ph].

Strigari, Louis E., James S. Bullock, Manoj Kaplinghat, Joshua D. Simon, Marla Geha, Beth Willman, and Matthew G. Walker (Aug. 2008). "A common mass scale for satellite galaxies of the Milky Way". In: 454.7208, pp. 1096–1097. arXiv: 0808.3772 [astro-ph].

Tak, Donggeun, Matthew Baumgart, Nicholas L. Rodd, and Elisa Pueschel (Oct. 2022). "Current and Future γ-Ray Searches for Dark Matter Annihilation Beyond the Unitarity Limit". In: 938.1, L4, p. L4. arXiv: 2208.11740 [astro-ph.HE].

Tisserand, P. et al. (July 2007). "Limits on the Macho content of the Galactic Halo from the EROS-2 Survey of the Magellanic Clouds". In: 469.2, pp. 387–404. arXiv: astro-ph/0607207 [astro-ph].

VERITAS Collaboration: E. Hays (Oct. 2007). "VERITAS Data Acquisition". In: *arXiv e-prints*, arXiv:0710.2288, arXiv:0710.2288. arXiv: 0710.2288 [astro-ph].

Villanueva-Domingo, Pablo, Olga Mena, and Sergio Palomares-Ruiz (May 2021). "A Brief Review on Primordial Black Holes as Dark Matter". In: *Frontiers in Astronomy and Space Sciences* 8, 87, p. 87. arXiv: 2103.12087 [astro-ph.CO].

Vincent, S. and VERITAS Collaboration (July 2015). "A Monte Carlo template-based analysis for very high definition imaging atmospheric Cherenkov telescopes as applied to the VER". In: *34th International Cosmic Ray Conference (ICRC2015)*. Vol. 34. International Cosmic Ray Conference, p. 844. arXiv: 1509.01980 [astro-ph.IM].

Walker, Matthew G., Mario Mateo, Edward W. Olszewski, Jorge Peñarrubia, N. Wyn Evans, and Gerard Gilmore (Oct. 2009). "A Universal Mass Profile for Dwarf Spheroidal Galaxies?" In: 704.2, pp. 1274–1287. arXiv: 0906.0341 [astro-ph.CO].

Weekes, T. C. et al. (July 1989). "Observation of TeV Gamma Rays from the Crab Nebula Using the Atmospheric Cerenkov Imaging Technique". In: 342, p. 379.

Weinstein, A. (Jan. 2008). "The VERITAS Trigger System". In: *International Cosmic Ray Conference*. Vol. 3. International Cosmic Ray Conference, pp. 1539–1542. arXiv: `0709.4438 [astro-ph]`.

Wilks, S. S. (1938). "The Large-Sample Distribution of the Likelihood Ratio for Testing Composite Hypotheses". In: *The Annals of Mathematical Statistics* 9.1, pp. 60 –62.

Winston, Roland (Feb. 1970). "Light Collection within the Framework of Geometrical Optics". In: *Journal of the Optical Society of America (1917-1983)* 6.2, pp. 245–247.

Wolf, Joe, Gregory D. Martinez, James S. Bullock, Manoj Kaplinghat, Marla Geha, Ricardo R. Muñoz, Joshua D. Simon, and Frank F. Avedo (Aug. 2010). "Accurate masses for dispersion-supported galaxies". In: 406.2, pp. 1220–1237. arXiv: `0908.2995 [astro-ph.CO]`.

Yodh, Gaurang B. (1997). "The MILAGRO gamma ray observatory". In: *Nuclear Physics B - Proceedings Supplements* 52.3, pp. 264–268. ISSN: 0920-5632.

Zel'dovich, Ya. B. and I. D. Novikov (Feb. 1967). "The Hypothesis of Cores Retarded during Expansion and the Hot Cosmological Model". In: 10, p. 602.

Zwicky, F. (Oct. 1937). "On the Masses of Nebulae and of Clusters of Nebulae". In: 86, p. 217.

A Appendix A : Point-Source Analysis

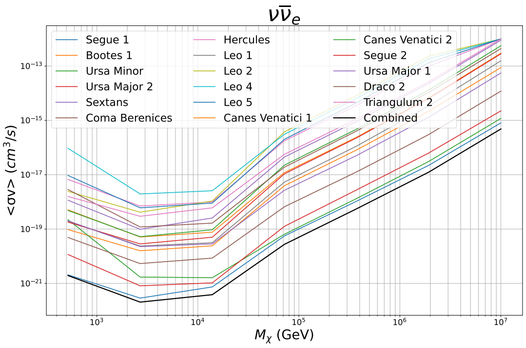

$\nu\bar{\nu}_e$

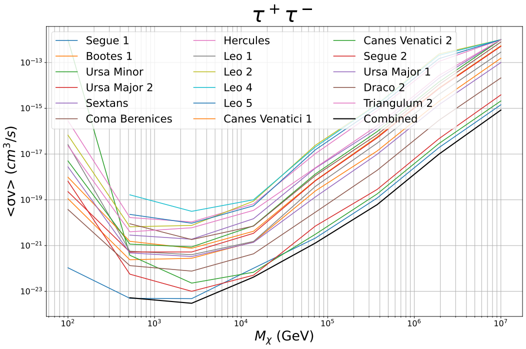

$\tau^+\tau^-$

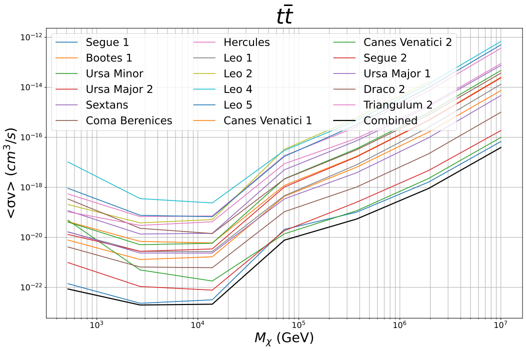

$t\bar{t}$

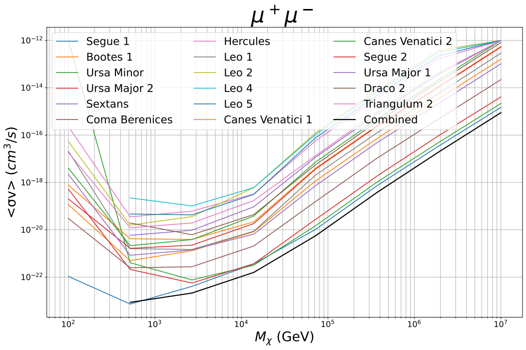
$\mu^+\mu^-$
Segue 1
Bootes 1
Ursa Minor
Ursa Major 2
Sextans
Coma Berenices
Hercules
Leo 1
Leo 2
Leo 4
Leo 5
Canes Venatici 1
Canes Venatici 2
Segue 2
Ursa Major 1
Draco 2
Triangulum 2
Combined
<σv> (cm³/s)
10⁻¹²
10⁻¹⁴
10⁻¹⁶
10⁻¹⁸
10⁻²⁰
10⁻²²
10²
10³
10⁴
10⁵
10⁶
10⁷
Mχ (GeV)

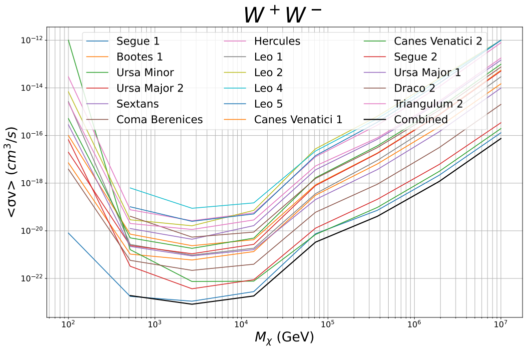
W^+W^-
Segue 1
Bootes 1
Ursa Minor
Ursa Major 2
Sextans
Coma Berenices
Hercules
Leo 1
Leo 2
Leo 4
Leo 5
Canes Venatici 1
Canes Venatici 2
Segue 2
Ursa Major 1
Draco 2
Triangulum 2
Combined
<σv> (cm³/s)
10⁻¹²
10⁻¹⁴
10⁻¹⁶
10⁻¹⁸
10⁻²⁰
10⁻²²
10²
10³
10⁴
10⁵
10⁶
10⁷
Mχ (GeV)

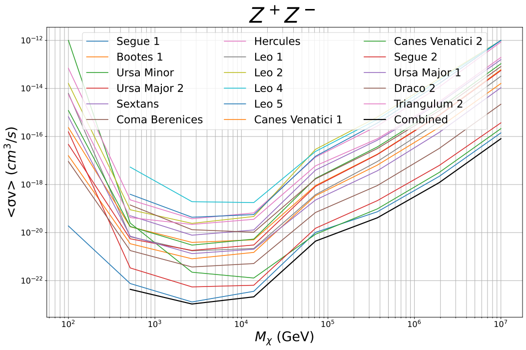
Z^+Z^-
Segue 1
Bootes 1
Ursa Minor
Ursa Major 2
Sextans
Coma Berenices
Hercules
Leo 1
Leo 2
Leo 4
Leo 5
Canes Venatici 1
Canes Venatici 2
Segue 2
Ursa Major 1
Draco 2
Triangulum 2
Combined
<σv> (cm³/s)
10⁻¹²
10⁻¹⁴
10⁻¹⁶
10⁻¹⁸
10⁻²⁰
10⁻²²
10²
10³
10⁴
10⁵
10⁶
10⁷
Mχ (GeV)

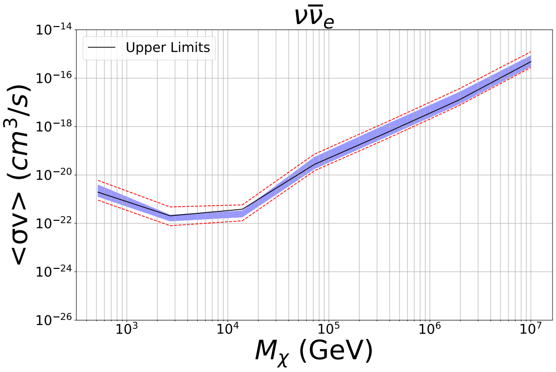
$\nu\bar{\nu}_e$
Upper Limits
<σv> (cm^3/s)
10^{-14}
10^{-16}
10^{-18}
10^{-20}
10^{-22}
10^{-24}
10^{-26}
10^3
10^4
10^5
10^6
10^7
M_χ (GeV)

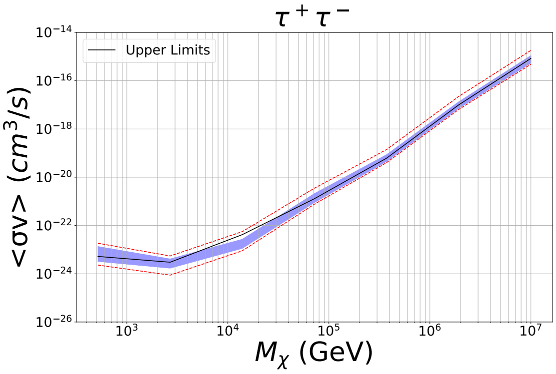
$\tau^+\tau^-$
Upper Limits
<σv> (cm^3/s)
10^{-14}
10^{-16}
10^{-18}
10^{-20}
10^{-22}
10^{-24}
10^{-26}
10^3
10^4
10^5
10^6
10^7
M_χ (GeV)

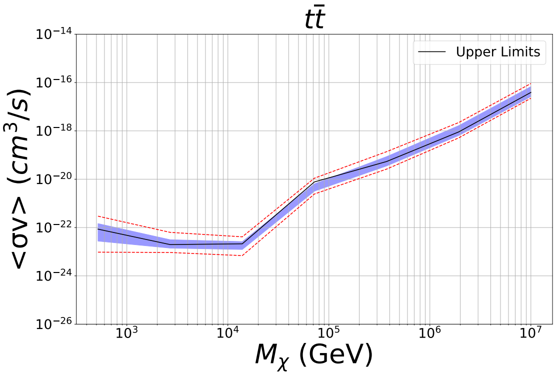
$t\bar{t}$
Upper Limits
<σv> (cm^3/s)
10^{-14}
10^{-16}
10^{-18}
10^{-20}
10^{-22}
10^{-24}
10^{-26}
10^3
10^4
10^5
10^6
10^7
M_χ (GeV)

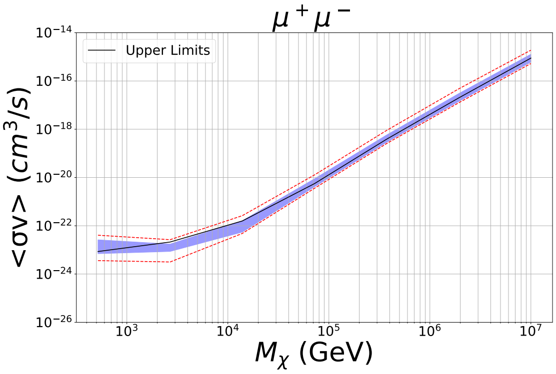
$\mu^+\mu^-$
Upper Limits
<σv> (cm^3/s)
10^{-14}
10^{-16}
10^{-18}
10^{-20}
10^{-22}
10^{-24}
10^{-26}
10^3
10^4
10^5
10^6
10^7
M_χ (GeV)

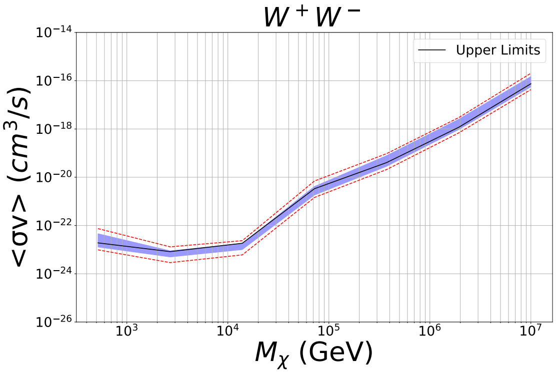
W^+W^-
Upper Limits
<σv> (cm^3/s)
10^{-14}
10^{-16}
10^{-18}
10^{-20}
10^{-22}
10^{-24}
10^{-26}
10^3
10^4
10^5
10^6
10^7
M_χ (GeV)

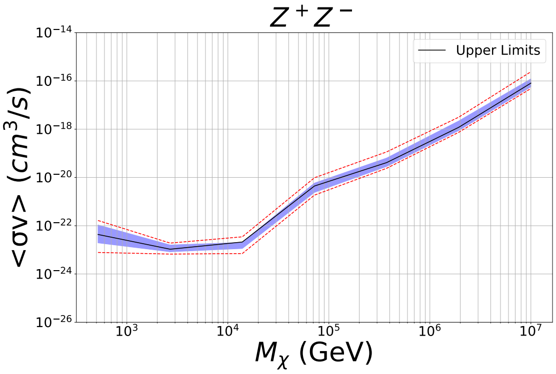
Z^+Z^-
Upper Limits
<σv> (cm^3/s)
10^{-14}
10^{-16}
10^{-18}
10^{-20}
10^{-22}
10^{-24}
10^{-26}
10^3
10^4
10^5
10^6
10^7
M_χ (GeV)

B Appendix B : Extended-Source Analysis

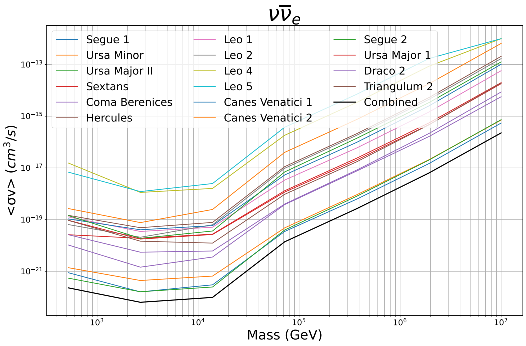

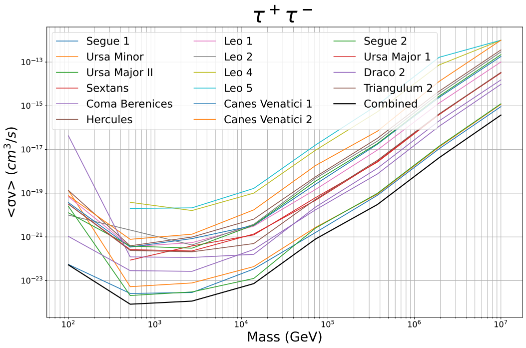

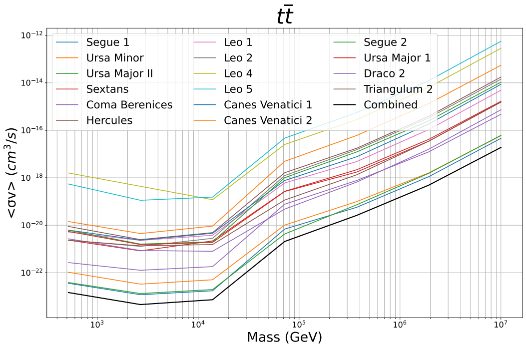

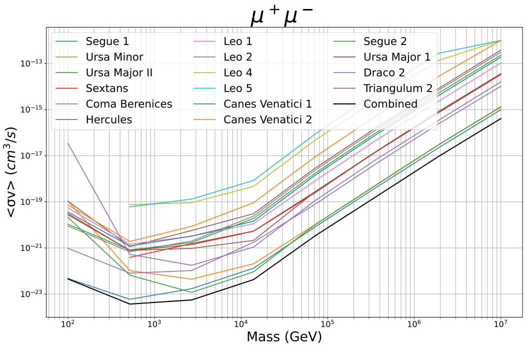
$\mu^+\mu^-$
Segue 1
Ursa Minor
Ursa Major II
Sextans
Coma Berenices
Hercules
Leo 1
Leo 2
Leo 4
Leo 5
Canes Venatici 1
Canes Venatici 2
Segue 2
Ursa Major 1
Draco 2
Triangulum 2
Combined
<σv> (cm^3/s)
10^{-13}
10^{-15}
10^{-17}
10^{-19}
10^{-21}
10^{-23}
10^2
10^3
10^4
10^5
10^6
10^7
Mass (GeV)

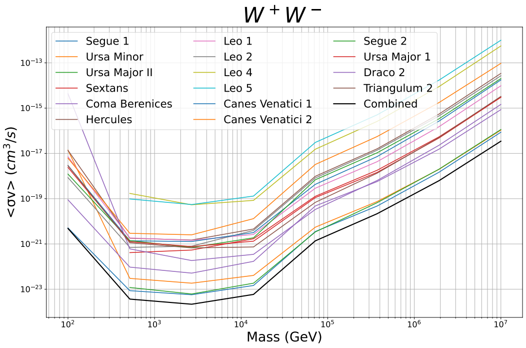
W^+W^-
Segue 1
Ursa Minor
Ursa Major II
Sextans
Coma Berenices
Hercules
Leo 1
Leo 2
Leo 4
Leo 5
Canes Venatici 1
Canes Venatici 2
Segue 2
Ursa Major 1
Draco 2
Triangulum 2
Combined
<σv> (cm^3/s)
10^{-13}
10^{-15}
10^{-17}
10^{-19}
10^{-21}
10^{-23}
10^2
10^3
10^4
10^5
10^6
10^7
Mass (GeV)

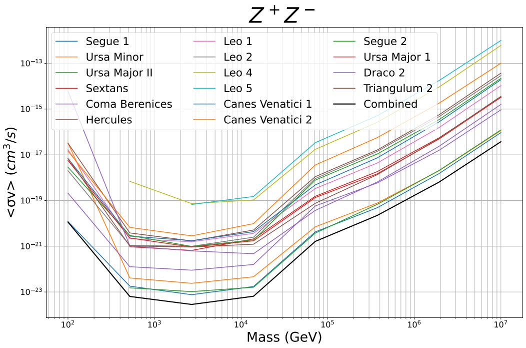
Z^+Z^-
Segue 1
Ursa Minor
Ursa Major II
Sextans
Coma Berenices
Hercules
Leo 1
Leo 2
Leo 4
Leo 5
Canes Venatici 1
Canes Venatici 2
Segue 2
Ursa Major 1
Draco 2
Triangulum 2
Combined
<σv> (cm^3/s)
10^{-13}
10^{-15}
10^{-17}
10^{-19}
10^{-21}
10^{-23}
10^2
10^3
10^4
10^5
10^6
10^7
Mass (GeV)

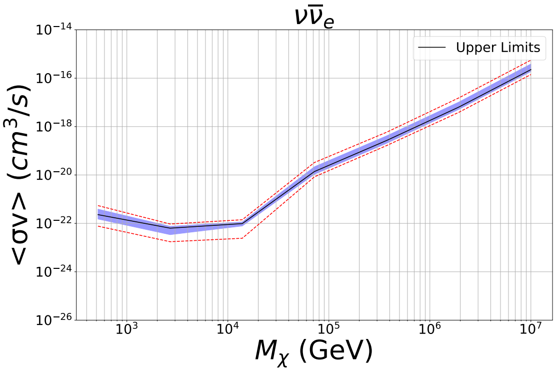
$\nu\bar{\nu}_e$
Upper Limits
$<\sigma v>$ (cm^3/s)
10^{-14}
10^{-16}
10^{-18}
10^{-20}
10^{-22}
10^{-24}
10^{-26}
10^3
10^4
10^5
10^6
10^7
M_χ (GeV)

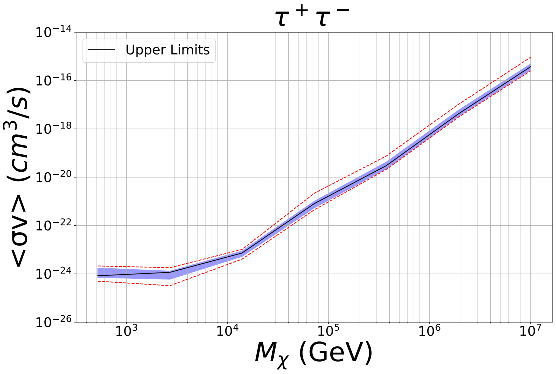
$\tau^+\tau^-$
Upper Limits
$<\sigma v>$ (cm^3/s)
10^{-14}
10^{-16}
10^{-18}
10^{-20}
10^{-22}
10^{-24}
10^{-26}
10^3
10^4
10^5
10^6
10^7
M_χ (GeV)

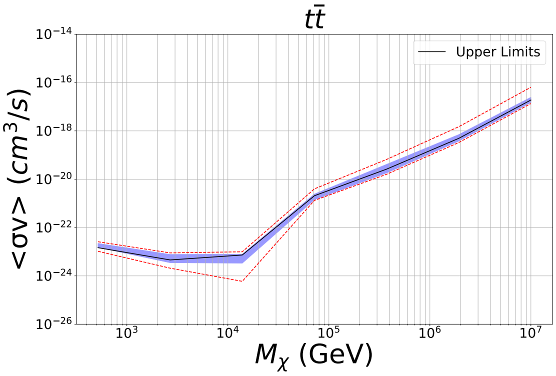
$t\bar{t}$
Upper Limits
$<\sigma v>$ (cm^3/s)
10^{-14}
10^{-16}
10^{-18}
10^{-20}
10^{-22}
10^{-24}
10^{-26}
10^3
10^4
10^5
10^6
10^7
M_χ (GeV)

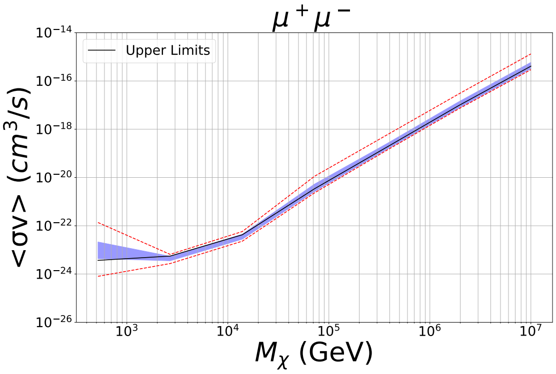
$\mu^+\mu^-$
Upper Limits
<σv> (cm^3/s)
10^{-14}
10^{-16}
10^{-18}
10^{-20}
10^{-22}
10^{-24}
10^{-26}
10^3
10^4
10^5
10^6
10^7
M_χ (GeV)

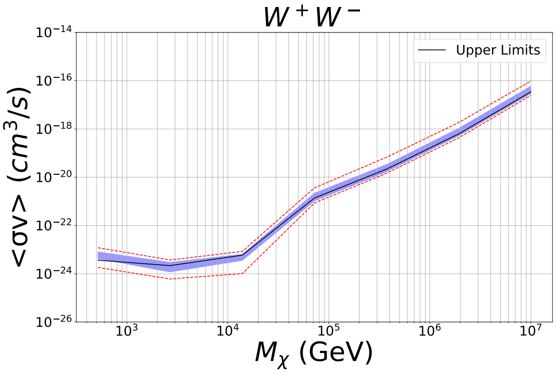
W^+W^-
Upper Limits
<σv> (cm^3/s)
10^{-14}
10^{-16}
10^{-18}
10^{-20}
10^{-22}
10^{-24}
10^{-26}
10^3
10^4
10^5
10^6
10^7
M_χ (GeV)

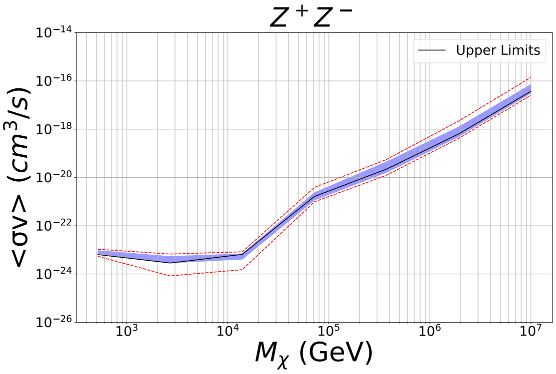
Z^+Z^-
Upper Limits
<σv> (cm^3/s)
10^{-14}
10^{-16}
10^{-18}
10^{-20}
10^{-22}
10^{-24}
10^{-26}
10^3
10^4
10^5
10^6
10^7
M_χ (GeV)